journal of the international meteor organization

WGN

51:4
august 2023

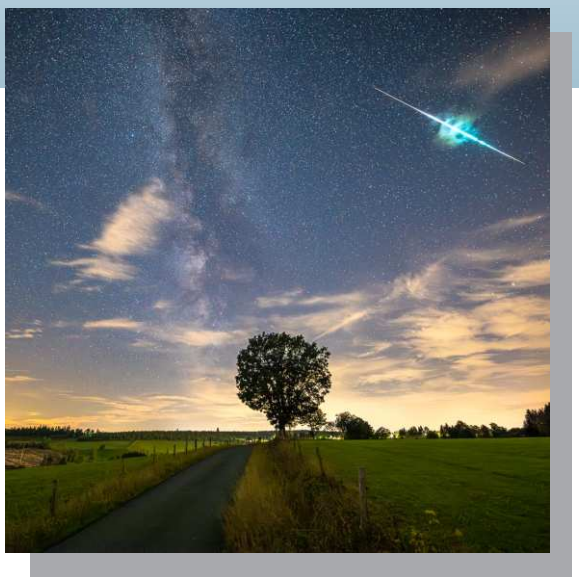

Report on the International Meteor Conference 2023
Utilizing video meteor trails to understand radio meteor detection
Luminous altitude characteristics of Halley type and long period meteor showers

ISSN 1016-3115

WGN Vol. 51, No. 4, August 2023, pp. 69 – 108

Conferences

International Meteor Conference 2023 Report *Greet Lembregts and Marthe D'Hooghe* 69

Ongoing meteor work

Utilizing Video Meteor Trails to Understand Radio Meteor Detection *M. T. German* 72

Halley Type and Long Period Meteor Shower Luminous Altitude Characteristics *Yasuo Shiba* 93

Front cover photo

Bright fireball with multiple flares on 2023 August 11 at $22^{\mathrm{h}}12^{\mathrm{m}}50^{\mathrm{s}}$ UT. Canon EOS R5 was used with 12-mm lens at $f/2$ and 15 s exposures at ISO 4000. Image credit: David Feldmann.

Writing for WGN

This Journal welcomes papers submitted for publication. All papers are reviewed for scientific content, and edited for English and style. Instructions for authors can be found in WGN **45:1**, 1–5, and at `http://www.imo.net/docs/writingforwgn.pdf` .

Copyright

Legal address

International Meteor Organization, Jozef Mattheessensstraat 60, 2540 Hove, Belgium.

Conferences

International Meteor Conference 2023 Report

Greet Lembregts and Marthe D'Hooghe

Received 2023 September 16

As amateur meteor observers, we thought we already knew a lot about meteors. We had spent hours in a cold field admiring shooting stars. Many visual observing reports had been sent to the IMO. We had attended the Dutch Meteor Day. And then the IMC was organised in Belgium. At the Euro Space Center. We didn't need to talk about it. Of course we would go!

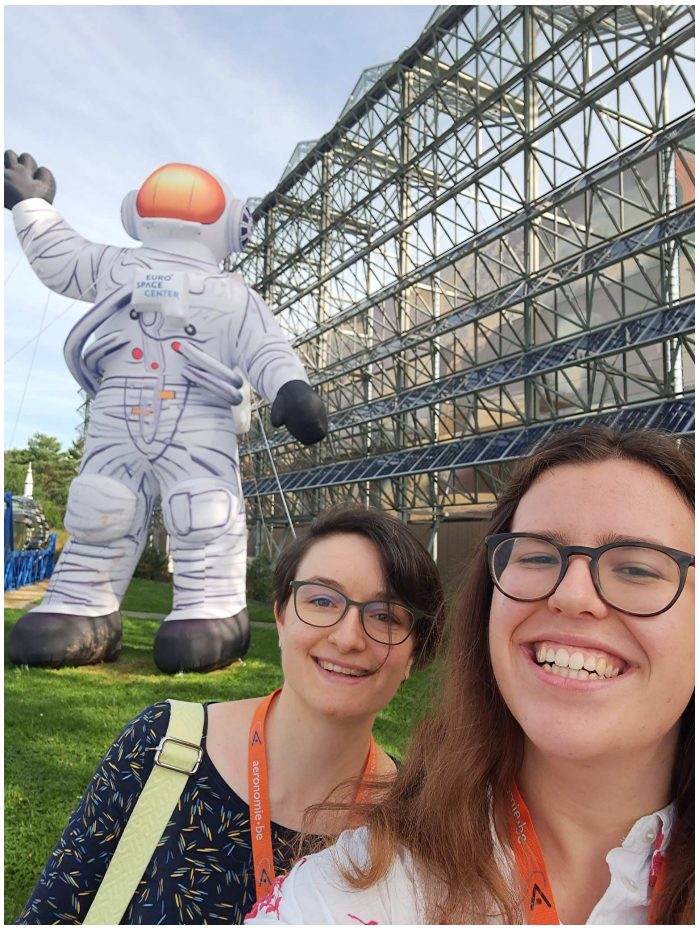

Figure 1 – Greet and Marthe in front of the Euro Space Center.

But little did we know about how much there was actually to know about this magnificent subject. We didn't know research on meteors and meteorites was so in-depth. In the stylish auditorium, we gained as much knowledge as we could. And although some presentations were way over our heads, we learned a lot. Both about meteors themselves and about the meteor community. That meteors could be observed with seismographic equipment was something we would not have guessed. And, as a refreshing break, even the scientists themselves are sometimes in doubt. Was that light flash a lunar impact, a satellite, or maybe a visual malfunction? Fortunately, there is the IMC, filled with like-minded people ready to discuss the matter. And discussions continued during coffee breaks, supplemented with a piece of cake. The Euro Space Center proved to be an excellent host.

And what a host it was, could a more astronomical location be found for the IMC? Even the rooms were Mars-themed! As was a part of the VIP tour, which for us started at the Mars habitat. The recreated habitat taught you about travelling to and living on the red planet, and let you search for scarce resources with Mars rovers. Springs hanging from the ceiling simulated walking in the reduced gravitational field on the surface on Mars. And though we did not fall in the centrifuge, gravity had us landing on the soft mat

Figure 2 – The Mars rover challenge during the VIP activities.

Figure 3 – The opening of the IMC in the auditorium.

Figure 4 – Listening to Antonio at the Radioastronomy Station in Humain.

Figure 5 – A beautiful sight in the caves of Han.

of the free fall slide. For those with a robust stomach, there was a chair that rotated freely around three axes. Fortunately, dinner was not served until after the VIP event.

Then, there was the excursion. Two buses drove us through the rolling countryside. First stop: an outpost of the Royal Observatory. Old radio dishes were standing in line, now silent witnesses of old scientific observations. Like an honorary hedge, they watched as we were introduced to the observing site. Some old mounts were refurbished to support new dishes, busy with observing the sun. As icing on the cake, the sun shone happily that day. What a contrast with the previous rainy day!

In a vast green lawn, the wooden cabin houses the BRAMS equipment and supports a camera for meteor observing. We got an instant desire to observe meteors! Unfortunately, we couldn't stay overnight because we had another excursion planned: the Han caves. After the hot summer day, the caves were a refreshing change. An authentically dressed guide led us through a doorway into the cave complex. How big it was in there! Behind each corner you could see different rock formations, from the familiar stalactites and stalagmites to veritable curtain formations of dripping limestone, artistically lit by many small lamps. An even more artistical light show decorated one of the biggest chambers, telling about the origin of Earth, life and the caves themselves.

Gradually, the river that led us to the exit of the cave also led us to the end of the IMC. The last evening was coming up, one that became even nicer than the previous evenings. The ESC staff had prepared a barbecue for us. And was this a crazy tradition or inspiration from Belgian beer, an IMC song was composed.

For a while, we felt like we were back at summer camp with the youth movement. Marc told us that the IMC once originated from camp reunions. And honestly, that is indeed the atmosphere an IMC breathes. Participants greeting and hugging each other warmly, this is so much more than just a conference. And whether you like it or not, by the end of the conference, you are adopted. Part of the great meteor family. And you are counting down to the next family reunion: the 2024 IMC. See you next year!

IMO bibcode WGN-514-lembregts-IMC2023 NASA-ADS bibcode 2023JIMO...51...69L

Figure 6 – Group photo of the on-site participants of the IMC 2023 at the entrance to Euro Space Center park. Credit: Peter Slansky.

Ongoing meteor work

Utilizing Video Meteor Trails to Understand Radio Meteor Detection

M. T. German[1]

"A meteor hits planet Earth" — that's a story idea but that doesn't give me any indication of what the character is. — Steven Soderbergh

The amateur radio meteor observer does not know where the meteoroid just recorded was or anything with any certainty about its characteristics. A new technique has been developed enabling single station radio meteor observers to establish properties of meteoroids from the definitive association of radio with video camera data. The technique uses video trail coordinates to establish that there exists, within the trail, the unique conditions necessary for specular reflection in forward scatter to occur. All the meteor characteristics found from video camera capture can be applied to the matched radio meteoroid signature for interpretation. The methodology was assessed during 2022 and results and analysis are presented.

Received 2023 June 5

1 Introduction

Meteor trails are routinely captured and analysed by video camera networks yielding orbital information by back-calculation, mass and magnitude estimates from trail intensities, and meteorite recovery from forward projections.

However, for amateur radio meteor observations it is normally only possible to infer meteor streams and to record shower activity (Verbeeck & Rault, 2022); details such as meteor location, height and mass are unobtainable. This paper presents the endeavours of an amateur radio meteor observer to understand the where, what and how of detected radio signals.

The project took a holistic approach: research on and measurement of transmitter characteristics; development of receiving systems and methods; and understanding the theoretical aspects of meteor forward scatter. The study of the transmitter, meteor and receiver (*T-M-R*) geometry revealed the unique conditions at the end of the head echo that made it possible for radio meteor signatures and video camera trails to be definitively matched. The known locations of transmitter and receiver stations and the reported locations of meteors from video meteor trails could be used to test that the conditions for specular scatter were met. Specifically, the termination of the Doppler frequency shift associated with the head echo would occur when the meteoroid was at the point of closest approach to transmitter and receiver. Calculation of the changing slant ranges of a meteoroid from the transmitter and from the receiver would determine whether a minimum was passed through along the trail; if so the conditions for match were met.

Other approaches to measure meteor trajectories from forward scatter have been proposed. For example Steyaert et al. (2010) derived meteor velocity and directional vectors that were solved from Doppler shift and Doppler shift derivatives at, at least three observation points. Head echoes detected at seven stations during the Geminids stream were analysed. They concluded that timing accuracy improvements were needed and that an automated process was required to replace the time-intensive post-processing of head echoes from audio files. Lamy et al. (2021) reported development of a method to reconstruct meteoroid trajectories from the timing of zero Doppler shift points at different locations. The technique used initial times, speed and height from video trajectories to select matching meteor echoes. Ernotte (2018) explained the derivation of velocity from the slope of the head echo Doppler shift and the half-width of the first Fresnel zone. Verbelen (2019) used Ernotte's relationship to determine velocities from head echoes during showers assuming ionisation heights.

It is noted that Fleet in an IMC 2015 paper described the results of matching detections on his co-located video cameras and radio system in the UK (Fleet, 2015). The detection time of 'energetic', long-duration specular reflection radio events were associated with video event times falling within an acceptance window. Radio meteor event locations were obtained from individual cameras, mainly over France to the north of GRAVES.

The methodology presented here does not require any assumptions to be made concerning the meteoroid trajectory. The measured trail properties from video camera captures can be applied to any matched radio head echo: in particular, the distribution of meteoroid locations around the receiving station were found. The Radio-Video (R-V) matching approach used the GRAVES transmitter in France and the author's receiving systems at Hayfield. Meteor trails were obtained from the UK Meteor Network (UKMON) database. The results of the study, conducted over the 2022 calendar year, are presented.

[1]Entropy, Swallow House Lane, Hayfield, SK22 2HB, United Kingdom. Email: mike.german@physics.org

IMO bibcode WGN-514-german-radiovideo
NASA-ADS bibcode 2023JIMO...51...72G

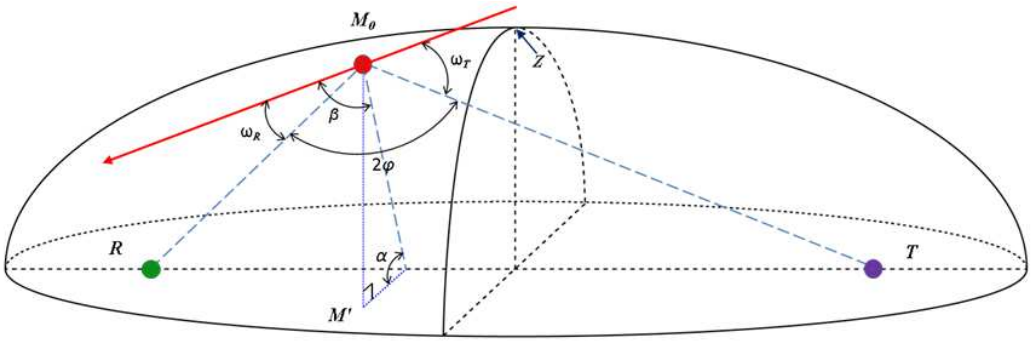

Figure 1 – The forward scatter geometry. At M_0 the meteoroid is at closest approach to transmitter T and receiver R. TMR is contained in the radio propagation plane, inclined at angle α (shown to aid visualisation). Point M' is vertically below M_0. The forward scatter angle is 2φ and β is the angle between the trajectory and plane of propagation. The angles between the trajectory and the directions from M_0 towards T and M_0 towards R are given by ω_T and ω_R respectively.

2 Geometry of a Radio Meteor

2.1 Some radio meteor geometry background

A meteoroid entering the atmosphere is heated by friction with atmospheric gases and an ionisation cloud forms. The plasma cloud is initially spherical. As the meteor progresses, the cloud expands and a tail forms behind the main spherically shaped front (see Dyrud et al., 2008; Marshall et al., 2015). McKinley (1961) notes that most of the visible radiation arises from vaporising material local to the meteoroid and that it is known as the head of the meteor. If radio waves scatter from the ionised cloud, the signal may be detected by a radio receiver. Dyrud et al. (2008) and Janches et al. (2014) refer to the head echo plasma as a cloud of electrons moving at the speed of the meteor. Verbeeck (2023) suggests that the term 'head echo' is solely reserved for the radio scatter from the plasma cloud around the moving meteoroid as modelled by Dyrud et al. (2008). The term is more loosely used as the early phase of the radio meteor signature prior to the tangent point: this looser terminology is adopted in the present paper. The head echo is characterised by a rapidly changing Doppler shift from transmitted frequency.

The arrangement for forward scatter is shown at Figure 1 with the trajectory of a meteoroid (shown as an arrow) passing a transmitter T and receiver R. If the scattered radio waves from the meteoroid are sufficiently strong a signal may be detected. The trajectory of the meteoroid may reach a point M_0 where the path is tangential to an ellipsoid of revolution with foci at T and R. This region around M_0 is significant for a number of connected reasons[a]:

- the meteoroid is tangential to the ellipsoid
- the total radio path TMR is at a minimum
- the radio meteor signature changes from head echo to so called '*specular reflection.*'

Specular reflection occurs around the tangent point where and when the ionised trail is of sufficient length and duration for scatter from points along the trail to reach the receiver simultaneously. The path length, TMR, changes along the trajectory; in-phase and anti-phase conditions lead to peaks and troughs in the received signal level.[b] The resultant amplitude variations can be explained by Fresnel diffraction, a physical process commonly encountered in wave optics. The peaks in signal level occur at what are known as Fresnel zones. The continuing received radio signal now results from scatter from the ionisation along the line of the trajectory rather than the moving meteoroid. Hence there is no Doppler shift for this part of a radio meteor signature.

Thus, the simple and most common radio meteor signature comprises at least the specular reflected part of the trail. Prior to the tangent point a head echo may be detected where the signal is above noise level. After the tangent point, the enhanced specular reflection signal usually swamps the relatively small head echo signal. However, negative Doppler shifted scatter from the moving body continues until the ionisation diffuses and in some instances have been recorded. An example of this is shown in Wilschut (2020).

Whereas all meteoroid ionisation clouds have the potential to scatter incident radiation from a transmitter and thereby generate a head echo, some do not meet the tangency conditions and specular reflection does not occur. For example in Figure 1 at M_0, the meteoroid may have ceased to create ionisation before reaching the tangency point. Verbeeck and Rault (2022) show these conditions at Figure 6.4. The resulting radio signature, where scatter is sufficiently strong, is a *naked* head echo and the type was mentioned by Kaufmann (2020a).

German (2020) used a Monte-Carlo, head echo model and found a region of space, central between T and R, where the tangent condition would not be met[c]. Kaufmann (2020b) confirmed the model prediction and demonstrated a dependency on the trail bearing and depression angle; the shallower the depression angle, the fewer the events meeting the condition.

In addition to simple radio signatures, it is worth mentioning the long duration meteor events reported, for example by Bourdillon et al. (2005), where the

[a]These factors are also noted in a Verbelen (2019) paper.

[b]See for example Wislez (1995) Figure 6, or Verbeeck and Rault (2022) Figure 6.12.

[c]Referred to in German (2020) as a "no-go zone".

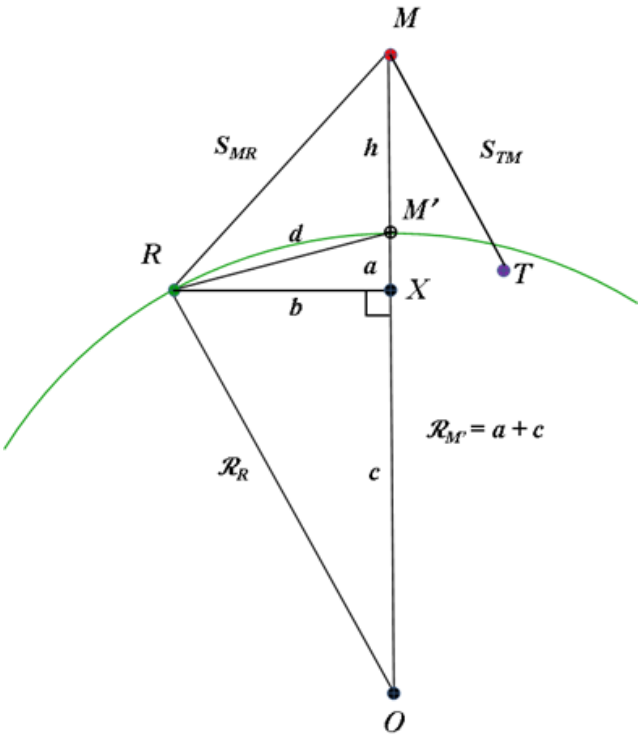

Figure 2 – TMR geometry showing slant range S_{MR} of Meteor M from Receiver R. Where $\mathcal{R}_R$ and $\mathcal{R}_{M'}$ are Earth radii to R and M' for WGS84 ellipsoid, and d is the chord between R and M'. The view is in the plane of RMO. Note T is not in this plane.

Doppler spectrum became bifurcated. It was speculated that the meteor trails were distorted by wind. A head echo may precede these events.

2.2 Calculational steps to establish a definitive Radio-Video (R-V) event match

There are a number of stages needed to establish the existence of a match of a particular video camera meteor trail with a particular radio meteor event. The detailed calculational steps are given here and a more general flow diagram of the practical steps involved in the matching process is in the Methodology Section. The UK Meteor Network (UKMON) combines and analyses matched multi-camera meteor trails into an archive database listing. A preliminary filtering based on time separation selects candidate radio events and video trails for the more detailed match assessment.

The video database listing has latitude, longitude and height coordinates at the raw camera times along the trail. To enable easier analysis these coordinate points were interpolated here to give 200 equi-spaced time-steps. UKMON trail coordinates use the EGM96 (Earth Gravitational Model) standard which includes the WGS84[d] (World Geodetic System). WGS84 takes into account the oblate spheroid shape of Earth and EGM96 the variations in surface height above and below WGS84 datum. Calculations involving altitude and latitude should take into account the EGM96 height datum[e] and the WGS84 ellipsoid model. Algorithms were developed to calculate the chord length between WGS84 latitude/longitude pairs and for the Earth radius at given WGS84 latitude and for convenience are at Annex A.

The next stage is to calculate the slant ranges between transmitter to meteor and meteor to receiver using the video trail, transmitter and receiver coordinates. The slant range S_{MR} from the meteor M to the receiving station R is shown in Figure 2. M' is on the surface of the Earth vertically below M, and O is the centre of the Earth. The view is in the plane of RMO. $\mathcal{R}_R$ and $\mathcal{R}_{M'}$ are Earth radii from O to R and M' and d is the chord between R and M' (See Annex A).
In triangle RXO

$$\mathcal{R}_R^2 = b^2 + c^2 \tag{1}$$

In triangle RXM', where d is the chord between R and M'

$$d^2 = a^2 + b^2 \tag{2}$$

for OXM'

$$\mathcal{R}_{M'} = a + c \tag{3}$$

Substituting c from (3) and b from (2) in equation (1) and rearranging in a

$$a = \frac{\mathcal{R}_{M'}^2 + d^2 - \mathcal{R}_R^2}{2\mathcal{R}_{M'}} \tag{4}$$

In triangle RXM, $S_{MR} = \sqrt{b^2 + (h+a)^2}$ where S_{MR} is the slant range from M to R and height, h, of meteor above the Earth's surface. Substituting from (2) gives

$$S_{MR} = \sqrt{d^2 - a^2 + (h+a)^2} \tag{5}$$

In Equation (5) h is given. The chord d and the component parts of a in equation (4) are calculated from the coordinates. The slant range S_{TM} from Transmitter T to Meteor M is similarly calculated. The total slant range is given by

$$S_{tot} = S_{TM} + S_{MR} \tag{6}$$

2.3 The Slant Range Minimum

In the example, Figure 3, slant ranges were calculated using the 200 interpolated video trail coordinate points and the coordinates of the GRAVES transmitter and Hayfield receiving station. The total slant range (S_{tot}) is plotted against time. The position (time) of the minimum in S_{tot} occurs at around $20^{\mathrm{h}}54^{\mathrm{m}}16\overset{\mathrm{s}}{.}07$ UTC.

The total slant range is at a minimum when the meteoroid trajectory is tangential to the ellipsoid (Figure 1). Thus, having confirmed a minimum exists in the total slant range curve, it is reasonable to assume the match is not random. Therefore radio and video events may be considered a definitive match.

[d] https://en.wikipedia.org/wiki/World_Geodetic_System#WGS84

[e] In practice variations in the EGM96 datum over the UK are small and have been ignored here. See also Annex A.

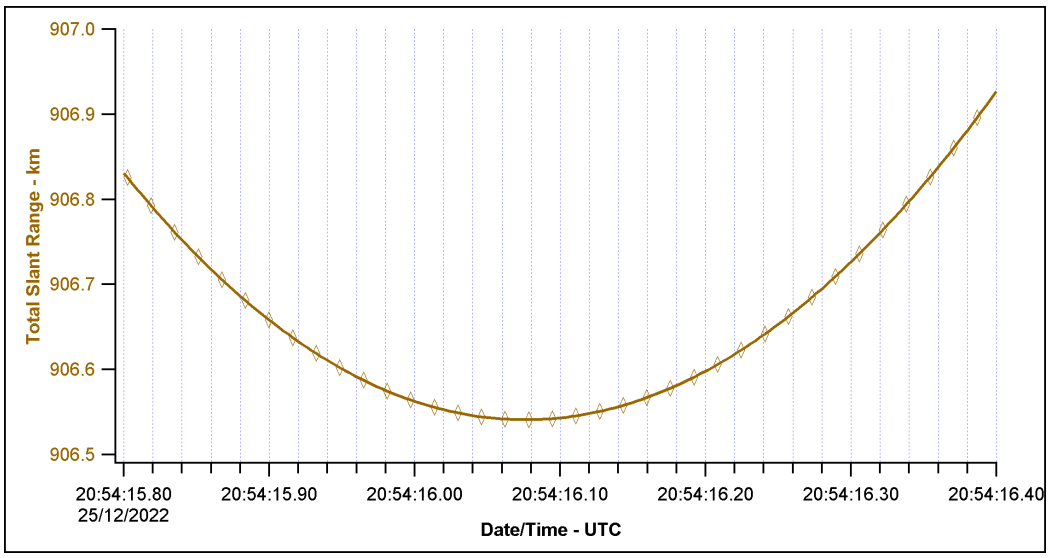

Figure 3 – Example the total slant range (S_{tot}) plotted against time. NB. Every 5th point is plotted.

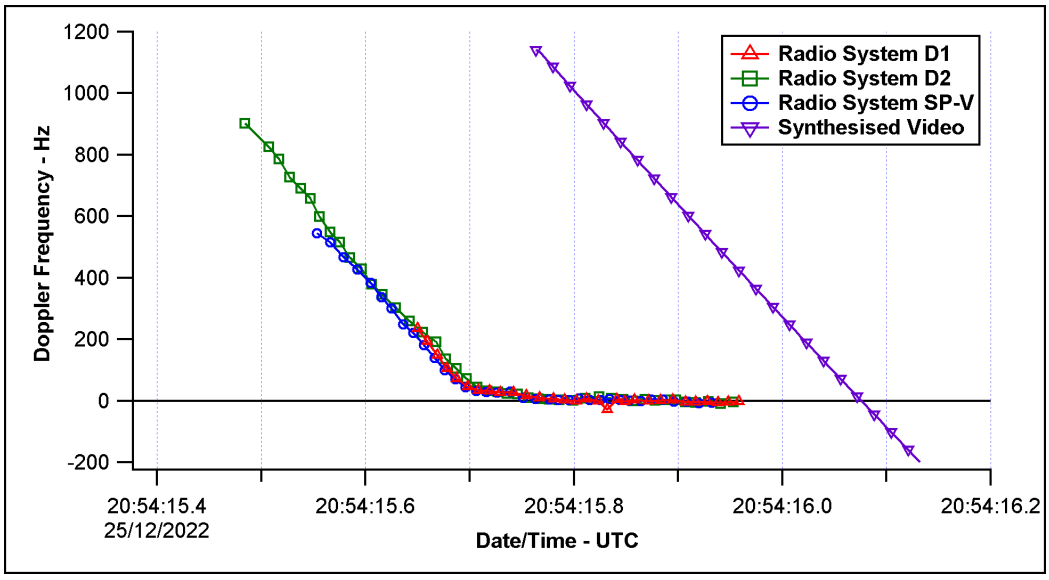

Figure 4 – Example of Doppler shifts $\Delta Dopp$ from measured radio head echoes and synthesised from the video trail data.

Using the bi-static radar equation, German (2020), a video trail *synthesised*[f] Doppler shift frequency, $\Delta Dopp$ can be found directly by differentiation of the total slant range curve shown in Figure 3.

$$\Delta Dopp = \frac{1}{\lambda}\frac{d}{dt}(S_{tot})$$

where λ is the transmitter wavelength, $\frac{d}{dt}(S_{tot})$ is the rate of change of total slant range S_{tot} with respect to time.

Part of the synthesised Doppler shift is shown in Figure 4 and compared with measured Doppler shift frequencies from three receiving systems at Hayfield. The synthesised video Doppler shift is zero at the same time as the minimum in the total slant range.

The parameters of a straight line fit to the head echo Doppler shift prior to the specular reflection provide a slope and intercept time. The difference between this intercept time and the synthesised video Doppler zero time is used to align times between radio and video. Thus, for example, the first detection time of a head echo can be linked to meteor height at that time from video data. The rate of change of Doppler shift or the slope of the frequency curve, $\Delta Dopp/\Delta t$, will be used in the next Section to determine the meteoroid velocity.

2.4 First Fresnel zone and velocity

The pattern and positions of the peaks in signal amplitude around the tangency point – the Fresnel zones – mentioned in Section 2.1 are governed by wavelength of the radiation and the position of the tangency point relative to the transmitter and receiver. The innermost zone is referred to as the first Fresnel zone. The half width of this zone and the rate of change of the Doppler shift are used to determine velocity of the meteoroid. The geometry of the half-width of the first Fresnel zone **f** is (depicted as the thick line) shown in Figure 5. It is general practice for the tangent point to be referenced to

[f] *synthesised* because, of course, physically there is no Doppler associated with a video trail

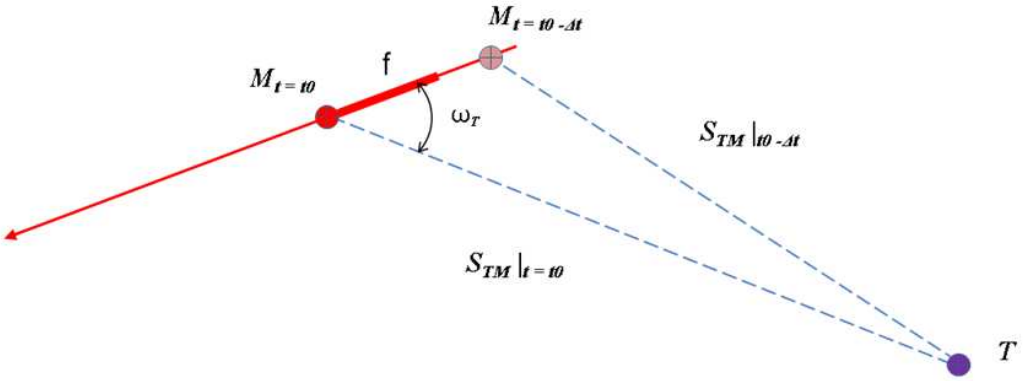

Figure 5 – The Fresnel zone at tangent point. The half-width of the first zone **f** is shown as a thick line.

a time t_0 along the trajectory. The situation is shown in the Figure where the meteoroid is at the tangency point $M_{t=t_0}$. Two positions for the meteoroid are shown at time t_0 and an earlier time $t_0 - \Delta t$. Corresponding slant ranges from the transmitter are shown as $S_{TM}|_{t=t_0}$ and $S_{TM}|_{t=t_0-\Delta t}$, where the vertical bar indicates the time at which the slant ranges measured. The angle between the trajectory and the line between from $M_{t=t_0}$ to T is shown as ω_T and is required in the calculation of **f**.

The first Fresnel zone half-width is determined in a number of stages. To start with, the full equation for **f** based on McKinley's (1961) original equation is given.

$$\mathbf{f} = \sqrt{\left[\frac{\lambda S_{TM} S_{MR}}{(S_{TM} + S_{MR})(1 - \sin^2\varphi\cos^2\beta)}\right]\Bigg|_{t=t_0}} \qquad (7)$$

The first Fresnel zone centre is evaluated at time $t = t_0$ as denoted on the vertical bar in (7). The transmitter wavelength is λ. S_{TM} and S_{MR} are the slant ranges computed from the trail at $t = t_0$, φ is half the forward scatter angle and β is the angle between the trajectory and plane of propagation as shown in Figure 1.

φ is found from

$$2\varphi = \cos^{-1}\left[\frac{S_{TM}^2 + S_{MR}^2 - D_{TR}^2}{2S_{TM}S_{MR}}\right]\Bigg|_{t=t_0} \qquad (8)$$

where D_{TR} is the cord between R and T and is determine from the known transmitter and receiver station coordinates referenced to the WGS84 ellipsoid. The algorithm for calculation of the cord is given at Annex A2 for convenience.

To obtain β it is necessary first to calculate ω_T. This is done by considering in Figure 5 the distance travelled by the meteoroid between the two points that include the first Fresnel half-width. In Figure 6 this distance travelled is shown as ΔM.

Point $M_{t=t_0}$ corresponds to the meteoroid at tangency and $M_{t=t_0-\Delta t}$, to the position at a time interval Δt earlier[g]. During the time Δt, the meteoroid height has fallen by ΔH and the ground range has changed

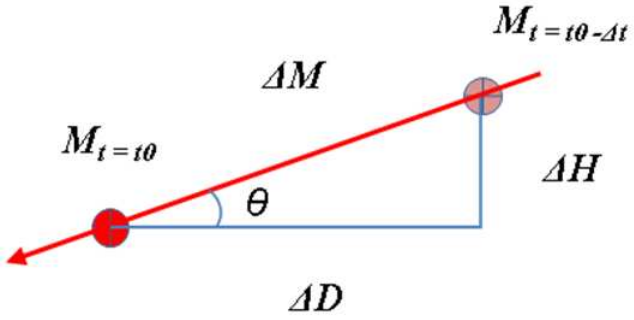

Figure 6 – Calculation of distance meteoroid moved by ΔM in time Δt where ΔD is change in ground range and ΔH change in height. The depression angle of the trajectory is θ.

by ΔD. In practice the increments ΔH and ΔD are evaluated from the interpolated video trail latitude and longitude. ΔM is readily determined from the triangle.

$$\Delta M = \sqrt{\Delta D^2 + \Delta H^2} \qquad (9)$$

Incidentally, and not necessary for the determination of **f**, the trajectory depression angle θ is straightforwardly found from the triangle.

Using the computed slant ranges shown in Figure 5 and ΔM from (9), ω_T can be found from,

$$\cos\omega_T = \frac{(S_{TM}|_{t=t_0})^2 + S_{TM}|_{t=t_0-\Delta t})^2 + \Delta M^2}{2S_{TM}|_{t=t_0} \cdot S_{TM}|_{t=t_0-\Delta t}}$$

The angle β between the trajectory and plane of propagation is obtained by rearranging the identity given by McKinley (1961, pp238)

$$\cos\beta = \frac{\cos\omega_T}{\sin\varphi} \qquad (10)$$

The half-width of the first Fresnel zone **f** given in (7) can now be evaluated with the computed slant ranges, φ from (8), ΔM from (9) and β from (10).

Finally the meteoroid velocity V_{Fres} may be calculated from the first Fresnel zone half-width, **f**, from (7)

[g]McIntyre (2023) gave the average duration of all meteors in 2022 as about 0.5 s. Trail coordinates interpolated to 200 points gives a maximum Δt of around 2.5 ms. Thus at highest geocentric velocity, ΔM corresponds to about 0.15 km. Verbeeck (1995) calculated the variation of first Fresnel Zone half-widths for several distances between transmitter and values of β. On a rough estimate, his values for the GRAVES to Hayfield distance (860 km) are between 0.6 and 6 km. It is therefore considered that 200 point interpolation of trails provides adequate increments in time and distance for these calculations.

Figure 7 – The GRAVES transmitter site at Broye-lès-Pesmes (47.3480° N 5.5151° E) showing the four Large Planar Array (LPA) antennas. Photo credits: Stephane Muratet / ONERA.

and the rate of change of Doppler shift (slope of the frequency curve), $\Delta Dopp/\Delta t$, using the formulation of Ernotte (2018).

$$V_{Fres} = \mathbf{f} \cdot \sqrt{(-\Delta Dopp/\Delta t)} \tag{11}$$

The equation applies to the radio meteor head echo frequency slope and to the synthesised Doppler shift frequency.

It is also noted in the triangle Figure 6 video trail velocity V_M may also be found at each increment along the trajectory from

$$V_M = \frac{\Delta M}{\Delta t} \tag{12}$$

3 Transmitter

3.1 Location and Characteristics

The high powered GRAVES transmitter enables head echoes of small meteoroid to be detectable with modest antennas at large ranges. However, the transmission sequence is complex and the resulting radiated power, changes abruptly with direction. The rear-ward radiation pattern is irregular and probably, in any one direction (azimuth and elevation), the composite of radiation from multiple LPA panels (see Figure 7). The beam steering 'spike' provides useful timing and can indicate the relative signal strength contributions from different parts of the scan sequence. Located at Broye-lès-Pesmes near Dijon in France it is part of a space surveillance radar owned by the French MoD and operated on their behalf by ONERA. The radar, known as GRAVES – *Grand Réseau Adapté à la Veille Spatiale* transmits continuously on 143.050 MHz.

Few technical details have been published on this military radar. An early paper by Michal et al. (2005) provides an overview of the intended design. It describes the general volumes of space illuminated by the beam forming LPAs (Large Planar Arrays). In the absence of published data reference is made to the measurements of amateur enthusiasts sourced from the internet[h] and from the present author's own investigations. Jouadé et al. (2019) report that circular polarisation is used for the receiving antennas to counter Farday rotation effects. They reveal that the transmitter

[h]Internet documents are, of their nature, transitory. If the documents cannot be found, the author offers pdf copies of the pages with due recognition to the original authors.

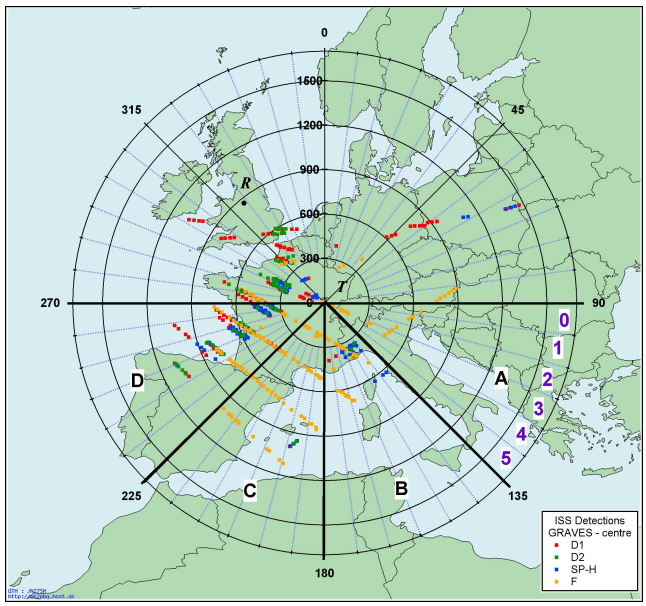

Figure 8 – The GRAVES transmitter, T, is centre and receiver station at R. The four sectors **A** to **D** correspond to the LPAs. The sub-sectors 0 to 5 on each panel (shown for **A** only) radiate in sequence on are synchronised on all 4 sectors. ISS orbit detections are discussed in Section 3.2.

antennas are "linearly polarised" but do not mentioned the orientation.

The four LPA antennas provide coverage of volumes of space with azimuthal directions form 90° through to 270°, in four distinct sectors each covering 45°. We arbitrarily indicate these sectors **A**, **B**, **C** and **D** in the Figure 8. The GRAVES transmitter T site and the receiving station R and the location receiving station for the present meteor forward scatter studies are also shown in the Figure. The receiving station R is 854 km from T at an azimuthal angle of 324.475°.

Hardenberg (2021) described that the GRAVES LPA sectors were divided into 6 sub-sectors, 7.5 degrees wide which were referred to by the numbers 0 to 5. At a very precise time, a beam was formed in the direction of the first sub-sector (0) of each sector. These 4 sub-sectors radiated the volume of space for 800 ms. The beam forming array then directed the radiation to the next sub-sectors for 800 ms and so on until sub-sector (5) and the sequence repeats from (0). The cycle or sequence of 6 beam-changes took 4.8 seconds. He shows

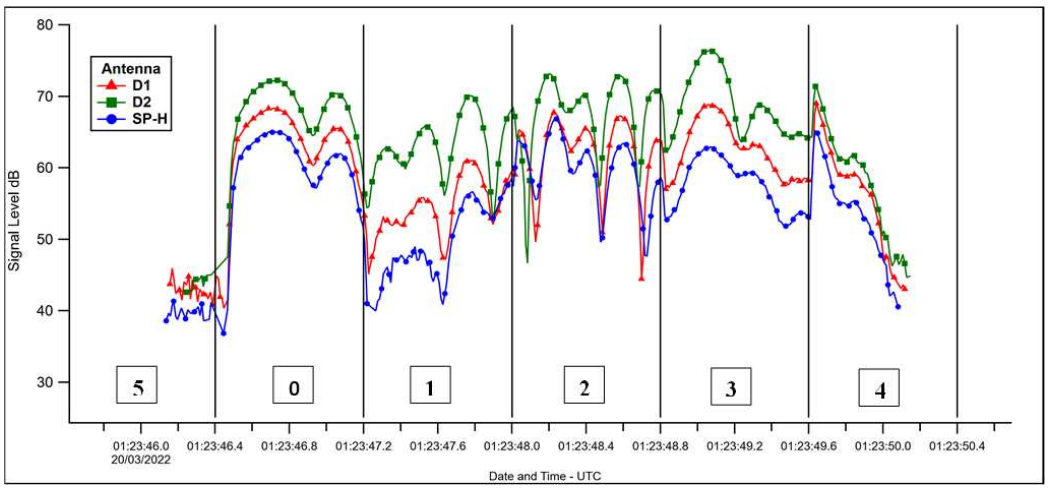

Figure 9 – Signal levels at Hayfield from antennas D1, D2 and SP-H showing the GRAVES LPA beam scan change times (vertical lines) and sub-sector scan sequence numbers (square boxes). The head echo signal level is in sub-sector scan sequence 5. Note abrupt changes in levels coincident with scan time changes. Every 4th point the logged radio data is shown.

beam elevation angles from 15° to 40°. Vallejo (2015) reports he found the beam was synchronised with UTC: starting on the hour for the first sub-sectors and then subsequent subsectors were timed at precisely 800 ms intervals. He also noted from his measurements a phase change in the transmitted signal associated with this beam changing. When viewed in a spectrogram, these changes can generate sharp vertical "spikes" – artefacts of the spectrogram and can serve as useful timing markers.

Norton (2016), based on received scatter from the Moon, estimated the transmitted power from one LPA to be 60 kW. Using what he considered to be "a best guess based on what little information was publicly available" also estimated the front to back ratio of a similar LPA, and estimated the power coming from the rear of one transmitter LPA as 27 kW. He suggested the rearward output of two south facing transmitters would be about 50 kW beamed north.

It can be assumed the transmitter antennas are designed to radiate in tight beams within the desired subsectors and the pattern would be expected to be uniform in all directions within sectors **A**, **B**, **C** and **D**. However, the radiation pattern to the rear of GRAVES would be far from uniform, with reflections from the ground, control buildings and so forth; radiation from the various sectors could combine in unpredictable directions and elevations. The UK is at azimuth angles from GRAVES between 290° and 350°. An example of the resulting complexity is shown in Figure 9. From R-V matching, the meteoroid was at a 308° azimuth angle from GRAVES over the Isle of Wight, close to Southampton in the UK and was a sporadic with velocity of about 42 km/s and estimated mass of 0.2 g. The head echo signal is in sub-sector 5 and the remaining part of the signature is the specular reflection. The main beam direction moves between subsectors at 800 ms intervals, shown as the vertical bars in the Figure.

3.2 ISS interrogation of transmitter radiation pattern

Official details of GRAVES have not been published but several exercises have investigated the volume of space behind the LPAs. Navara et al. (2014) used the passage of the ISS (International Space Station) through the GRAVES beams to measure the Doppler shift and matched the ISS position with an astronomical telescope. Their results are summarised in Figure 4 of the reference and show a patchy picture for radiation from GRAVES. A similar exercise was conducted by the Collaborative Database Group (2020) where three radio meteor monitoring stations in England and one in the Republic of Ireland measured the ISS Doppler signal times and matched them with TLEs (Two Line Element sets that provide ISS positional data at given times). The range, elevation and direction of the ISS from GRAVE were determined from latitude, longitude of the ISS footprint. With simple scaling of the ISS altitude, the positions corresponding to meteor heights (120 km) were found. The ISS makes about 16 orbits of the Earth each day and there is an approximate repeat of orbit tracks over the same area on the ground every 3 days. The highest latitude reached is 51.9° N.

Following a similar approach, the author deployed four antenna-receiver systems at Hayfield England to simultaneously monitor the space station during the period October and November 2020. The detections were dependent on the ISS orbits during the period and on the orientation of large structures, such as the solar arrays, that give the largest reflected power. The distribution of ISS detections for the GRAVES was given at Figure 8. The interest was in azimuth and elevation angles of ISS detection from GRAVES. Generally, as might be expected, there were more ISS detections in the main beam than in the rear lobes. Although detections appear to be along long lines they were not necessarily recorded in the same orbit. The influence of the transmitter radiation pattern on meteoroid detectability is discussed in Section 7.3.

Table 1 – Summary of receiver system antennas

System	Antenna	Polarisation	Head Amp	Period Used	Azimuth – deg.
D1	3 element loop-fed Yagi	N/A	Y	All Year	93/273 †
D2	3 element loop-fed Yagi	N/A	Y	All Year	3/183 †
SP-H	2 element loop-fed quad	H	Y	Until end July	138
SP-V	Vertical ground plane	V	N	August onwards	Omnidirectional

† Note D1 and D2 antennas mounted orthogonally on same boom pointing vertically and azimuths are in line with the elements. Thus the broadside to the elements is 90 degrees to the elements.

4 Receiver Station

4.1 Location

The radio meteor monitoring station is located at Hayfield – 53.383° N, 1.9526° W at a height of 200 m (WGS84 datum) in the Peak District of England. It is surrounded by hills that raise the observable horizon (see Figure 21). The position of Hayfield relative to the GRAVES transmitter was shown in Figure 8.

4.2 Antennas

An experimental arrangement of antennas was used to provide all round coverage for meteor detection. Although the GRAVES transmission is almost certainly vertically polarized and various receiving antenna polarizations have been used, no particular attention has been paid to polarization in this study.

Pointing vertically, the two LFA (Loop Fed Array) 3 element Yagi antennas were arranged with the bisector of the elements pointing at an azimuth angle of 138° from North towards the GRAVES transmitter. A signal on the bisecting angle would receive equal power. Individually these Yagis have directionality in azimuth similar to a dipole; using the two antennas provided all-round coverage including in elevation. The photograph on the left side of Figure 10 shows these antennas and LFA-Q (Loop Fed Array) two element Quad with a 3 dB total azimuth beam-width of 69° which was directed toward GRAVES with an elevation angle of 20°. The LFA-Q was used from January to July 2022 and was designated SP-H. Narrow band mast head amplifiers with nominal gain of approximately 20 dB were used on these three antennas to compensate for long down leads and to slightly improve noise figures. Antennas and head amplifier were designed for GRAVES frequency of 143.05 MHz. As the study progressed it became clearer that meteoroids were detected at all azimuths. Therefore, for the final five months of the study the LFA-Q was replaced by a ground plane vertical (designated SP-V) for all-round coverage and is shown on the right side of Figure 10. The antennas are summarised in Table 1.

Figure 10 – Receiving antennas at Hayfield. Left-hand panel D1, D2 and SP-H. Right-hand SP-V. See Table 1 for details.

4.3 Receiving System

The bread-board layout of the external hardware is given at Figure 11. Low-loss antenna cables connected to mast head amplifiers via bias-tee DC power in the monitoring room. The three SDR receiver channel were colour coded in line with the antennas: red channel D1 of RSP Duo and green for D2 channel. The RSP2 Pro was blue coded for SP-H and SP-V channels. One GPS DO (Global Positioning System Disciplined Oscillator) provided a reference frequency to the SDR external hardware to regulate tuners and another was used for calibration. The schematic at Figure 12 shows the arrangement of receiver hardware, calibration unit and interface with SDR and logging software.

4.4 PC Software

The PC internal clock was synchronised with Meinberg NTP Time Server Monitor (Diehl, 2008) on a 10 s refresh cycle keeping it generally within a couple of milliseconds of UTC. The three separate SDR channels were controlled by instances of SDRUno (SDRPlay, 2014) feeding instances of Spectrum Lab (Büscher, 2023) and Meteor Logger (Kaufmann, 2017) via Virtual Audio Cables (VACs) as shown in Figure 12. The SDRs frequency was set to 143.049 MHz with an IF bandwidth from −500 Hz to 4000 Hz. IF and RF gain were set to optimise SNR and minimise possible overload. The PC used 32 bit audio level was set to a common level in the SDRs' settings. Lower/upper frequency limits in Meteor Logger were set the same as the IF limits. Spectrum Lab was used to provide a visual display and for general monitoring and not for measurement purposes.

4.5 Calibration

Particular attention was paid to the stability and accuracy of the receiver and data logging. Monthly calibrations were routinely undertaken to ensure frequency

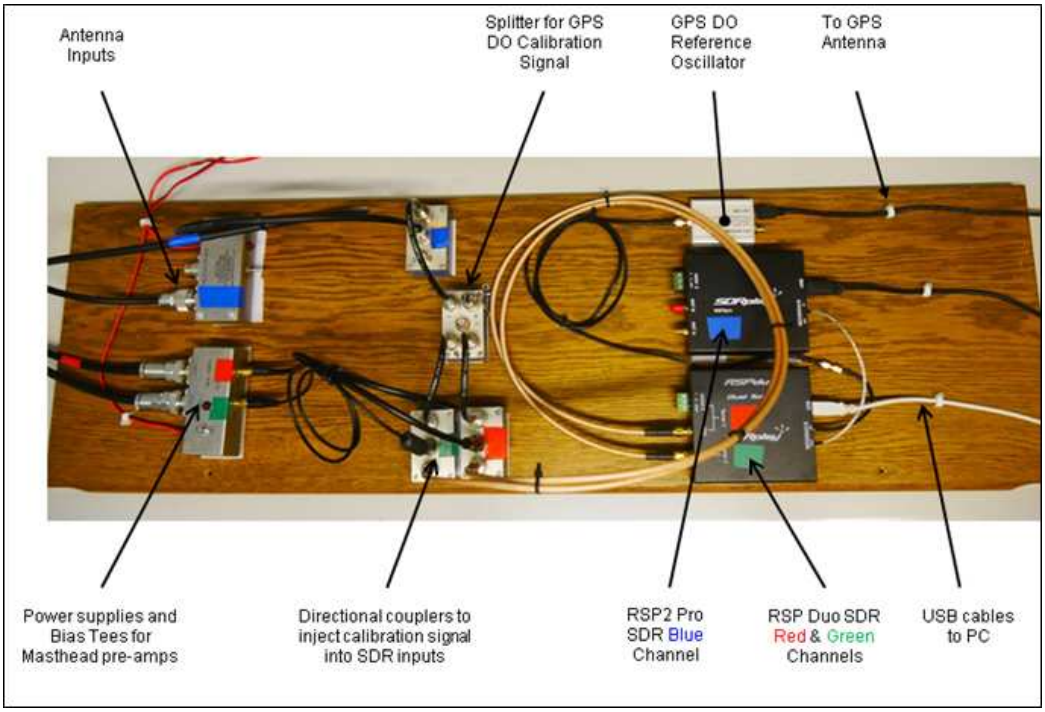

Figure 11 – Breadboard Layout of receiver hardware. Separate GPS DOs (Global Positioning System Disciplined Oscillator) were used for calibration and as a reference frequency for the SDRs.

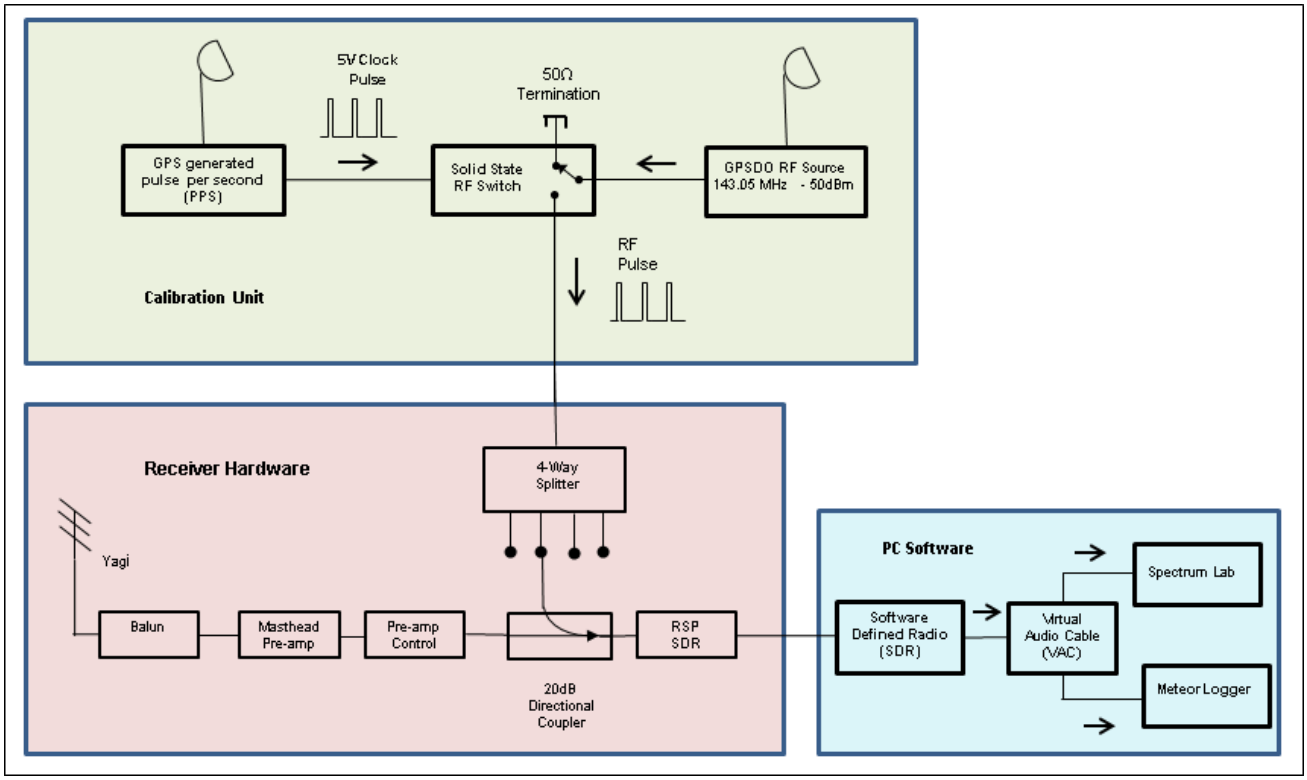

Figure 12 – Schematic of Receiving systems. There are three main sections: receiver hardware, PC software and Calibration Unit.

and gain remained steady and to measure latency between applying signal to RSP input ports and data being recorded by Meteor Logger. The 143.050 MHz output from a GPSDO RF reference source was switched with a solid-state RF switch driven by the UTC synchronised one second pulses from the PPS (Pulse Per Second) output from a GPS. The pulsed RF signal was directed into the RSP input through a signal splitter and directional coupler for 10 minutes (∼ 600 pulses), the signal being recorded by Meteor Logger.

Over the twelve month period, the median latency was measured as approximately 340 ms with a standard deviation of ±10 ms caused, it was assumed, by PC system jitter. Timing was checked against the GRAVES

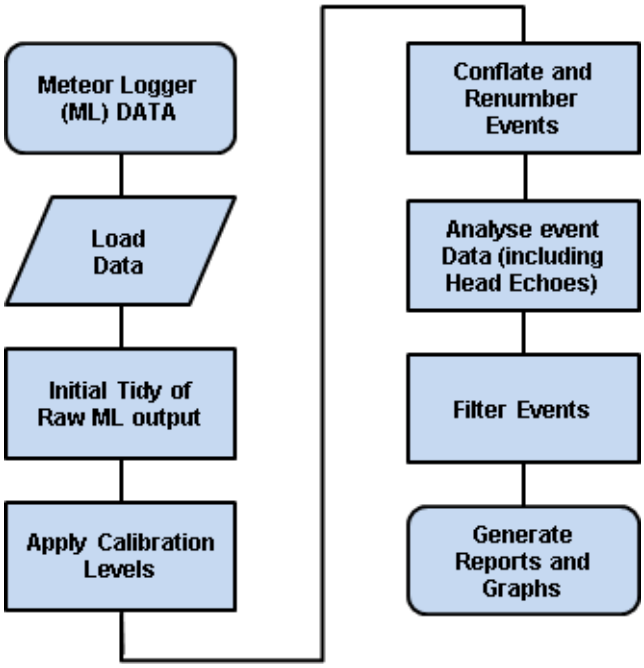

Figure 13 – Process Flow Diagram for Meteor Logger Data.

"marker spike" (Section 3.1). The mean frequency from 3600 calibration pulse for all SDRs was at worst 0.6 ± 0.3 Hz. Measured power levels showed that relative recorded levels were maintained to within ± 1 dB.

4.6 Data Logging and Post-processing Software

In previous works, head echo characteristics have been measured from spectrograms either individually (Steyaert et al., 2010; Ernotte, 2018; Verbelen, 2019; Verbeeck & Rault, 2022) or automatically as proposed by Powell (2019). The Meteor Logger software developed by Kaufmann (2017) produces a meteor event log containing date and time, signal and noise levels, and frequency. The output log data can be post-processed to give individual radio meteor signatures and head echoes analysed directly. In his paper, Kaufmann describes the operation of Meteor Logger. Briefly, the audio input stream is processed continuously in chunks by Fast Fourier Transform (FFT) with high temporal (10.7 ms) and frequency resolution (23.7 Hz). The FFT output identifies those frequencies with the highest power; where 3 adjacent frequency bins are the highest in the time sample and deviate from the previous sample within given limits, the signal is accepted as real and data are logged. See Kaufmann (2017) for full details. The latest version has an estimated accuracy of the calculated frequency from some 10 Hz to 0.01 Hz, depending on the SNR.

Meteor Logger (ML) writes Event Number, Date, Time, Frequency, Signal and Noise to monthly `csv` files which were subsequently processed. Kaufmann developed his own software for post-processing; however, the present author uses purpose written code within the IGOR Pro (1994) environment[i]. A flow chart of the processes is at Figure 13. The process is automated and is usually initiated on whole-month blocks of data. An initial tidy of the raw log data removes ML headings and other artefacts. Calibration levels are applied to time, frequency and signal levels. Events may be discontinuous (from GRAVES beam sequence) or merged when logged closely together in time; attempts are made to conflate or separate such events. Each event is analysed and 32 parameters determined which are used for filtering and characterisation of meteor signatures including head echoes.

A meteor event signature is stored in Igor Pro as date-time, frequency and signal and noise level (relative dB and linear) data points as contiguous data sets. Figure 14 shows an example head echo captured on three antennas. The R-V match reported it over Reading in England: it was a sporadic which was first record on the radio systems at a height of 109 km with a speed of 45 km/s and had an estimated mass of just under 0.1 g.

Filtering by radio signature characteristics, although stringent, effectively reduces interference from satellite reflections and fixed frequencies. On average over the year 13% of logged events were classified as acceptable meteors although this varied widely on a month by month basis depending on levels of interference. The number of meteor events with head echoes tended to follow the monthly diurnal pattern of all meteor events. A simple algorithm developed by Kaufman (2018) was used to identify analysable head echoes. Depending on the month of measurement, between 1% and 14% of all acceptable meteor events were found to have useable head echoes.

5 UK Meteor Network (UKMON) Video Camera Network

The UK Meteor Network (2013) provides video camera coverage of the UK with over two hundred cameras as shown in Figure 15. Contributing stations operate the individual cameras and the output made freely available to UKMON. Analysed data are used for orbit determination and for potential meteorite searches. Extensive listings of captured video event are generated and the data made publicly available for on-line viewing and direct download from the databases. UKMON is a contributor to the Global Meteor Network.

Of particular interest for R-V matching is the routine resolution of meteor trajectories from multiple-camera sightings[j]. The summary data seen in Figure 16 provides shower identification, geocentric velocity (V_g), and estimates of absolute magnitude and mass. A caveat notes *"mass is a lower estimate based on the measured emitted energy and will significantly underestimate the mass of bright events"*.

[i]The Igor Pro `pxp` experiment code is available "as-is" on request

[j]`https://archive.ukmeteornetwork.co.uk/reports/2022/orbits/index.html` and is licensed under a Creative Commons BY 4.0 International License `https://creativecommons.org/licenses/by/4.0/`.

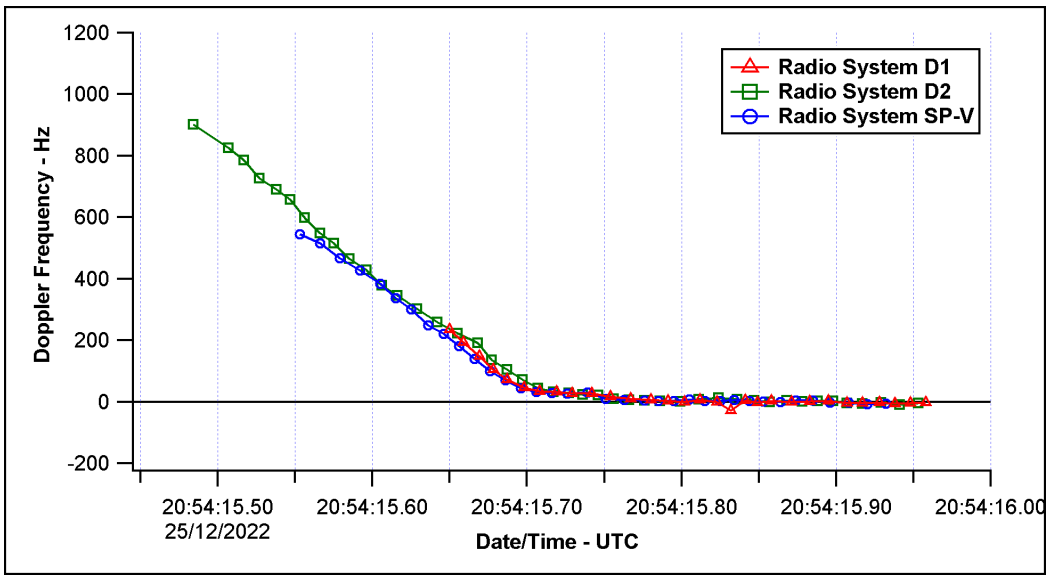

Figure 14 – Meteor event frequency signature received simultaneously on three receivers.

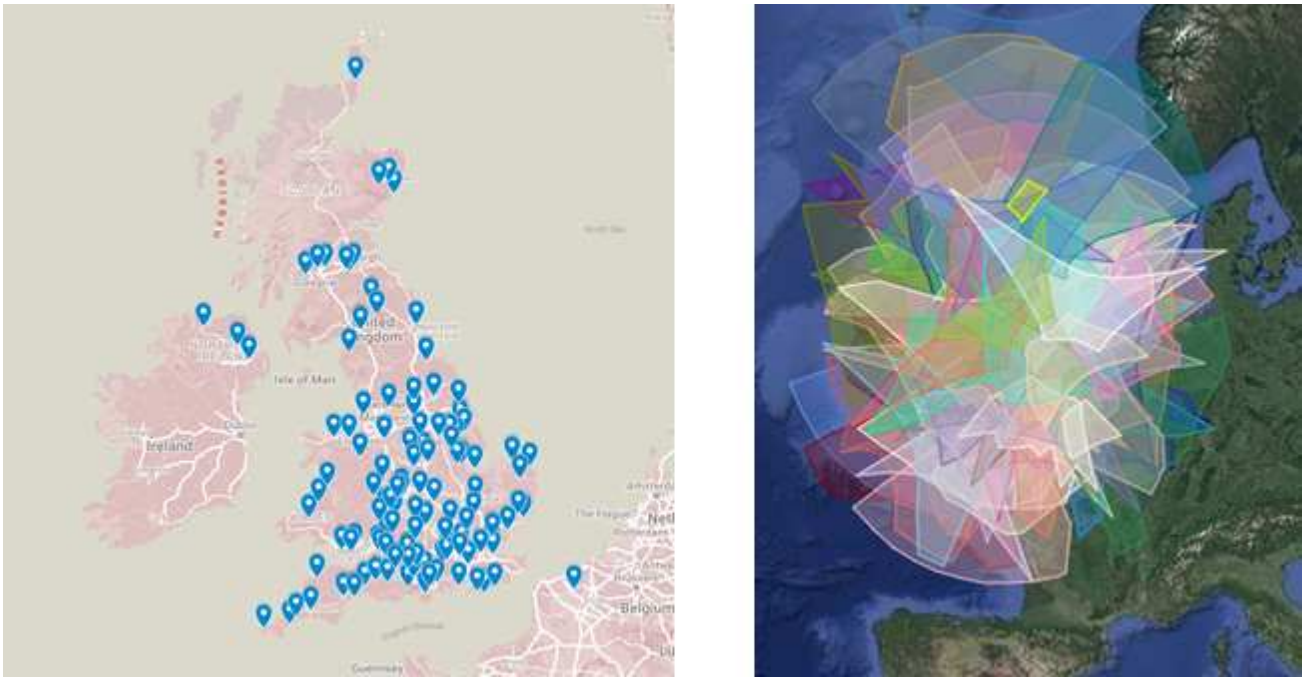

Figure 15 – UK Meteor Network of Video Camera Stations (left) and Coverage to 100 km Height (right) (Courtesy: UK Meteor Network).

```
Summary for Event
-----------------
shower ID 10 QUA (Quadrantids)
Lg 186.57° Bg 66.66° Vg 38.87km/s
mass 0.02861g, abs. mag -0.1
best visual mag 0.7
Path Details
------------
start -2.97° 50.80° 95.31km
end   -3.03° 50.79° 85.44km
```

Figure 16 – UKMON event summary (Courtesy: UK Meteor Network).

The more detailed listings of a meteor trail include the times, latitudes, longitudes and heights required for R-V matching. UKMON archive database provides a useful structure for data download: an annual "Matched Event Orbit and Trajectory Report" links to individual months and days. Internet URL queries can be used to download the header data of all video events by day, month, and year as required. Downloads of the more detailed trail listing can also be generated from URL queries.

6 Methodology

Code developed in the Igor Pro (1994) programming environment is used to control radio meteor and UKMON data downloads, determine initial time match-

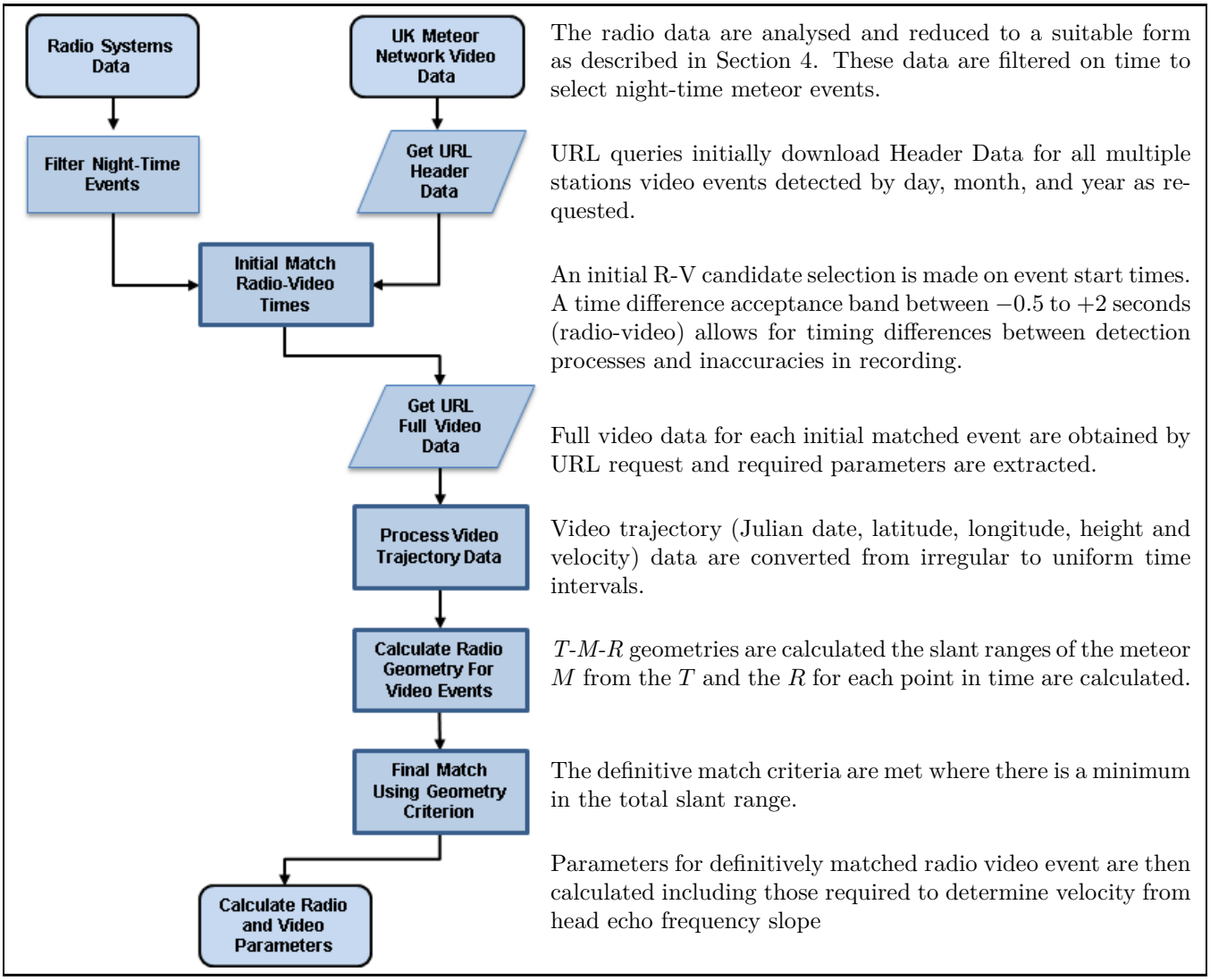

Figure 17 – Flow Diagram for Radio Video Match Methodology.

ing, and calculation of *T-M-R* geometries for definitive R-V matching. Built-in and purpose-written functions are used to calculate derived parameters and provide analysis of matched events. In the present study the process was conducted on a monthly basis with "push button" operation from the software.

The flow diagram, Figure 17 shows the merging and subsequence processing of the radio meteor data and video camera data through to final R-V match and calculation of derived parameters. Reference should be made to previous sections for details.

7 Results

7.1 Radio and Video Raw Data

Radio data were collected throughout 2022 with 22 nights lost from receiver system issues. There were no night-time transmitter outages. Cloud cover periods affecting video data collection were not analysed. The receiver systems and antennas were detailed in Section 4 and summarised in Table 1.

Over all systems, about 1.5% of the 2 855 174 accepted logged meteor events in 2022 had head echoes that were useable. A summary of the numbers of radio meteor head echo events during hours of darkness and of multi-station video events are given at Table 2. The numbers of events preliminarily selected based on time and definitely matched are shown. For the video events 1.9% of all events in the year were selected using time constraints, and of these 60% were definitely matched to radio head echoes. Differences in antenna gain and radiation pattern, and variable levels of interference meant that the video events were not always matched by all systems. The yield of R-V matched events to all video events is about 1%.

7.2 Assessment of R-V match

The velocity V_M, derived from trail positions and height using a straight line fit to the video trail data, equation (12), and velocity V_{Fres} computed from radio TMR and video synthesised Doppler (11) are compared against the given video event geocentric velocity V_g in Figure 18. A visual inspection show, in general, there is a reasonable match using the trail data, indicating the interpolation provides acceptable numbers for slant range calculations. There is more spread in the synthe-

Table 2 – Summary of radio head echo and video multi-station events.

Event source	All Events	Preliminary Selection	Definitive Match
Video Camera	72937	1396	834
D1	12746	862	549
D2	17116	993	604
SP-H	5897	220	122
SP-V	5491	556	212

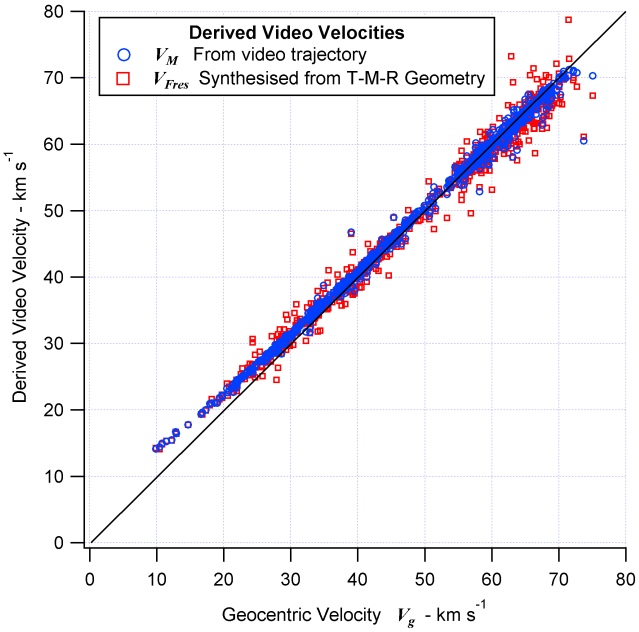

Figure 18 – Calculated video trail V_M and synthesised Doppler velocity V_{Fres} compared with geocentric velocity V_g.

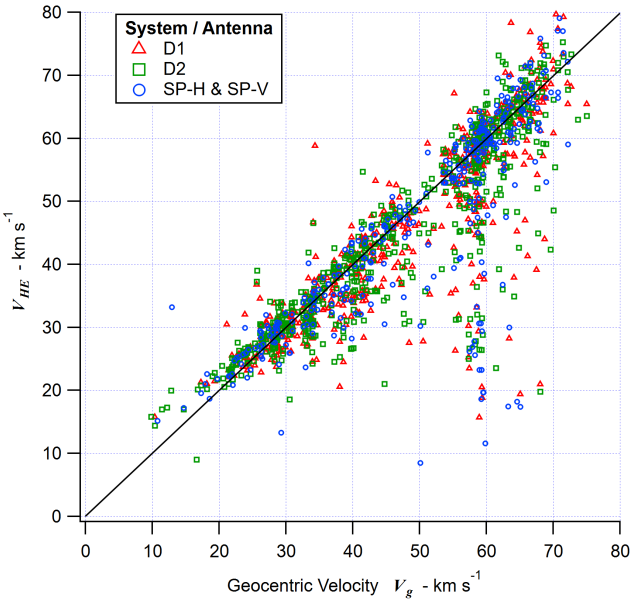

Figure 19 – Meteoroid velocity V_{HE} from the head echo frequency slope and Fresnel zone width compared with V_g.

sised Doppler velocity. The reason for this has not yet been fully investigated. It is noted that both sets show a departure from the 1:1 straight line guide at lower values of V_g; the reason for this is not understood.

The velocities V_{HE} calculated using the half-width of the first Fresnel zone from the video trail, equation (11), and the head echo Doppler frequency slope are shown in Figure 19. The agreement with V_g is poorer. At about 60 km/s the calculated velocities are particularly poorly estimated. These events correspond to the Perseid shower. An inconclusive investigation found that some of these events were of the bifurcation type reported by Bourdillon et al. (2005); it is thought that the multiple frequencies present in the radio meteor signature may have become confused in Meteor Logger leading to distortions in the recorded head echo. It has also been noticed that a number of logged head echo slopes are not straight lines and hence the simple linear fit may not be suitable under all circumstances. The signal to noise ratio (SNR) for the early part of the head echo signature is routinely calculated and ranged from 8 to 30 dB with the majority around 15 dB. No obvious correspondence could be found between the magnitude of SNR and the departures in agreement seen in Figure 19. It is worth acknowledging that head echoes with such low values of SNR can be resolved and detected by Meteor Logger.

7.3 Distribution of Radio Video (R-V) Matches

The ground range and azimuth of R-V matched meteors centred on the receiving station in Hayfield are shown in Figure 20. The points are at the end of the head echo detection i.e. at zero Doppler shift. Algorithms for range and azimuth calculations are given in Annex A for convenience. Individual events are colourised according to the trajectory depression angle. The line indicates the azimuth from the receiving station towards the transmitter T.

Examination of the position of trajectory depression angles either side of the line shows shallow angles close to the line and steeper angles further away. This emphasises the dependence of specular reflection on the TMR geometry and tangency of trajectories to ellipsoids; there are only a few shallow angle trajectories close to the TR line. German (2020) developed a Monte Carlo model of head echo Doppler shift calculated at locations between the transmitter and receiver. The model used a flat rather than curved surface for the Earth. It predicted a "no-go" or exclusion zone above the TR line where the zero Doppler shift condition would not be met. This situation can be visualised by imagining a card representing the tangent plane pinned to the ellipsoid containing the tangent point. In Figure 1 at point Z, directly over the TR line and above the midpoint between T and R, trajecto-

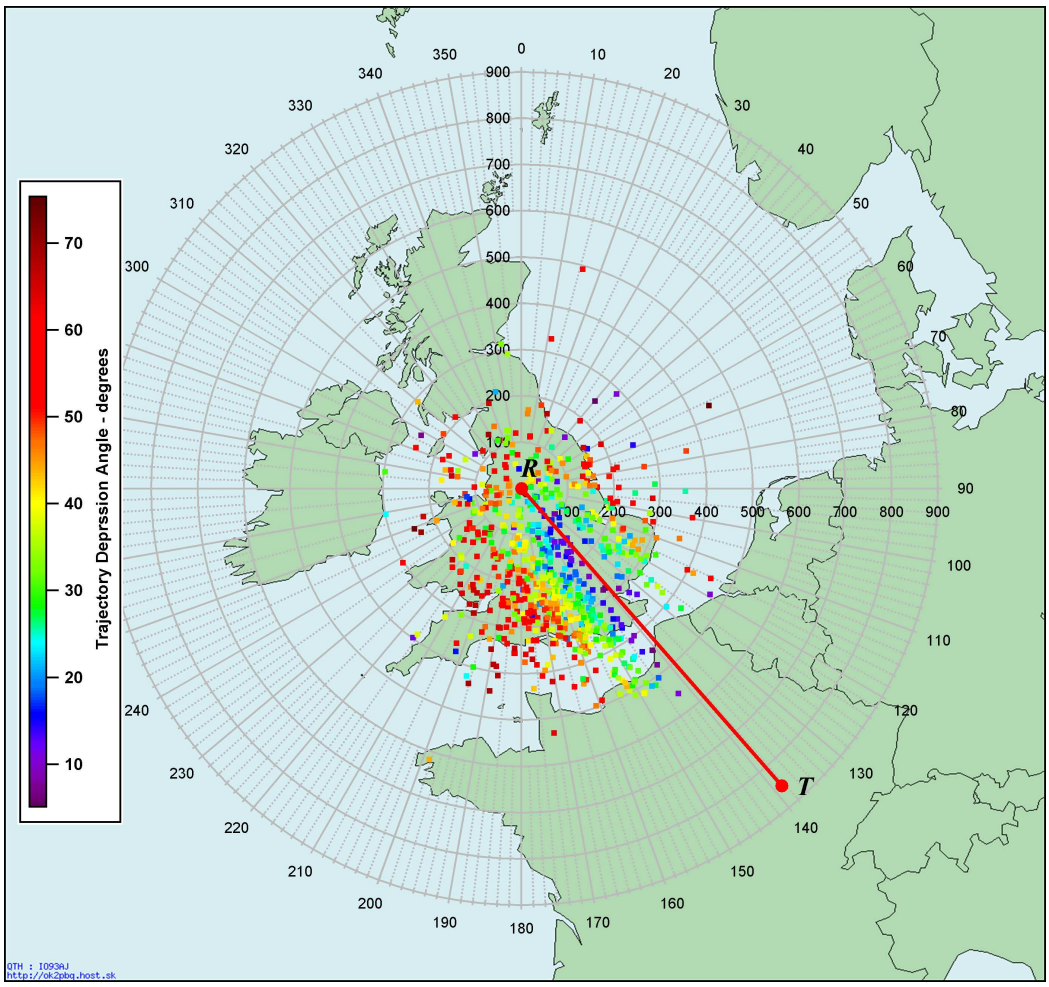

Figure 20 – Azimuth-Ground Range of Radio Video matches centered on Hayfield, UK. Trajectory azimuth angles are indicated by colour. The direction of GRAVES from Hayfield is shown by line RT.

ries in the plane of the card could be in any azimuthal direction but would have zero depression angles – atmospheric glancing or skimming angles. As point Z is moved over the ellipsoid above the TR line towards, say, the receiver station R the possible acceptance angles increase but would remain limited to a small range of values. In a similar manner any tangent point on any ellipse (at meteor altitudes) will be selective in possible trajectory angles of depression. The effect of this can be clearly seen in Figure 20. It will also be evident that trajectories are generally directed away from the TR line.

There are more matches to the west of the RT line at azimuths 138° to 318°. This could have arisen from a number of causes:

- video camera coverage
- local geographical constraints
- receiver antenna patterns
- transmitter radiation pattern

Video cameras coverage, Figure 15, showed about 60% of the stations to the east of the RT line. The area to the north east appeared to be covered. However, McIntyre (2023) informs that cameras on the east coast of the UK are limited and most are directed inward towards the mainland. The relative number of video detections on either side of the line is not known.

The elevation angles of local hills around Hayfield are shown in Figure 21. The azimuth and elevation angles, taken at the end of the head echo, as seen from Hayfield are shown for the four antennas. Overall, meteoroid elevations are between about 8° and 78°. Generally more meteoroids were detected at elevations between 8° and 30°. There is no clustering of events close to the local horizon and it reasonable to assume that the hills did not curtail radio detection. The gap around the RT line at 138° is evident.

An inspection of individual antennas detections in Figure 21 showed the two vertical pointing three-element loop fed Yagis, D1 and D2, had best coverage of altitudes. There was little evidence of an expected increased detection from "element-broadside" directions. There were differences in signal levels and it is possible radiation pattern performance resulted in both providing similarly acceptable SNRs. The ground plane vertical SP-V and the two-element loop-fed quad SP-H, were deployed for a shorter time than the other two antennas. However, it is possible to see that detections were as would be expected from their design; SP-V has better detection at wider azimuth angles and is poor at higher elevation angle, and the directional SP-H has limited detections away for the maximum of the radia-

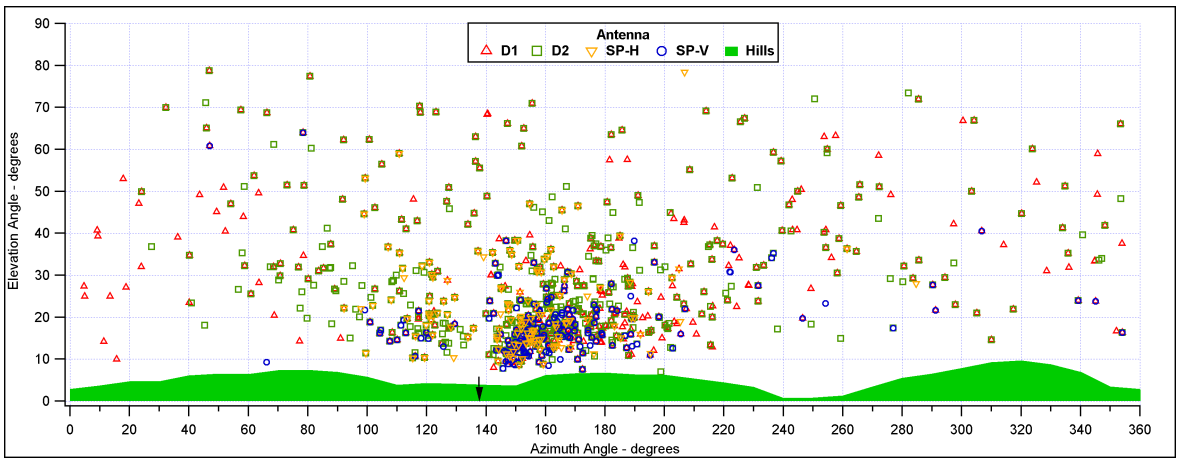

Figure 21 – Azimuth-Elevation Angles of R-V Matched Meteoroids from Hayfield using four Antenna. The Arrow indicates the azimuth of GRAVES from Hayfield.

tion pattern. Overall it was concluded that there was no particular detection directional bias from the antennas that would account for the side to side differences.

An exercise in autumn 2020 to measure the GRAVES transmitter radiation pattern using radio detection of the International Space Station (ISS) was discussed in Section 3. The important factors are the azimuthal and elevation angle from GRAVES where the ISS was observed rather than position. Figure 8 showed a dearth of detections in the 330° to 10° azimuth sector. Observers in Southern England and the Republic of Ireland belonging to the Collaborative Database (2020) group, conducted similar ISS measurements (see Contributor ISS radio map pages) earlier in the year and found few detections in that sector. In 2014 Navaro et al. had combined telescope and GRAVES Doppler detection to track ISS orbits. Their findings were somewhat different to the more recent measurements. Interpretation of their results was difficult but a few detections were judged by the author to be within the sector. It seems improbable for the low number of detection in the sector to have arisen from lack of ISS orbital coverage or persistently poor orientation of large radio scattering structures such as solar panels.

In summary, the low number of R-V matches most probably arises from the low radiation from the GRAVES transmitter and the limited video cameras directed towards that sector.

7.4 Fusion of Radio and Video Meteor data

In Figures 22 and 23 the heights of first head echo detection are compared with geocentric velocity and the estimated mass. Data from all of the antenna systems are shown on the plots and therefore some matched events are represented by more than one head echo. Where the head echo detection occurred before the video detection the height used in the plots was obtained by backward extrapolation. In Figure 22 there appears to be a trend of increased detection height with velocity. The result is rather surprising considering the variations in distances from transmitter and receiver, the radiation patterns of receiver antennas, and the

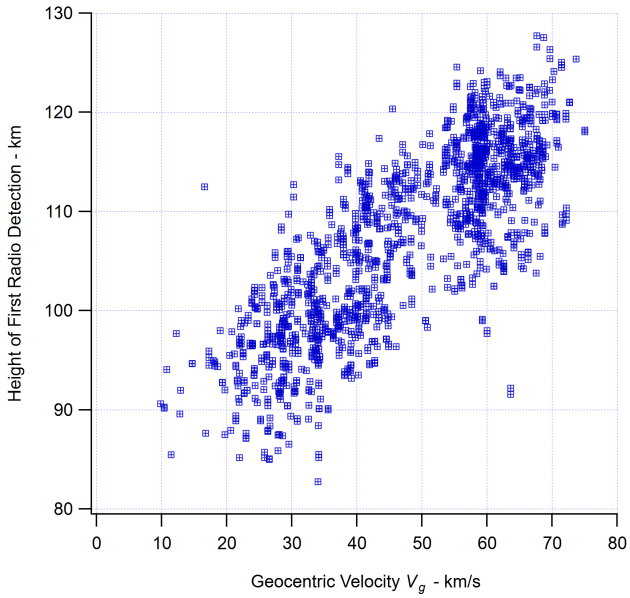

Figure 22 – Height of first radio detection as function of geocentric velocity V_g. All radio antenna systems.

mass and angles of meteoroid trajectory which all contribute towards the signal level and hence detectability by the receivers. Nevertheless, it is reasonable to consider faster[k] meteoroids will generate more ionisation than slower. The spread in heights at given velocities could be interpreted as the result of the various influences resulting in detection, mentioned earlier. There does not appear to be correlation between detected height and meteoroid mass and Figure 23 is shown to indicate the range of estimated[l] masses found.

A period during the Perseids shower is shown in Figure 24 where the elevation angles of meteoroid positions are compared with the altitude angle of the radiant. The events are colourised by geocentric velocity V_g. Elevation is in very good agreement with computed

[k]Whereas the faster meteoroids showed this apparent trend, there appeared to be no correlation between detection height and kinetic energy.

[l]UK Meteor Network notes: *"mass is a lower estimate based on the measured emitted energy and will significantly underestimate the mass of bright events"*

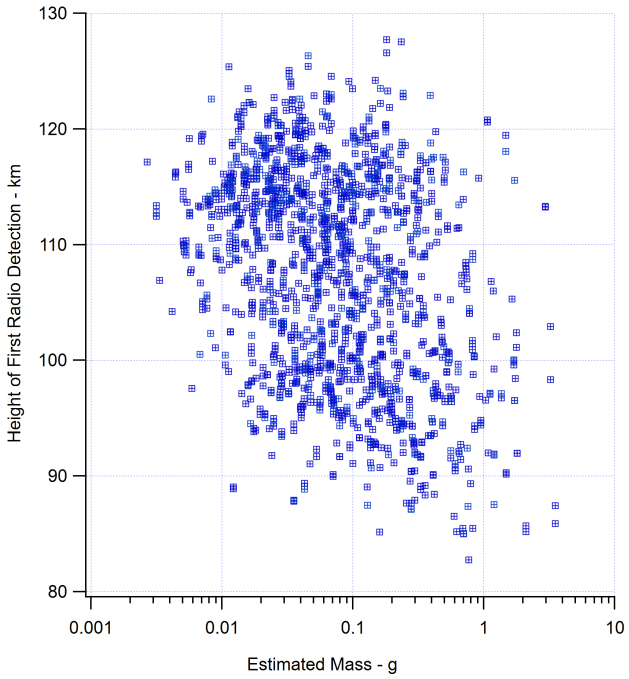

Figure 23 – Height of first radio detection as function of estimated mass. All radio antenna systems.

altitude angle and velocities are in line with Perseids meteoroids. Other non-Perseids detections are readily identifiable by velocity and non-alignment with the radiant altitude.

8 Conclusions – an assessment of objectives

The minimum in total slant range in the radio TMR geometry derived from video meteor trail positions provides a precise match between radio and video camera detections. In the 2022 year, 834 video camera trails were definitively associated with radio detections providing insight of receiving station and meteoroid characteristics. The processes were actioned at the push of virtual buttons. Although the match yield was low, significant experimental evidence of detection distribution around the receiver location and towards the transmitter was obtained. The technique provided a new range of hitherto unattainable radio meteor characteristics relating to head echoes. Backward extrapolation from video data gave the altitude of first radio detection – some at heights above video detection. The velocity, mass and magnitude (bearing in mind the UK Meteor Network caveat on the latter two items) scoped what had been detected as head-echoes:

- masses (estimated) from 27 mg to 3.5 g,
- velocities (from V_g) from 9.85 to 75.03 km/s,
- heights of first head echo detection 83 to 128 km,
- an apparent relationship between height of first head echo detection and velocity,
- heights of zero Doppler shift / specular reflection 73 to 118 km,
- the combination of antennas provided all-round detection,
- elevation angles at receiving station ranged from 7.5° and 78.7°,
- detection ranges from receiving station were from 17 to 626 km.

It was possible, for the first time, to relate individual radio meteors directly with the particular originating shower radiant.

The nature of radio meteor detection and association with the ellipsoids with foci at transmitter and receiver can be readily envisaged from the RV match polar plots: the direction generally away from the TR line. The meteoroid depression angle leads to a clearer understanding of the predicted "exclusion zone" (at least for the author) whereby only the shallowest angles close to the TR line can achieve tangency and result in specular reflections and detection. This region around the transmitter–receiver line where geometry precludes, or at least limits, certain meteoroid trajectory angles,

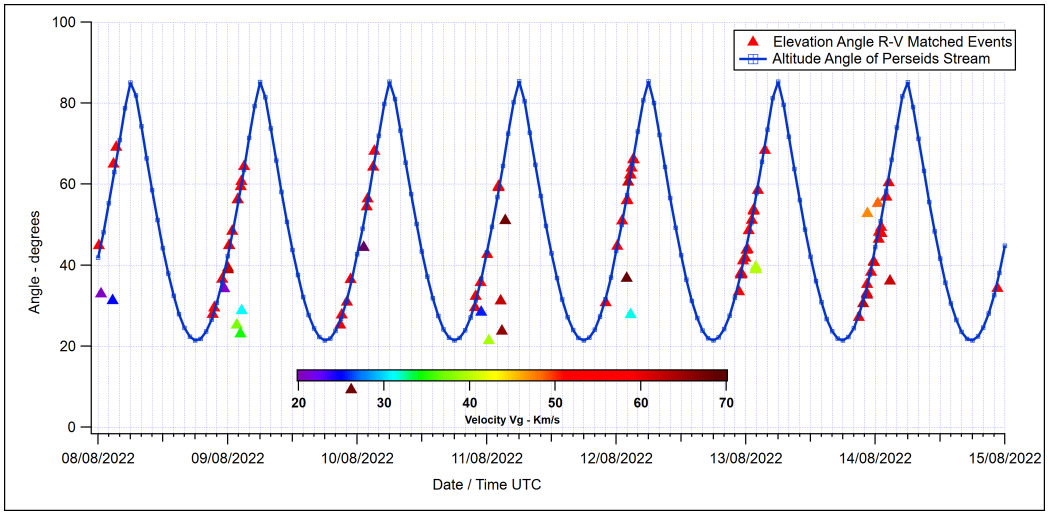

Figure 24 – Elevation angle of meteoroid head echoes compared with Perseids radiant altitude. Events are colourised to indicate velocity.

would impinge on shower detection levels, as the radiants transit the volume.

At the outset of the project an objective was to have another measure of velocity based on the rate of change of head echo Doppler frequency with time. Therefore only head echoes of acceptable duration were used. However, velocities determined in this way suffered from the practicalities of measuring real head echo with slopes that were not always straight. Although calculation of velocity from the video trail, V_M, added confidence to the given value of the geocentric velocity, and the determination of synthesized Doppler and Fresnel zone width gave reasonable agreement, the velocities obtained using head echoes deviated significantly. It is therefore concluded that whereas the exercise to use head echoes in this way was instructive, there was no benefit over using video trail data.

A more stringent algorithm to identify analysable head echoes may improve velocity determination to an acceptable level but the yield of matching radio-video events would inevitably be reduced. Thus, in light of the already low match yields, rather than attempting to improve velocity determination, a relaxation in match requirements would improve the number of matches to the benefit of the other meteor properties that are obtained. The vast majority of all radio meteor detections are those of the simple type – a specular reflection with or without a head echo. Relaxing the requirement of the algorithm to include all events with evidence of a head echo should still allow the use of the same minimum total slant range approach. Where the event has only the specular reflection part it is possible that the starting time may correspond to the time of tangency and application of the match test could also show the proximity of a minimum.

Having demonstrated that reasonably accurate Fresnel width can be obtained from the match technique, it is worthwhile considering the use of Fresnel oscillations (seen in the radio meteor signature at Figure 9) to calculate the meteoroid velocity. See for example the note in Verbelen (2019).

There is benefit in having more than one receiving antenna with complementary radiation patterns, but having these does not even double the number of detections. Cameras in the UKMON network are limited to the UK and Belgium. The FRIPON[m] network which provides very good coverage of France has potential to perhaps double the R-V match region covered. However, FRIPON data for the 2022 year covered by this study had not been released at the time of writing.

The RV match approach should provide an important addition to single station forward scatter meteor monitoring. The symbiosis of radio with video provides new knowledge and understanding for the radio observer and begins to answer the where, what and how of radio meteor detection.

[m]FRIPON (2013) Fireball Recovery and Inter Planetary Observation Network, `https://fireball.fripon.org/list_multiple.php`

Acknowledgements

I am indebted to all the contributors to the UK Meteor Network, without whom this paper would not have been possible. Data from the network are copyright of UK Meteor Observation Network 2013–2023 and is licensed under a Creative Commons BY 4.0 International License `https://creativecommons.org/licenses/by/4.0/`. Particular thanks are due to Mark McIntyre of UK Meteor Network for his tireless response to question on the data and workings of the Network and for comments on the original draft. I appreciate the many discussions over the years with my friend Wolfgang Kaufmann, for Meteor Logger and his explanations of its operation, and for his comments on the draft. The technical support staff of Igor Pro answered countless queries and enabled my coding to work as intended. John Berman of the Collaborative Database gave useful advice in developing the ISS look-up method.

References

Bourdillon A., Haldoupis C., Hanuise C., Le Roux Y., and Menard J. (2005). "Long duration meteor echoes characterized by Doppler spectrum bifurcation". *Geophysical Research Letters*, **32:5**, L05805.

Büscher W. (2023). "Spectrum Lab Software Download". `https://www.qsl.net/dl4yhf/spectra1.html` .

Collaborative Database (2020). `https://radiometeordetection.org/Radioproject` .

Diehl G. (2008). "NTP Time Server Monitor Download". `https://www.meinbergglobal.com/english/sw/ntp.htm` .

Dyrud L., Wilson D., Boerve S., Trulsen J., Pecseli H., Close S., Chen C., and Lee Y. (2008). "Plasma and Electromagnetic Simulations of Meteor Head Echo Radar Reflections". *Earth Moon and Planets*, **102:1-4**, 383–394.

Ernotte P. (2018). "Forward Scattering : an interesting formula to calculate the velocity of a meteoroid that generates a head echo". *WGN, Journal of the IMO*, **46:6**, 198–200.

Fleet R. (2015). "Correlating video meteors with GRAVES radio detections from the UK". In Rault J.-L. and Roggemans P., editors, *Proceedings of the International Meteor Conference, Mistelbach, Austria, 27–30 August 2015*. International Meteor Organization, pages 30–32.

FRIPON (2013). "Fireball Recovery and Inter Planetary Observation Network". `https://fireball.fripon.org/list_multiple.php` .

German M. T. (2020). "A Head Echo Doppler Model for Assessment of Meteoroid Forward Scatter Characteristics". *WGN, Journal of the IMO*, **48:1**, 4–11.

Hardenberg R. (2021). "Graves Radar Update April 2021". http://www.itr-datanet.com/~pe1itr/graves/graves-update-20210408.htm .

Igor Pro (1994). "Scientific data analysis software, numerical computing environment and programming language". https://en.wikipedia.org/wiki/IGOR_Pro .

Janches D., Hocking W., Pifko S., Hormaechea J. L., Fritts D. C., Brunini C., Michell R., and Samara M. (2014). "Interferometric meteor head echo observations using the Southern Argentina Agile Meteor Radar". *Journal of Geophysical Research: Space Physics*, **119:3**, 2269–2287.

Jouadé A. and Barka R. (2019). "Massively Parallel Implementation of FETI-2LM Methods for the Simulation of the Sparse Receiving Array Evolution of the GRAVES Radar System for Space Surveillance and Tracking". *IEEE Access*, **7**, 128968–128979.

Kaufmann W. (2017). "New radio meteor detecting and logging software". *WGN, Journal of the IMO*, **45:4**, 67–72.

Kaufmann W. (2018). "Visualizing meteor streams by radio forward scattering on the basis of meteor head echoes". *WGN, Journal of the IMO*, **46:1**, 39–44.

Kaufmann W. (2020a). "Enhanced radio detectability of forward scattered head echoes passing zero Doppler shift". *WGN, Journal of the IMO*, **48:4**, 108–111.

Kaufmann W. (2020b). "Limitations of the observability of radio meteor head echoes in a forward scatter setup". *WGN, Journal of the IMO*, **48:1**, 12–16.

Lamy H., Balis J., and Anciaux M. (2021). "Reconstructing meteoroid trajectories using BRAMS data". *WGN, Journal of the IMO*, **49:6**, 195–200.

Marshall R. A. and Close S. (2015). "An FDTD model of scattering from meteor head plasma". *Journal of Geophysical Research: Space Physics*, **120:7**, 5931–5942.

McIntyre M. J. M. (2023). "From UK Meteor Network of Matched camera trails". personal communication.

McKinley D. W. R. (1961). *Meteor science and engineering*. McGraw-Hill, New York.

Michal T., Eglizeaud J. P., and Bouchard J. (2005). "Graves: the New French System for Space Surveillance". In Danesy D., editor, *4th European Conference on Space Debris*, volume 587 of *ESA Special Publication*. page 61.

Navara M., Matousek M., and Drbohlav O. (2014). "Fusion of Telescopic and Doppler Radar Data". In Ryan S., editor, *Proceedings of theAdvanced Maui Optical and Space Surveillance Technologies Conference*. page E84.

Norton P. (2016). "Understanding the amount of Power Graves Transmits North towards Meteors". personal communication.

Ordnance Survey (2015). *A guide to coordinate systems in Great Britain*. D00659 v2.3.

Powell C. (2019). "Automated Spectrogram Analysis for Meteor Head Echoes". *WGN, Journal of the IMO*, **47:2**, 55–65.

SDRPlay (2014). "SDR Software for RSPduo and RSP2". available at http://sdrplay.com/sdruno/.

Steyaert C., Verbelen F., and VVS Beacon Observers (2010). "Meteor Trajectory from Multiple Station Head Echo Doppler Observations". *WGN, Journal of the IMO*, **38:4**, 123–129.

UK Meteor Observation Network (2013). https://ukmeteornetwork.co.uk/ .

Vallejo M. (2015). "Determining the radiant of a meteor using Graves radar". https://ea4eoz.blogspot.com/2015/05/determining-radiant-of-meteor-using.html .

Verbeeck C. (1995). "The First Fresnel Zone and the Power Profile Throughout the Forward Scattered Reflection Surface". In Roggemans P. and Knöfel A., editors, *Proc. IMC (Brandenburg) 1995*.

Verbeeck C. (2023). personal communication.

Verbeeck C. and Rault J.-L. (2022). "Radio meteor observations". In Rendtel J., editor, *IMO Handbook for Meteor Observers*, chapter 6, pages 119–138. International Meteor Organization.

Verbelen F. (2019). "Meteor velocity derived from head echoes obtained by a single observer using forward scatter from a low powered beacon". *WGN, Journal of the IMO*, **47:2**, 49–54.

Wilschut H. W. (2020). "Frequency shifts of head echoes in meteoroid trail formation". *WGN, Journal of the IMO*, **48:4**, 112–117.

Wislez J.-M. (1995). "Forward scattering of radio waves off meteor trails". In Roggemans P. and Knöfel A., editors, *Proc. IMC (Brandenburg) 1995*.

Handling Editor: Javor Kac

Annex A. Summary of Geodetic Calculation

Video camera databases report meteor trajectories as time series' of latitude, longitude, and height, based on EGM96 (Earth Gravitational Model) which includes the WGS84[n] standard (World Geodetic System). WGS84 takes into account the oblate spheroid shape of Earth and EGM96 the variations in surface height above and below WGS84 datum. See Ordnance Survey (2015) for for more detail. In practice, in the UK and neighbouring regions of Europe, the EGM96 geoid heights are small and add little to the WGS84 ellipsoid.[o] Any correction would be small compared to meteor heights and in this paper the EGM96 geoid heights have not been used.

Annexes A1 to A4 contained the algorithms for calculation of Earth parameters based on WGS84. Functions were written in the Igor Pro programming language but should be readily translatable to other platforms.

A1. WGS84 Distance from Earth Centre

```
Function WGS84EarthRadius(Lat)
  // returns the WGS84 Earth radius Rlat at Latitude Lat
    variable Lat                  // WGS84 Latitude for calculation - degrees
    variable a = 6378.137         // semi-major axis of WGS84 reference ellipsoid  km
    variable b = 6356.752314245   // semi-minor axis of WGS84 reference ellipsoid  km
    variable RadEarth =  6371     //  Mean radius of Earth km
    variable Rlat                 // Earth radius at latitude Lat
    Lat = Lat * pi /180           // convert latitude degrees to radians
    Rlat =  sqrt(((a^2*cos(Lat))^2+(b^2*sin(Lat))^2)/((a*cos(Lat))^2+(b*sin(Lat))^2))
  return Rlat
end
```

A2. WGS84 Chord Length

```
Function WGS84ChordLength(lat1,lon1,lat2,lon2)
  // Returns the chord length between two points on WGS86 reference ellispsoid
  // From https://planetcalc.com/7725/
    variable lat1,lon1,lat2,lon2          // WGS84 coordinates in decimal degrees
    variable x1,y1,z1,x2,y2,z2            // Cartesian coordinates
    variable chord                        // Chord length - km
    Variable R1,R2                        // radius at WGS84 latitude km
    variable theta1,phi1,theta2,phi2      // angles in geocentric coordinates
    variable a = 6378.137                 // semi-major axis WGS84 reference ellipsoid km
    variable b = 6356.752314245           // semi-minor axis WGS84 reference ellipsoid km
    // radii at WGS84 latitudes km
    R1 = WGS84EarthRadius(Lat1)
    R2 = WGS84EarthRadius(Lat2)
    // convert angles degrees to radians
    lat1 = lat1 *pi/180
    lat2 = lat2 *pi/180
    lon1 = lon1 *pi/180
    lon2 = lon2 *pi/180
    // convert angles to geocentric
    theta1 = atan((b*tan(lat1))/a)
    phi1   = lon1
    theta2 = atan((b*tan(lat2))/a)
    phi2   = lon2
    // cartesian coordinates
    x1 = R1*cos(theta1)*cos(phi1)
    y1 = R1*cos(theta1)*sin(phi1)
    z1 = R1*sin(theta1)
    x2 = R2*cos(theta2)*cos(phi2)
    y2 = R2*cos(theta2)*sin(phi2)
    z2 = R2*sin(theta2)
    // Chord length
    chord = sqrt((x2-x1)^2 +(y2-y1)^2+(z2-z1)^2)
  return chord
end
```

[n] https://en.wikipedia.org/wiki/World_Geodetic_System#WGS84

[o] Ordnance Survey (2020), private communication

A3. WGS84 Azimuth Angle

```
Function WGS84Azimuth(lat1, lat2, lon1, lon2)
  // Takes Coordinates at Location 1 and 2 and calculates Azimuth of 2 from 1
  // Developed from wikipedia azimuth geodesy https://en.wikipedia.org/wiki/Azimuth
     variable lat1, lat2, lon1, lon2 // latitude & longitude of the 2 points in degrees
     variable dLat, dLon             // delta latitudes and longitudes
     variable azimuth                // Azimuth in radians then-> degrees
     variable e = 1/298.257223563    // oval Earth eccentricity WGS84
     variable lambda                 // used in part equation
  // convert coordinates in degrees to radians
     lat1 *= Pi/180
     lon1 *= Pi/180
     lat2 *= Pi/180
     lon2 *= Pi/180
  // angular location coordinate differences in radians
     dLat = lat1 - lat2
     dLon = lon1 - lon2
     lambda = (1-e^2)*(tan(lat2)/tan(lat1))+e^2*sqrt((1+(1-e^2))*
              (tan(lat2)^2)/(1+(1-e^2)) * (tan(lat1)^2))
     Azimuth = atan(sin(dlon) / ((lambda-cos(dlon))*sin(lat1)))
  // Convert Radians to Degrees
     Azimuth *= 180/pi
  // Select Trigonometrical Quadrant of target azimuth
     if (azimuth<0)
          azimuth +=180
     endif
  // Target in 1st Quadrant. dLat<0 and dLon<0 azimuth <0  NE Q1
     if ((dLat<0) && (dLon<0))
          azimuth = 180 - azimuth
     endif
  // Target in 2nd Quadrant. dLat<0 and dLon>0 azimuth >0  NW Q2
     if ((dLat<0) && (dLon>0))
          azimuth = 360 - azimuth
     endif
  // Target in 3rd Quadrant.  dLat>0 and dLon>0 azimuth < 0  SW Q3
     if ((dLat>0) && (dLon>0))
          azimuth = 360 - azimuth
     endif
  // Target in 4th Quadrant.  dLat>0 and dLon<0 azimuth > 0  SE Q4
     if ((dLat>0) && (dLon<0))
          azimuth = 180 - azimuth
     endif
    // Same Latitude, target to East
     if ((lat2==lat1) && (dlon<0))
          azimuth = 90
     endif
  // Same Latitude, target to West
     if ((lat2==lat1) && (dlon>0))
          azimuth = 270
     endif
  // Same Longitude Target south
     if ((dlat>0) && (dlon==0))
          azimuth = 180
     endif
  return azimuth
end
```

A4. WGS84 Elevation Angle

```
Function WGS84Elevation(slantDistance,rad1,rad2,Height)
  // Takes slant distance between two points at WGS84
  // Earth radii rad1 and rad2 and Height of meteor
  // Return Elevation angle in degrees
     variable slantDistance     // Distance from point 1 on surface to point 2 (meteor)
     variable rad1              // WGS84 Earth Radius at location 1
     variable rad2              // WGS84 Earth Ratius at location 2 (meteor)
     variable Height            // Height of meteor at Location 2
     variable elevation         // calculated elevation angle
     variable a, b, c, d, cosAngle
  // Cosine rule
     a = rad1
     b = slantDistance
     c = height + rad2
     cosAngle = (b*b + a*a - c*c) / (2*a*b)
     d = acos(cosAngle)          // radians
  // convert to degrees
     elevation = (180/pi * d) - 90
  return elevation
end
```

Halley Type and Long Period Meteor Shower Luminous Altitude Characteristics

Yasuo Shiba[1]

The luminous-altitude statistics for Halley-type and 115 long-period meteor showers were investigated by using 15 years of data from the SonotaCo network. The processing sequence took into account known influencing factors for the luminous altitude and successively removed their effect. As a result, two new factors were identified, these being orbital perihelion distance and the meteor shower's stage of evolution. These were not identified by previous research which had identified the factors of geocentric velocity, radiant elevation angle, and mean luminous magnitude. It is concluded that the meteoroids were affected by metamorphism when close to the Sun. A possible mechanism for metamorphism by the Sun is as follows. (1) Parts of the meteoroids are removed by vaporization. (2) Mechanically weak materials on the meteoroid surface are removed. (3) Empty parts of the meteoroids vanish, thus increasing the density and hardness. (4) Mechanically weak meteoroids like "dust balls" disintegrate or are taken away from their meteor orbit. The correlation with the solar cycle was researched for six major meteor showers, five of which show a positive correlation, but no correlation was seen for the Perseids. The luminous altitude for #246 AMO was low. This meteor shower's chemical or mechanical features might be unique as might be the meteor shower's characteristic evolution. Other exceptional luminous-altitude meteor showers are pointed out.

Received 2023 March 22, revised 2023 August 16

1 Introduction

Meteoroids enter the Earth's atmosphere from the vacuum of space. We can observe them as meteors when the atmospheric density they encounter is sufficient to cause them to radiate light or produce plasma to reflect radio waves. The luminous altitude of meteors is determined by so many factors. During the photographic observation era using the Super-Schmidt cameras, meteor luminous altitude differences were explained by origin of the meteoroid material – comets or asteroids (Cook, 1970). Accumulation of many photographic observations brought out that the principal cause is meteor velocity, which is confirmed also by many TV observations (e.g.: Sarma & Jones, 1985) and more especially for the sporadic meteors (Roggemans, 2017). The velocity effect is the most important factor because the meteoroid's luminous energy is generated by its kinetic energy. The kinetic energy is proportional to the square of the velocity and proportional to the mass. Thus, the velocity is the most influential factor regarding meteor light emission and this is the reason that meteor light emission can occur in the attenuated atmospheric environment at high altitudes. The meteoroid cross-sectional area also influences luminous altitudes. If the meteoroid has a broad cross-section, collision with many atmospheric molecules can lead to the earlier emission of light at high altitudes. Different types of wider cross-section meteoroids even exist for meteoroids of the same mass. One is meteoroids that are low-density from the start. Next, there is the fragmentation of meteoroids in the atmosphere. A few types of fragmentation are already considered for low-velocity meteors mainly. One of these is gross fragmentation (Ceplecha & Revelle, 2005). The next is quasi-continuous fragmentation (Babadzhanov, 2002). Furthermore, there is the melting meteor phenomenon (Ward, 2016) in which whole fragmentation occurs instantly, considered to originate from very easily broken meteoroids. Many volatile matter materials contained in meteoroids are possible to make an enhanced plasma that radiates visible or infrared light. It may be highly effective for low-velocity meteors that allow a longer time for meteoroid material to heat and evaporate. Recently, fast ($V_g >\sim 60$ km/s) fireballs in extremely high altitudes (130–170 km) were observed by TV cameras (Fujiwara et al., 1998; Koten et al., 2006; Spurný et al., 2000) and also by radio observations (Li et al., 2014). It was explained that the air molecules spattering to the meteoroid's surfaces produced plasma cascades. Its high altitude spectrum indicates abundant infrared light produced by Oxygen and Nitrogen (Spurný et al., 2014). The extremely high altitude meteor diffusion images accompanied by jets are understood to differ from the general height meteor luminous mechanism (Vinković, 2007; Spurný et al., 2014). We must also pay attention to variations in the comparatively static atmospheric structure. There has been research into some factors that might cause the air density to vary at the meteor light emission altitudes of the upper mesosphere or lower thermosphere. Initially, many researchers reported variations in line with the solar cycle based on radio observations (Batubara et al., 2018; Premkumar et al., 2018; Campbell-Brown, 2019). However, a negative result was reported for large Perseid meteoroids, based on Photographic observation (Buček et al., 2012; Porubcan et al., 2012). Radio observations of echo height reported variations that are linked to diurnal motion, seasonal variation for sporadic meteors (Clemesha & Batista, 2006; Roggemans, 2017), planetary wave (Liu et al., 2017), geomagnetic activity (Campbell-Brown, 2019), and mesosphere environment temperature (Lee et al., 2022).

Luminous end height is determined by the meteoroid size becoming too small to emit enough light or the velocity becoming too slow for ablation. Luminous end

[1]SonotaCo Network
Email: kqc43540@biglobe.ne.jp

IMO bibcode WGN-514-shiba-altitude
NASA-ADS bibcode 2023JIMO...51...93S

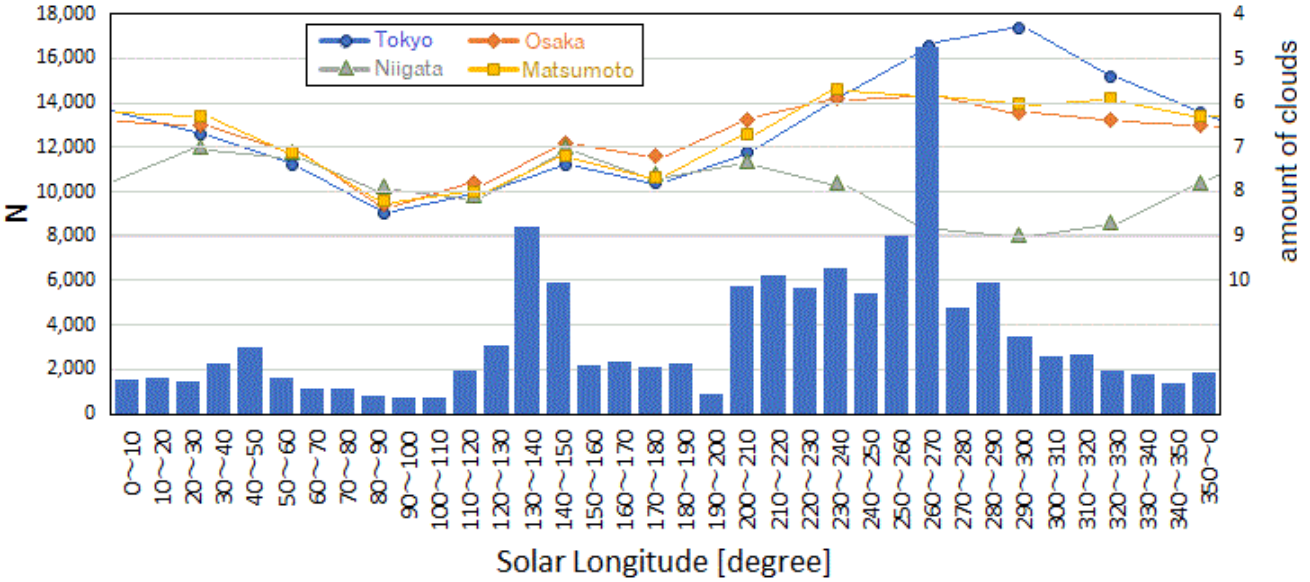

Figure 1 – Meteor orbit number and amount of cloud for the solar longitude

heights for all fast meteors and the majority of other meteors are generally dominated by mass reduction. On the other hand, some sizeable slow velocity meteoroids disappear due to deceleration. Based on SonotaCo network observations, the typical final velocity is about 4 km/s for the general meteorite expectable fireballs. The meteor ending-altitude-determined factors are also complex. High start point meteors feature earlier progressing ablation and this leads to earlier mass loss. The heavy initial mass meteoroids are sure to have long ablation times, delaying their disappearance at low altitudes. The low-velocity meteors have a tendency to having low end points because they have a lower start altitude, reduced fragmentation, and a slower progress of ablation. End altitudes for the high-density meteoroids are also low because they have narrow cross-sectional areas and therefore collide with fewer atmosphere molecules and this delays the ablation progress. If fragmentation occurs, the total cross-section area increases suddenly, and as a result, explosive ablation arises and the meteor disappears earlier. When the meteoroid surface air pressure ($p = \rho v^2$) is stronger than the meteoroid mechanical strength, meteoroid fragmentation occurs. Especially low mechanical strength meteoroids, called "dust balls" (Campbell et al., 2000) will likely have extremely high end altitudes. Meteoroids containing much volatile material will show accelerated ablation and fragmentation and consequently their end height will be higher. Meteor pass elevation angle will influence the end altitude. The artificial orbiter reentry is planned generally to have a low elevation angle and that increased deceleration time can release more heat and extend ablation times. The end altitudes for low-elevation-angle meteoroids were described as being high in (Sarma & Jones, 1985, Table IV: Vidicon). On the other hand, low-entering-angle Perseids meteors bring on low end altitudes that were described as inverse results (Molau & Sonotaco, 2008).

The luminous start and end heights of meteors are influenced by a complex set of multiple factors which have to be combined. Individual meteors belonging to the same meteor shower will show a range of altitudes for each parameter. However, I believe that the statistical characteristics of start and end altitudes for individual meteor showers can be differentiated. SonotaCo Network observation brings us over 100 thousand meteor orbit data from 2007 to 2021 and will fit my purpose. This study's purpose is to investigate the characteristics of meteoroids and the lower thermosphere and upper mesosphere. Previous research (Roggemans, 2017) investigated established meteor showers. In this study, I investigate the Halley type and long-period meteor showers.

2 Method

Basic data on the SonotaCo network's site (SonotaCo, 2009) was downloaded for this study. This data was uploaded and analyzed for each meteor whose image was taken by individual network observers. The data duration is 15 years, from January 2007 to December 2021. Orbit calculation is by UFOOrbitV2 (SonotaCo, 2009). The atmosphere deceleration correction parameter "Voi" was set as 0.3 km/s. The orbital elements were taken from the "unified" data that was derived from all observations. Quality level of the UFOOrbitV2 was taken "Q2" in order that relatively low-quality level data would be rejected. As result, the total number of the orbits included was 126 184. The number of orbits for each 10-degree bin and the amount of clouds in the typical observation district for months (Japan Meteorological Agency, 2022) are shown in Figure 1. The solar longitude from 70 to 110 degrees and from 190 to 200 degrees coincide with the rainy season and thus contribute a rather small quantity of meteor orbits.

Individual meteors are assigned to the relevant meteor shower. The method used follows. Two types of radiant points charts were drawn for each 10-degree solar longitude bin. One had right ascension and declination axes and the second was based on ecliptic longi-

Table 1 – Influence factors for the luminous height.

Factor: brevity code	linear approximation		correl. coefficient	
	begin [km]	end[km]	begin	end
Geocentric Velocity: V_g [km/s]	$H_b = 89.44 + 0.341 V_g$	$H_e = 72.84 + 0.350 V_g$	0.935	0.824
Mean Radiant Elevation Angle: ev [°]	$\Delta H_b = -0.0086\, ev + 0.349$	$\Delta H_e = -0.159\, ev + 6.36$	−0.071	−0.712
Mean Absolute Magnitude: mag	$\Delta H_b = -1.10\, mag - 1.62$	$\Delta H_e = 1.12\, mag + 1.64$	−0.329	0.254
Perihelion Distance: q [au]	$\Delta H_b = 2.04\, q - 1.53$	$\Delta H_e = 3.62\, q - 2.72$	0.367	0.484
Diurnal variation: $LT = UT + 9$ [h]	$\Delta H_b = -0.034\, UT - 0.60$	$\Delta H_e = -0.141\, UT + 2.00$	0.036	−0.114
Yearly motion: SL [°]	$\Delta H_b = -0.613 \sin(SL)$	$\Delta H_e = -0.456 \sin(SL)$	—	—
Radiants Diffusion Index: RDI	$\Delta H_b = -0.395\, RDI + 1.18$	$\Delta H_e = -0.249\, RDI + 0.73$	−0.524	−0.249
D criterion : av_{Dd}	$\Delta H_b = -29.2\, Dd + 1.57$	$\Delta H_e = -17.3\, Dd + 0.90$	−0.592	−0.265
1/(semi-major axis): $1/a$ [au]	$\Delta H_b = 5.69\,(1/a) - 0.36$	$\Delta H_e = 7.00\,(1/a) - 0.45$	0.216	0.177
inclination: i [°]	$\Delta H_b = -0.0072\, i + 0.86$	$\Delta H_e = -0.0062\, i + 0.72$	−0.283	−0.162

tude – solar longitude:ecliptic latitude axes. Assessment of radiant point concentration regions of the chart involved two-step checks being carried out for included members to remove some spurious meteors. One is geocentric velocity, the second is the D criterion (Drummond, 1981) that calculates closeness between a meteor shower's mean orbit and that of individual meteors. The removing D_d criterion threshold is not constantly applied, with other values being used for individual meteor showers between 0.05 – 0.18. Long term continuous concentrated radiants existing over 10 degrees solar longitudes are judged to be one meteor shower. The mean meteor shower data is shown in (Appendix Table A.1). The mean semi-major axis was calculated from mean eccentricity and mean perihelion distances. Research meteor showers were adopted over 5 [au] semi-major axis as Halley-type or long-period meteor showers. The total of researched meteor showers is 122 containing four new meteor showers adding to IAU MDC (Jopek & Jenniskens, 2011; Jopek & Kaňuchová, 2014; Jopek & Kaňuchová, 2017; Jenniskens et al., 2020; Neslusan et al., 2020). One "removed meteor shower" (#89 PVI) deserve to be put back on the working list. For seven meteor showers, it wasn't possible to confirm their existence or find useful data. Forty-one meteor showers are rejected for luminous height research in this study because the number of their meteors was fewer than 30 meteors, judged to be insufficient for statistical study. As a result, luminous heights were studied for 72 meteor showers.

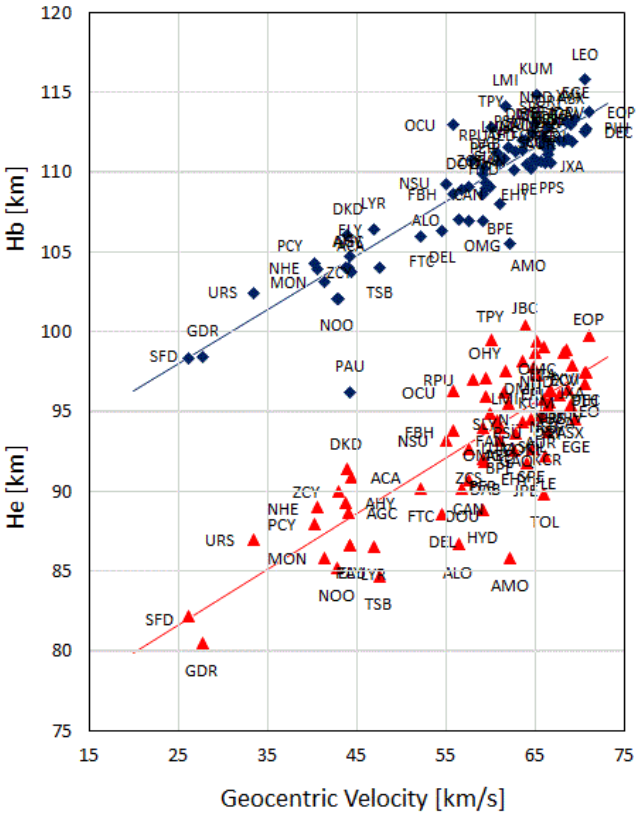

Figure 2 – Meteor shower geocentric velocity and luminous height.

3 Results

The factors that might influence the luminous altitudes of meteors were selected (Table 1: left column) and sequentially researched from top to bottom. The linear approximation and correlation coefficient for each factor were shown in the later columns. Two meteor showers (#183 PAU, #248 AMO) had abnormal luminous altitudes that are described in the "discussion" and were excluded from the Table 1 data calculation. If you want the arbitrary meteor luminous altitude value, you can add total of the columns "linear approximation" in Table 1. The individual factors are explained below.

3.1 Geocentric Velocity (V_g)

The start and end luminous altitudes vs mean geocentric velocity is shown in Figure 2. The upper side diamond mark is the start and the lower side triangle mark is the end altitude. The linear fit is superposed for each altitude. Both show a clear correlation.

3.2 Path Elevation Angle (ev)

Path elevation is the same as the apparent radiant elevation angle. The Figure 3 vertical axis is the deviation between the individual plot point and linear fit in Figure 2. The Figure 3 horizontal axis is the path elevation angle. The low path elevation angle condition leads to high start altitudes and low end altitudes. End height has a strong negative correlation but the negative correlation for the start altitude is small. Two meteor showers #183 PAU and #246 AMO do not agree with the linear fit line at the start height, while only #246 AMO is is out of step with the linear fit line at the end altitude.

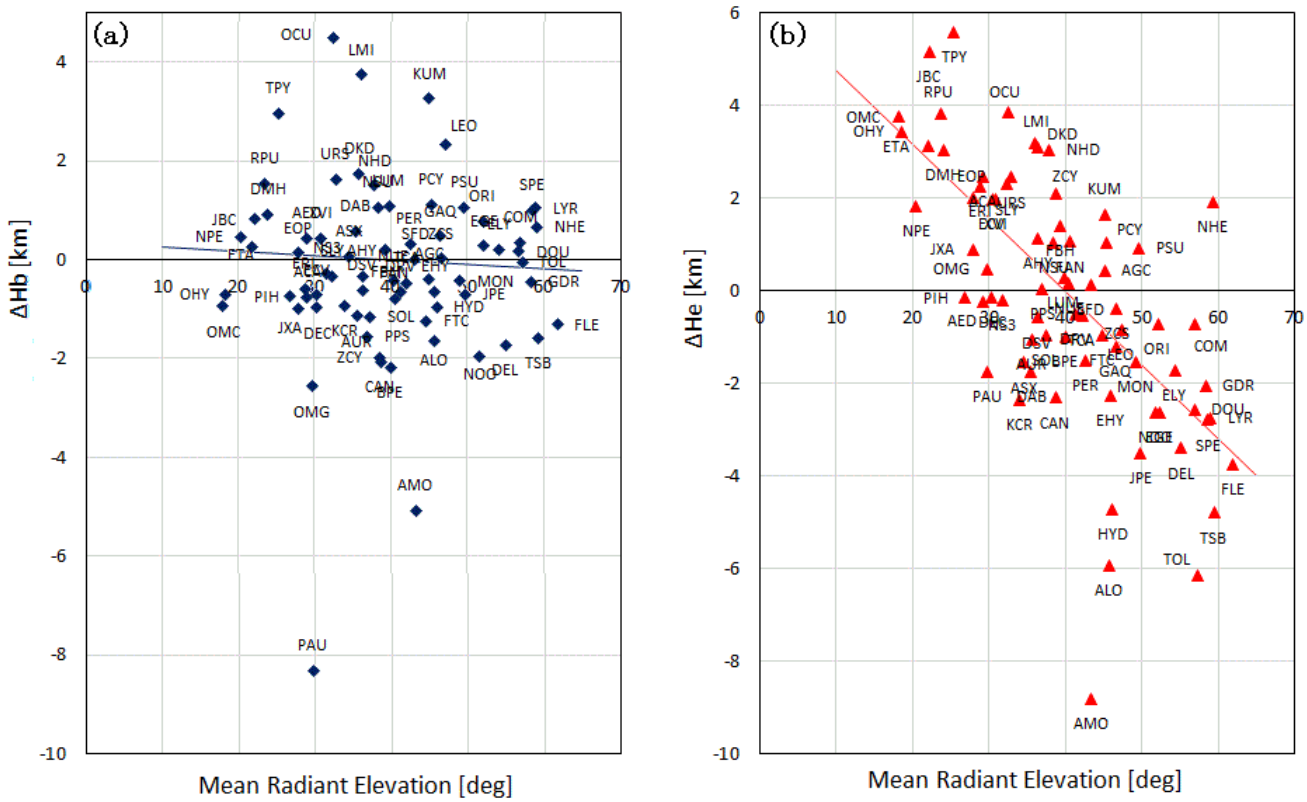

Figure 3 – ΔH_b and ΔH_e for the mean path elevation angle.

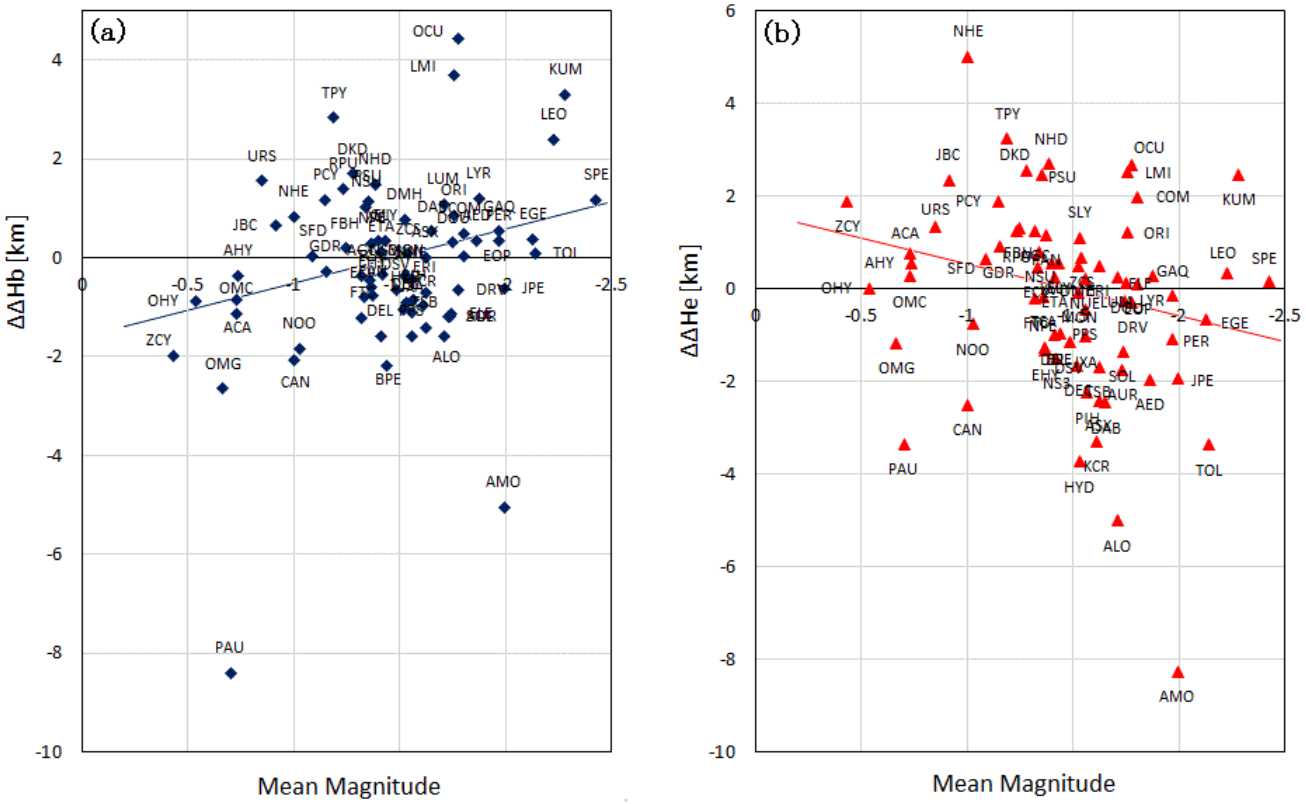

Figure 4 – $\Delta\Delta H_b$ and $\Delta\Delta H_e$ for the mean absolute magnitude.

3.3 Absolute Magnitude (mag)

The Figure 4 vertical axis is the deviation between every plot point and the linear fit in Figure 3. The Figure 4 horizontal axis shows the mean absolute magnitudes of the individual meteor showers. The bright mean absolute magnitude meteor showers have high start altitudes with weak positive correlation and low end altitudes with weak negative correlation.

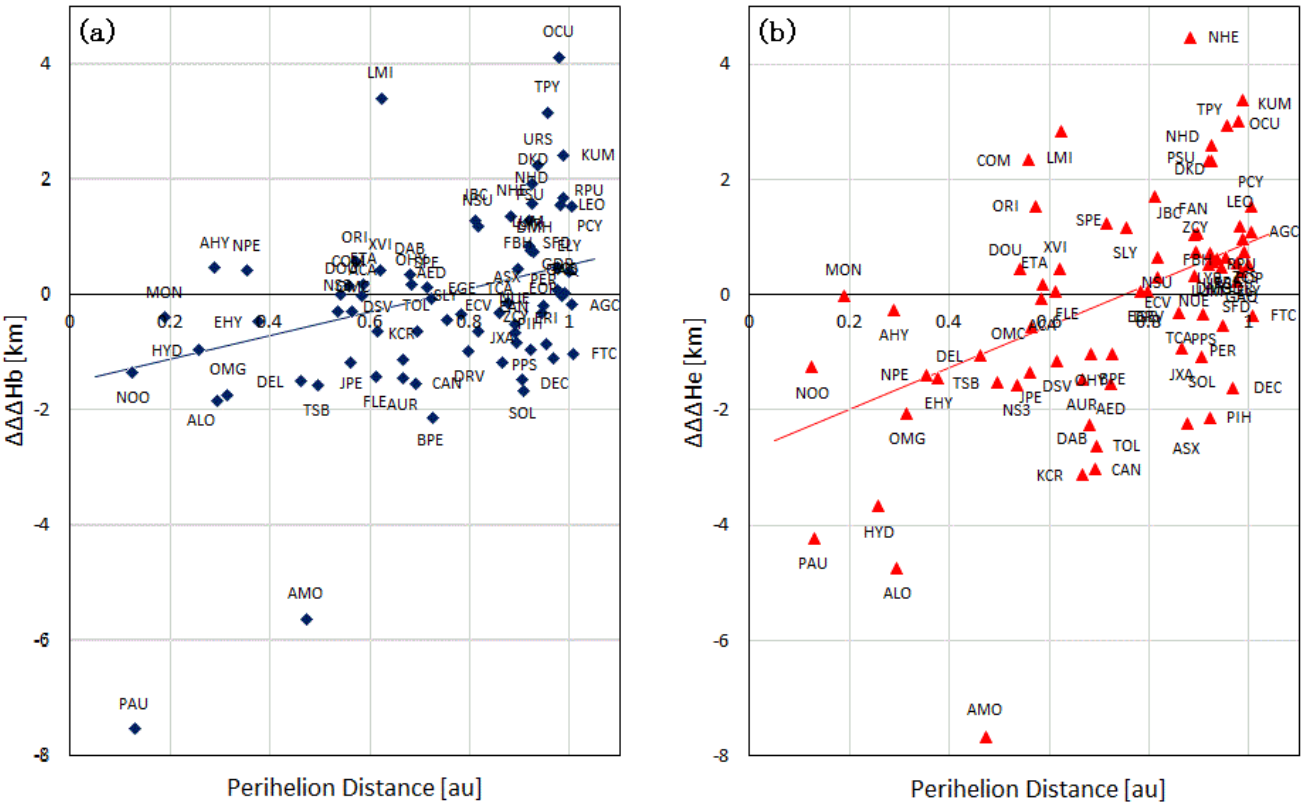

Figure 5 – $\Delta\Delta\Delta H_b$ and $\Delta\Delta\Delta H_e$ for the perihelion distance.

3.4 Perihelion Distance (q)

The Figure 5 vertical axis is the deviation between individual plot points and the linear fit in Figure 4. The Figure 5 horizontal axis shows the mean perihelion distance (q) of the individual meteor showers. Start altitudes are low for small perihelion distances with a weak positive correlation. Near 1 [au] perihelion distance, meteor shower start altitudes are strikingly high and out of step with the linear fit. The end altitude shows a more distinct positive correlation. Note that the extremely low start height meteor shower #183 PAU is close to the Sun.

3.5 Local Time (LT)

The Figure 6 vertical axis is the deviation between individual plot points and linear fit in Figure 5. The Figure 6 horizontal axis is the mean meteor appearance time in UT. The relation between local time and universal time is $UT = Local\ time - 9$ [hr]

Start altitudes show little correlation with local time. End altitudes decreases toward morning twilight with low correlation.

3.6 Seasonal Variation (SL)

The Figure 7 vertical axis is the deviation between individual plot points and the linear fit in Figure 6. The Figure 7 horizontal axis is the solar longitude. The approximation line was taken as the trigonometric functions and is not linear. The approximate sine curve indicates a minimum at the northern hemisphere summer solstice and a maximum at the winter solstice. Start altitude shows a more distinct correlation than does the end altitude but both are almost error-level correlations.

3.7 Radiants Diffusion Index (RDI)

The distribution of meteoroids will have been diverging from the parent body's original solar system orbit since their time of ejection. We can investigate this via observations as orbital diffusion or the concentration level of radiant points. I adopted the radiant points diffusion level as described here: Initially, the mean radiant points were calculated as described (radiant ecliptic longitude – solar longitude) and (ecliptic latitude). Note that if the ecliptic latitude is $\sim \pm 90$ degrees, you must pay attention to the calculation method. Next, the mean angular distance (L) calculates all of the angular differences between individual radiant positions and the mean radiant position. Furthermore, the expanded diffusion effect for low-velocity meteor shower radiants was considered, and the "Radiants Diffusion Index (RDI)" was calculated from "L" and geocentric velocity (V_g). $RDI = L \log(V_g)$ The Figure 8 vertical axis is the deviation between every plot point and the sine curve fit in Figure 7. The Figure 8 horizontal axis is the "RDI". In Figure 8, the right hand side features radiant points from diffused meteor showers that might have completed many orbits since being released from the parent body. The more evolved meteor showers have low luminous altitudes and a strong correlation at the start altitude. The adapted linear fit for Figure 8 may not be so good but the meteor showers may eventually converge towards a constant height as they continue to evolve.

3.8 Orbit diffusion Level (av_Dd)

Orbital diffusion value was evaluated as another meteor shower evolving index. The mean value of the D

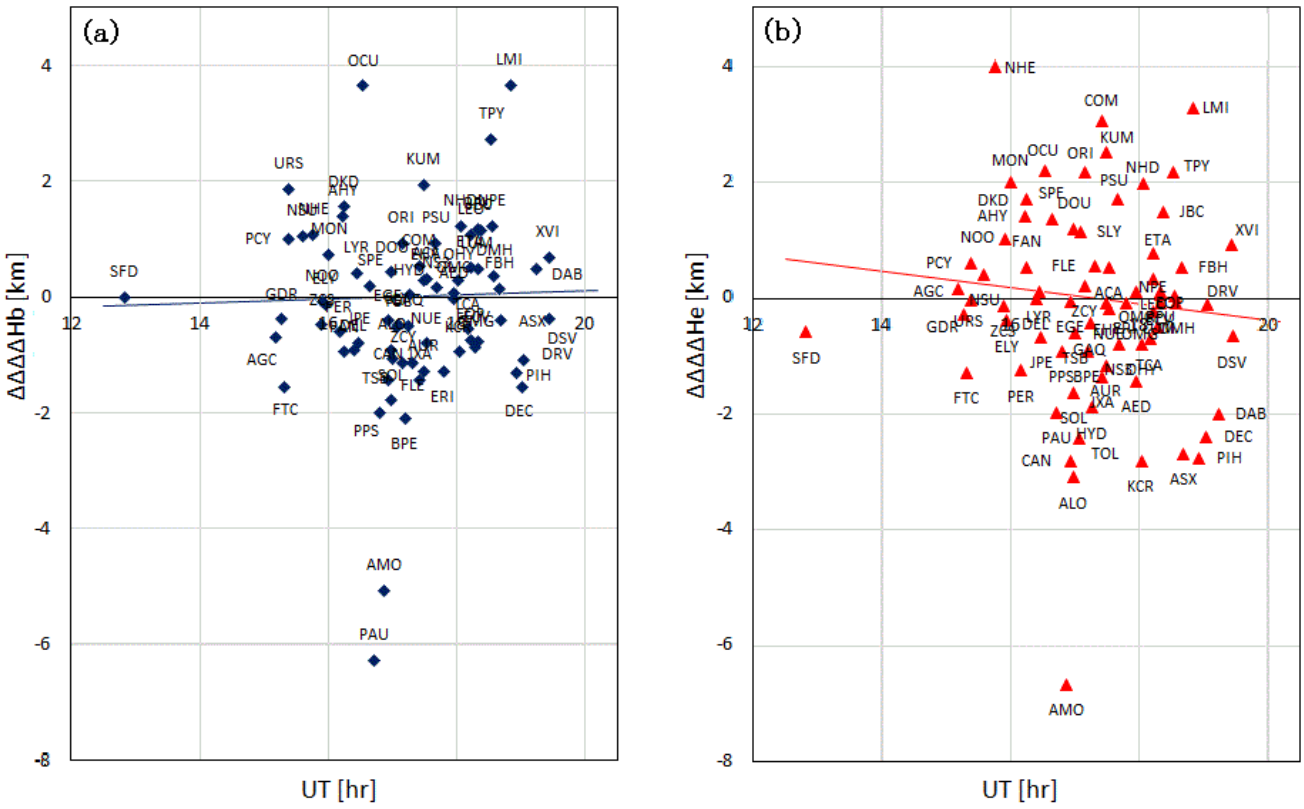

Figure 6 – $\Delta\Delta\Delta\Delta H_b$ and $\Delta\Delta\Delta\Delta H_e$ for Mean UT (UT=LT-9hr).

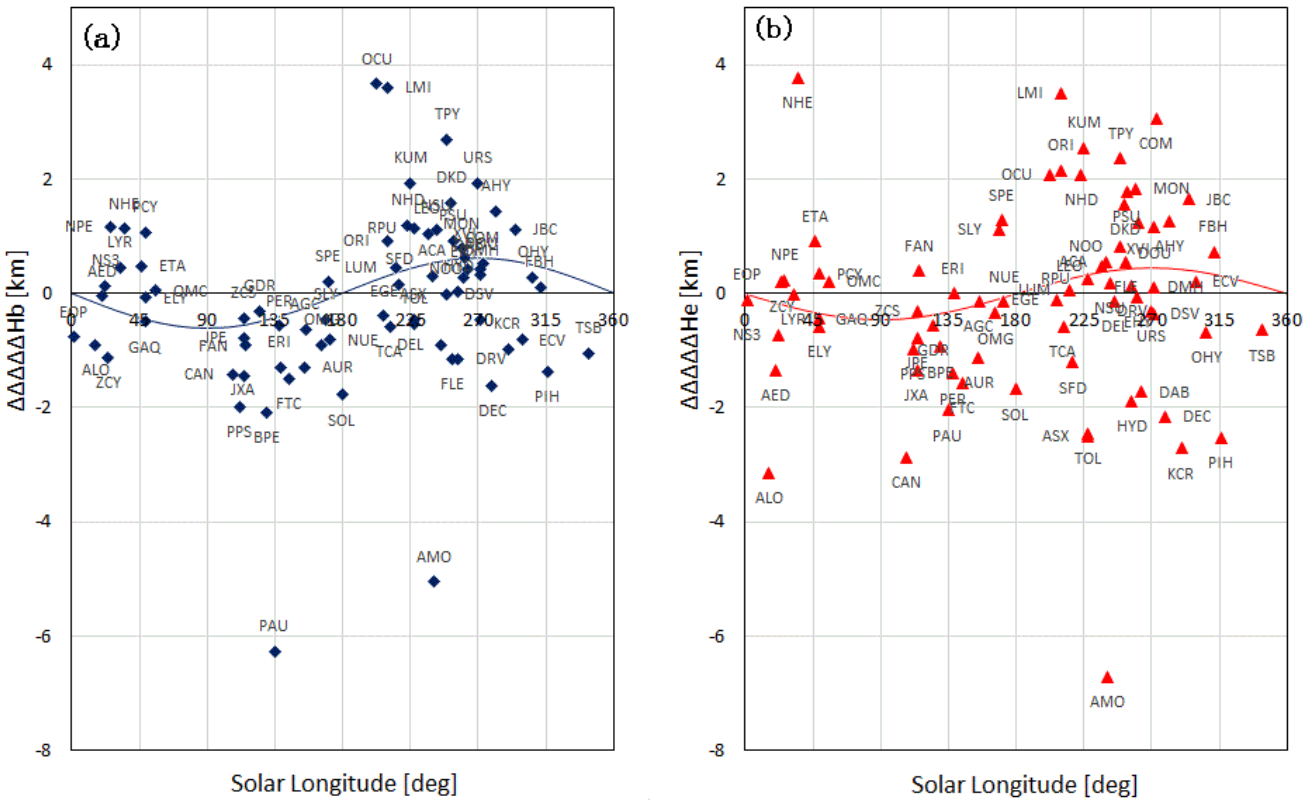

Figure 7 – $\Delta\Delta\Delta\Delta\Delta H_b$ and $\Delta\Delta\Delta\Delta\Delta H_e$ for the solar longitude.

criterion (Drummond, 1981) between the mean orbit for individual meteor showers and individual meteors' orbit belonging to that meteor shower was calculated (*av_Dd*). The Figure 9 vertical axis is the deviation between individual plot points and the sine curve fit in Figure 7. The Figure 9 horizontal axis is shown for the "*av_Dd*". In Figure 9, the right hand side indicates more diffused orbits from meteor showers that have evolved more since being released from the parent body. The results are similar to Figure 8.

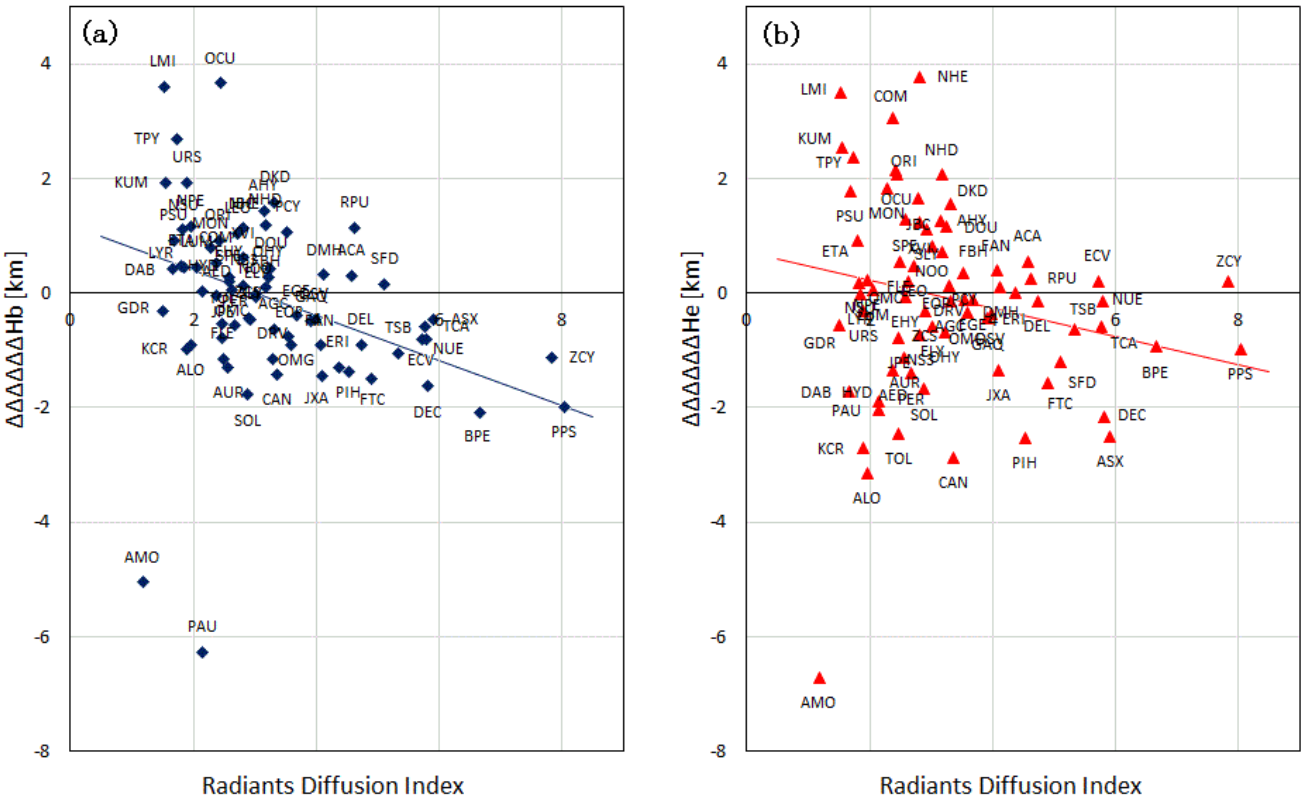

Figure 8 – $\Delta\Delta\Delta\Delta\Delta\Delta H_b$ and $\Delta\Delta\Delta\Delta\Delta\Delta H_e$ for the Radiants Diffusion Index.

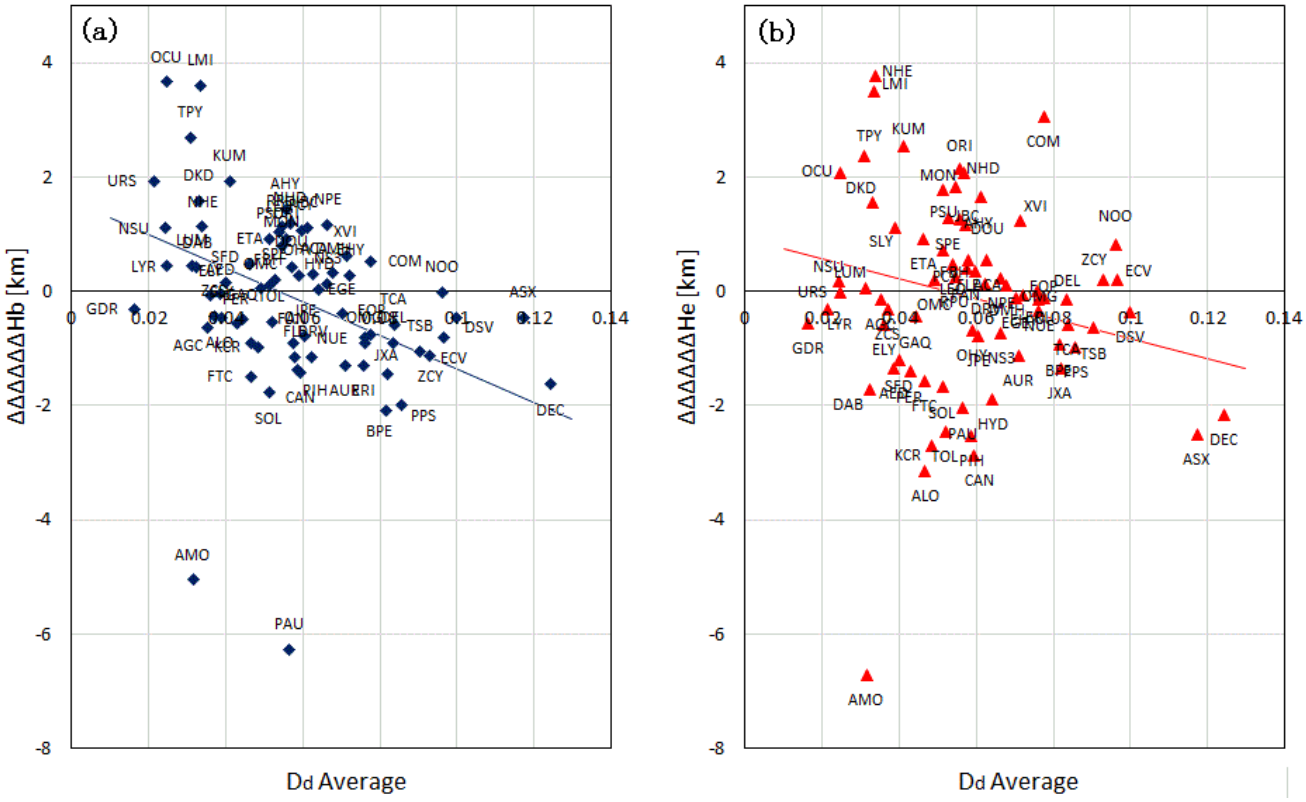

Figure 9 – $\Delta\Delta\Delta\Delta\Delta\Delta\Delta H_b$ and $\Delta\Delta\Delta\Delta\Delta\Delta\Delta H_e$ for the orbits difusion level.

3.9 The Inverse of the Semi-major Axis (1/a)

The Figure 10 vertical axis is the deviation between every plot point and the linear fit in Figure 8. The Figure 10 horizontal axis is shown for the inverse value of the semi-major axis. A small positive correlation is found for the start and end altitudes.

3.10 Inclination (i)

The Figure 11 vertical axis is the deviation between every plot point and the linear fit in Figure 8. The Fig-

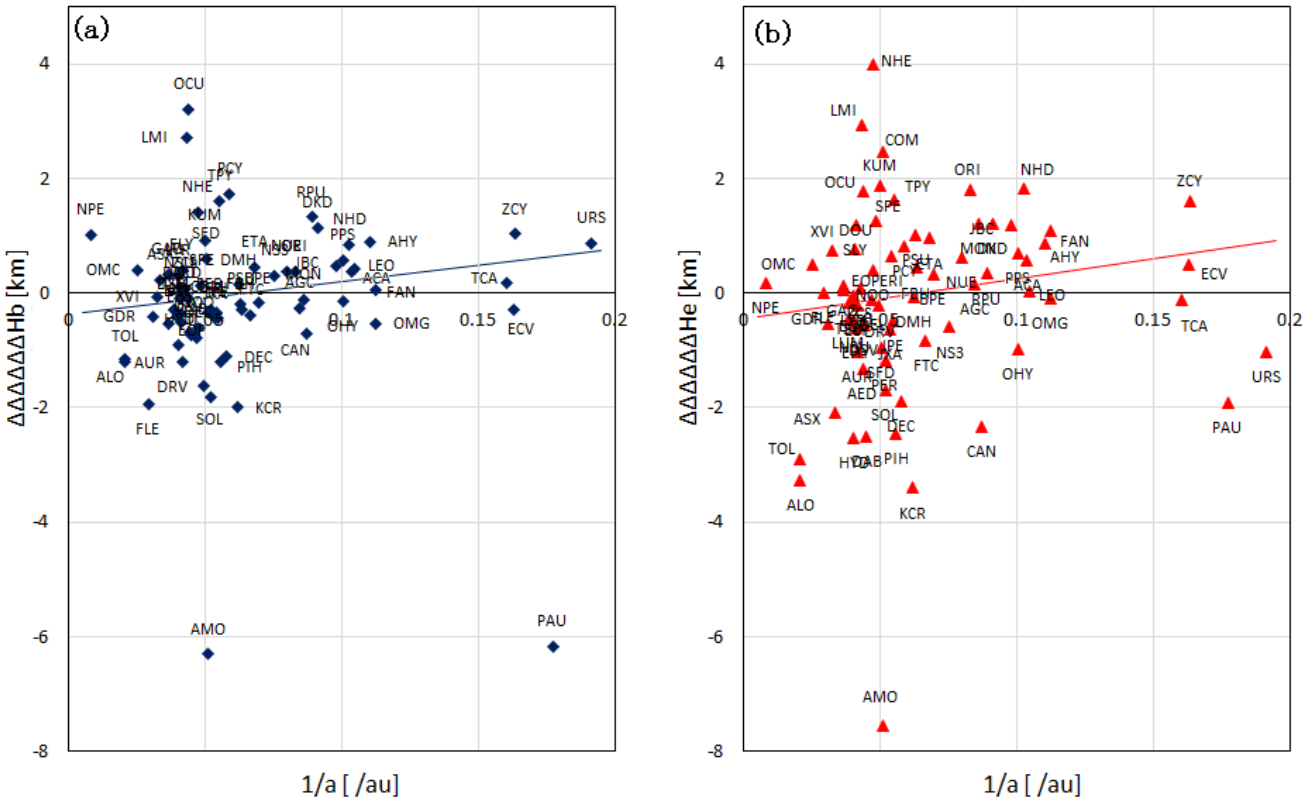

Figure 10 – $\Delta\Delta\Delta\Delta\Delta\Delta H_b$ and $\Delta\Delta\Delta\Delta\Delta\Delta H_e$ for the inverse of the orbit semi-major axis.

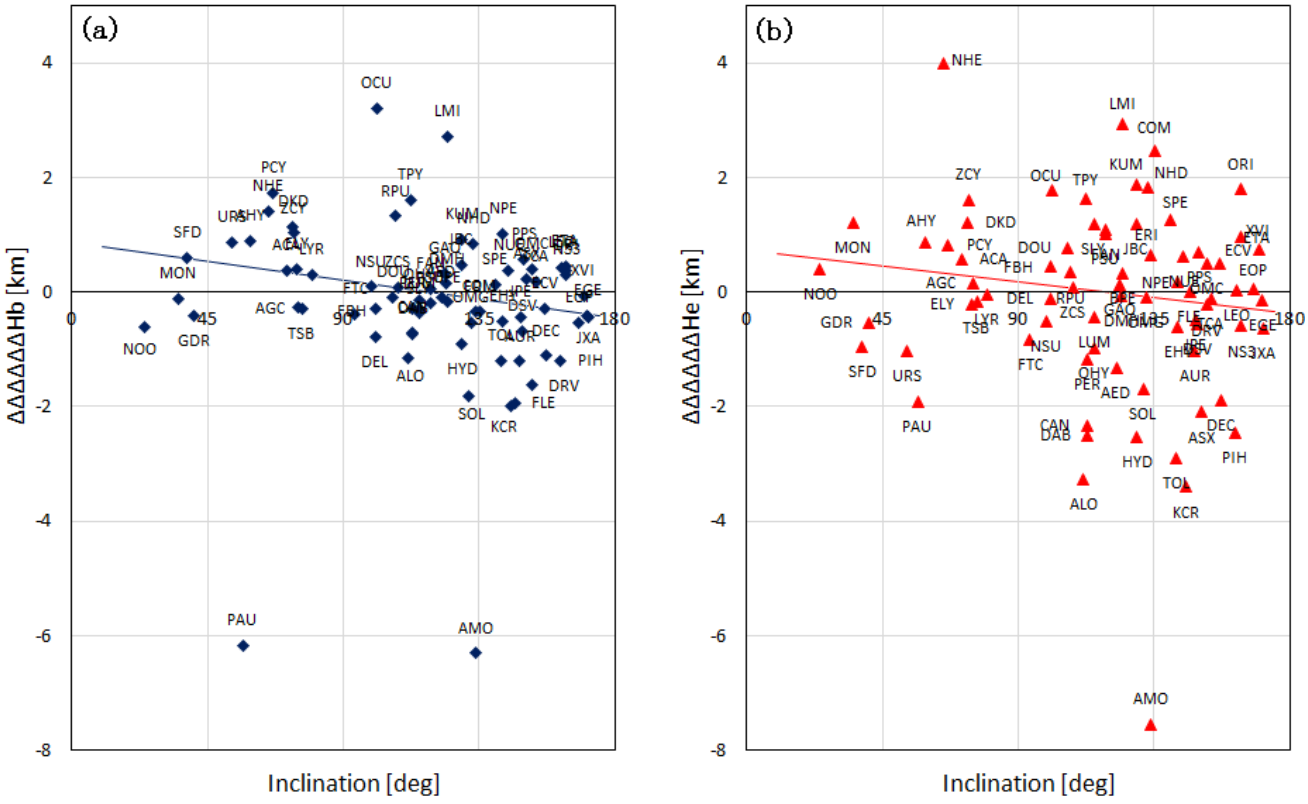

Figure 11 – $\Delta\Delta\Delta\Delta\Delta\Delta H_b$ and $\Delta\Delta\Delta\Delta\Delta\Delta H_e$ for the orbital inclination.

ure 11 horizontal axis is shown for the orbit inclination. The start and end altitudes have a weak negative correlation with the orbital inclination, and the retrograde orbit meteor shower start height is low.

3.11 Solar Cycle

Six meteor showers, that produced over 1 000 observed meteors over 15 years, were selected in order to investigate the correlation with the solar cycle. Figure 12 is the Wolf Number yearly rate published by The

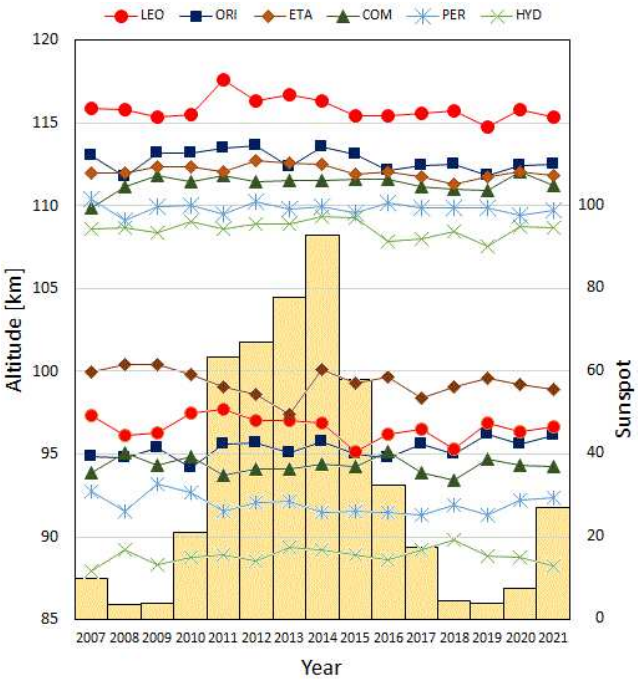

Figure 12 – Luminous height for the solar cycle (1).

Astronomical Society of Japan (NAOJ Mitaka, 2022) that was shown as a column graph and superposed each year meteor showers' luminous altitude is a polygonal line graph. The upper side is the start, and the lower side is the end. Correlation is difficult to interpret in Figure 12. Hence, Figure 13 was drawn with the Wolf number on the horizontal axis and altitudes on the vertical axis. Start altitudes are on the left end altitudes are on the right. If the Perseids are excluded, the meteor showers' linear fit increases left to right, indicating that meteor start heights are higher during the period of high solar activity. Only the Perseid linear fit was not right side up and showed low correlations (Table 2). The end altitudes linear fit slopes are random and no correlation exists.

Table 2 – Correlation coefficient of luminous height and solar activity.

shower	V_g [km/s]	begin	end
LEO	70.53	0.632	0.256
ORI	66.31	0.566	0.149
ETA	65.88	0.607	−0.395
COM	63.46	0.337	−0.143
PER	59.06	0.094	−0.272
HYD	59.07	0.574	0.193

4 Discussion

The many causes of individual meteor luminous altitude observation errors are considered. Under hazy skies or moonlight, the meteor's path will appear shortened. Images from observation sites distant from the meteor will not record the fainter parts of the meteor path in TV cameras due to distance effects and atmospheric absorption. If the start and the end are out of the field of view or hidden by clouds or buildings, the recorded positions will differ from the true start and end positions. SonotaCo network observers' camera systems are selected on individual observer decisions and are not uniform. More sensitive video cameras or larger aperture lenses can record the higher start and lower ending. Most small low light cameras have a tendency to record higher start points for fast meteors than do photographic observations because they have a higher sensitivity to the infrared range. In the meteor recording software UFOCapture some selectable values for sky conditions or observers' plans can be adjusted. For example, observers may want to record or not record extremely slow meteors or faint meteors close to the noise level. At the analysis stage, some values of UFOAnalyzer can be selected according to the preferences of individual observers. These affect the luminous height error. I believe that there was insensitivity to the fainter start of slow meteors by UFOAnalyzerV2 despite them being visible on the display device. Therefore, this problem was corrected in UFOAnalyzerV4.

I believe that the statistical research of meteor showers' luminous heights comparison can be sufficiently accurate, even though individual meteor errors might exist. This is because these errors exist almost equally for every meteor shower. Most of the SonotaCo Network observers operate the same types of equipment continue in long years not but specific equipment use to specific meteor showers. The total number of meteors in this study is 126 184 – which is enough to obscure statistical errors. Seasonable weather conditions influence the number of meteors recorded but not the luminous altitude. Finally, I adopted a threshold for 30 observed meteor orbit numbers for a meteor shower to reduce the statistical error.

I examined many influencing factors concerning meteors' luminous altitude in this study. It is explained in Section 1 that there have been many previous researches into factors affecting meteor luminous altitudes. The extent of the influence of factors was measured and taken away in Section 2 in the importance order that I estimated. Incidentally, it is a problem that it may not be clear as to which factor is the real influence factor regarding a meteor's luminous height when two or more factors influence each other. If after the first-factor influence's quantity has been taken out, the second-factor comes out as zero, this may not be reliable because the existing influence quantity may already have been taken out in the first phase. Generally, when there is a correlation between factors, the influence due to each factor affects the result for other factor and the exact root factors are difficult to decide. Hence, correlation coefficients between factors were listed in Table 3 and processed in the order given in Section 2. However, the bottom three factors were not processed in the same manner. Av_{Dd} was taken out from the influence as far as SL but not RDI. $1/a$ and i were taken out from the influence as far as RDI. A strong correlation is found between Vg and i in Table 3. Thus, using the wrong process for Vg can cause an unreliable correlation result for i. On the other hand q and RDI show

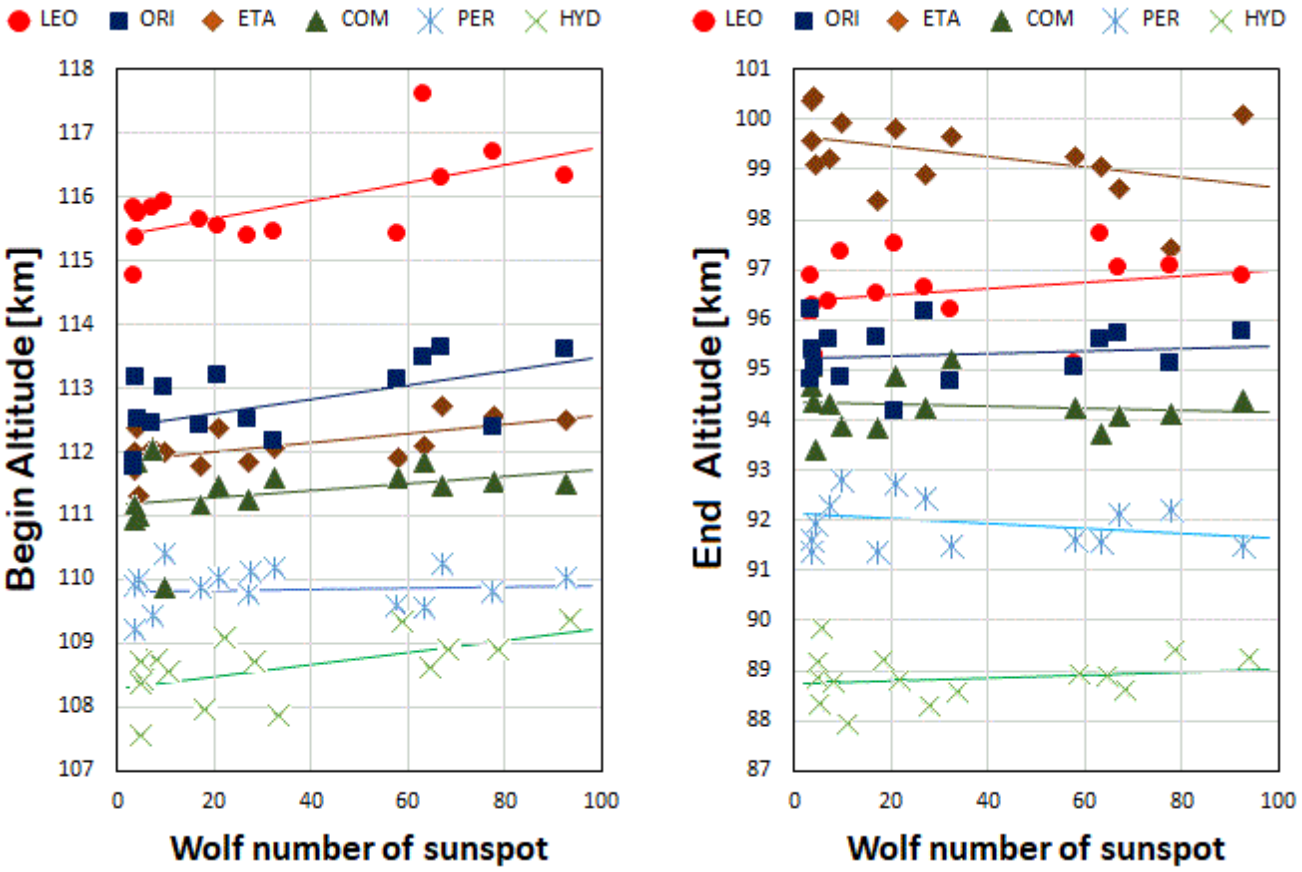

Figure 13 – Luminous height for the solar cycle (2).

Table 3 – Mutual correlation coefficients of the factors.

	Vg	ev	mag	q	UT	SL	RDI	Av_Dd	1/a	i
Vg		-0.30	**-0.48**	0.00	**0.74**	0.08	0.06	**0.40**	-0.15	**0.95**
ev	-0.30		-0.39	-0.09	**-0.50**	0.01	-0.12	-0.12	-0.23	-0.30
mag	**-0.48**	-0.39		-0.13	-0.12	0.03	0.23	0.07	**0.47**	**-0.44**
q	0.00	-0.09	-0.13		-0.10	-0.13	0.22	-0.25	0.14	0.02
UT	**0.74**	**-0.50**	-0.12	0.10		0.24	0.01	0.38	-0.04	**0.68**
SL	0.08	0.01	0.03	-0.13	0.24		0.00	0.17	0.16	-0.02
RDI	0.06	-0.12	0.23	0.22	0.01	0.00		**0.66**	0.39	0.06
Av_Dd	**0.40**	-0.12	0.07	-0.25	0.38	0.17	**0.66**		0.14	0.38
1/a	-0.15	-0.23	**0.47**	0.14	-0.04	0.16	0.39	0.14		-0.13
i	**0.95**	-0.30	**-0.44**	0.02	**0.68**	-0.02	0.06	0.38	-0.13	

few correlations to other processed factors and have few error sources. Only SL was not a linear approximation so can't have the same assessment.

The categorized correlation coefficients assessment was shown in Table 3 that of halftone background is for the |correlation coefficient| > 0.2, and bold for the |correlation coefficient| > 0.4.
$1 >$ |correlation coefficient| > 0.7 : strong correlation
$0.7 >$ |correlation coefficient| > 0.4 : moderate correlation
$0.4 >$ |correlation coefficient| > 0.2 : weak correlation
$0.2 >$ |correlation coefficient| $>$: little correlation

I assumed that the upper-side factor is more significant than the lower-side in Table 3, so I took away the influences from the upper-side to the lower-side, without the lower three factors, Dd, $1/a$, and i. If this assumption is incorrect, the results might be incorrect. It pays attention to that the correlation exists between "mag" and V_g which means that the "mag" results possibly include some error from the incorporation of V_g.

Based on the results, I now start to discuss the many complex influence factors affecting the luminous altitude of meteors.

The relation of geocentric velocity and luminous altitude of Halley-type and long-period meteor showers is a good approximation as linear (Figure 2). The previous research for sporadic meteors (Molau & Sonotaco, 2008) for slow velocity ($V_g < 25$ km/s) meteors presented disagreement with a linear approximation. The cause of both studies' disagreement is that low-velocity meteor showers are not contained in the Halley type and long-period meteor showers.

The start height of two meteor showers (#183 PAU, #246 AMO) is characteristically lower (Figures 2-10) than for other meteor showers. The meteoroid material for these meteor showers is possibly different from that of general meteors. The #246 AMO has a characteristic low ending altitude. The #246 AMO material might be lost volatile substances in the meteoroids or solidified high-density meteoroids. It might be categorized as "Ceplecha's Class A (small semi-major axis-asteroid origin)" (Cook, 1970). The previously photographed spectrum of two #246 AMO meteors of three was magnesium-rich (Sekiguchi, 2022). #246 AMO might have an unusual parent body or have experienced a unique orbital evolution. #183 PAU has a low altitude for only the start altitude. #183 PAU orbit has a small semi-major axis (Figure 10) resembling an asteroid and is close to the sun (Figure 5) that contain faint meteor (Figure 4). #187 PCA start altitude is low but the end altitude is contrarily ordinary for a meteor shower. These results were statistically uncertain because the total number of meteors number was low ($n = 15$). #319 JLE start and end are characteristics of low altitude but were removed from this study because the number of meteors was only a few ($n = 14$), even though the results agreed with previous research (Roggemans, 2017) based on CAMS data.

Two meteor showers (#22 LMI, #333 OCU) have a high start altitude. This feature agrees with (Roggemans, 2017) results. These meteor showers might be in the early stages of meteor shower evolution (Figures 8 and 9). The meteoroids are possibly covered with mechanically fragile material on the surface or are inclusive of a volatile substance. #581 NHE is a high-ending altitude meteor shower that would indicate a mechanically weak meteoroid construction. I expect future investigations for unique luminous altitude meteor showers' material characteristics.

Start height tends to be higher for low path elevation angles and this trend is more prominent for the end height (Figure 3). It agrees with previous research (Molau & Sonotaco, 2008). For low path elevation angles, collisions involve a more voluminous atmosphere mass in order to reach an equivalent altitude, therefore the start height may be higher by accumulated heat. End luminous altitudes for low elevation path angles also show rapid progress of ablation until an equivalent altitude is reached leading to a higher end-altitude trend. Hence, two model calculations were carried out and are shown compared with the observation in Figure 14 with 40 degrees elevation angle as the comparison origin. The first model assumes that the luminous trajectory length is constant for all elevation angles. The second model assumes that there is constant atmosphere mass collision with meteoroids for all elevation angles. In that case, the decrease by ablation of the meteoroids' cross-section area was neglected and a constant value was assumed. Figure 14 indicates that observational results are similar to results of the collision atmosphere mass constant model for the range of the low elevation path angles. On the other hand, for high path elevation angles, observation results were between both model results. I assumed collision meteoroids constant cross-section area in this because the decrease in cross-sectional area was difficult to model. It is future problem that collision cross section area be considered. A future challenge will be to create a model for the decrease in collision cross-section area.

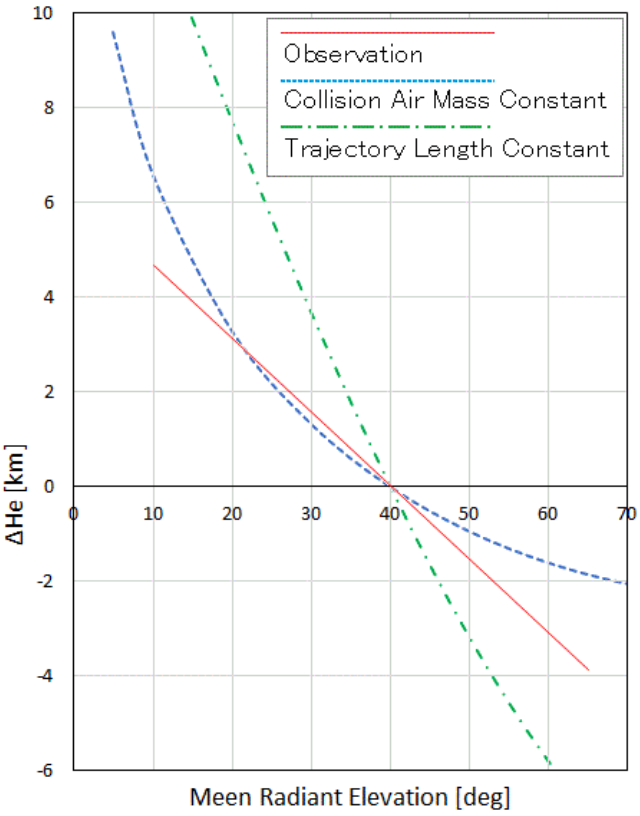

Figure 14 – Model calculations for the luminous end altitudes by the path elevation angle.

Bright meteor showers have a higher start and a lower end (Figure 4). It seems like a natural result. A different study (Ueda, 2015) has, however, shown that the start altitude of Geminid meteors is constant irrespective of the magnitude.

Short perihelion orbit meteor showers have a low start altitude (Figure 5). This result indicates some mechanism of metamorphism affects the meteoroids when close to the Sun. A suggested metamorphic mechanism follows: The solar wind will already have removed the meteoroids' surface fragile material, so there is less material left to peel off on collision with the Earth's atmosphere. The mechanically weak meteoroids, like dust-balls, will have been broken down and removed from their orbit. End altitude tends to be lower for meteor showers with short perihelion distances (Figure 5). This can be explained by volatile substances being re-

moved, density increases, and mechanically fragile meteoroids being removed from their orbit. Luminous altitude drastically increases near $q = 1$ (Figure 5) and it is likely that the snow-line in the solar system leads to differences in the dust material. Generally, it is possible for $q > 1$ meteoroids to include water (H_2O).

The end altitude decreases towards morning (Figure 6). However that is near the error level and it is difficult to separate the influences of the geocentric velocity and the radiant elevation angle. Optical observation struggles to detect all daily motion because it has a shorter observable time period than radio observation.

Seasonal motion (Figure 7) shows a similar result to (Clemesha & Batista, 2006) but does not agree with the (Roggemans, 2017; Figure 6) for sporadic meteor research. However, this result interpretation is complex because this study's result is near the error level, and furthermore (Clemesha & Batista, 2006) was based on southern hemisphere observations. I expect advanced future research will separate other factors that influence the luminous altitude.

Similar results were obtained by two different assessment methods for the meteor shower evolution level (Figures 8, 9). The luminous altitude of meteors decreases with the accumulation of completed orbits around the Sun, with the metamorphism of the meteoroids occurring when close to the Sun. This effect shows a smaller correlation than that for the perihelion distance but there may be a common mechanism involved. It might be better to use a curved approximation that converges to a constant value rather than a linear approximation.

Meteor showers with smaller orbits have slightly higher luminous altitudes (Figure 10). However, there is little correlation between the semi-major axis and the luminous altitude (Table 1). By the way, $1/a$ correlates with some factors that might influence it (Table 3). Future research is required.

A weak correlation exists between inclination and start altitude (Figure 11). The inclination does, however, influence some other factors (Table 3). The accurate determination of the relationship between inclination and luminous altitude is difficult in this study.

Five meteor showers show higher luminous altitudes during years of high solar activity (Figure 13). Only the Perseid meteor shower produced a negative result for the correlation between solar activity and the meteor luminous altitude. This result agrees with (Buček et al., 2012; Porubcan et al., 2012) based on photographic observations. The reason for the lack of correlation for the Perseids is considered complex. It is possible that the yearly mean Wolf number was not accurate for the Perseid season. The Perseid meteor shower's luminous magnitudes vary during its activity period. If observations during part of the Perseid period were hindered by cloudy skies, the result might be distorted. It is expected that future research is needed into the relationship between the Perseids and the solar cycle. This study's meteor shower geocentric velocity is 60 km/s or more. This meteor shower's start altitude was 107–118 km and includes extra high altitude start altitude ($H_b > 130$ km) meteors that might possibly be sensitive to solar activity. If we carry out future research for slower velocity meteor shower observations, we may possibly identify a relationship for atmospheric conditions in the lower thermosphere to the mesosphere with solar activity.

5 Conclusion

Research into some factors affecting the luminous start and end altitude statistics for Halley type and the long period meteor showers was carried out using SonotaCo network TV observation data. The height of the observation region involved covers the lower part of the thermosphere and the upper part of the mesosphere. Meteoroids' sizes were smaller than for photographic observations and larger than for radio observations. Almost all were fast meteors.

In addition, the factors listed below also correlate with luminous altitude:

(1) Path elevation angle,

(2) Mean luminous magnitude,

(3) perihelion distance,

(4) Meteor shower orbital evolution level.

It is concluded from correlations (3) and (4) that meteoroids undergo metamorphism when close to the Sun. That effect depends on the distance from the Sun and number of orbits and is more affected by the former.

A possible metamorphism mechanism consistent with the results is as follows:

(1) Some of the molecules are removed by vaporization.

(2) On meteoroid surfaces, mechanically weak materials are removed.

(3) The empty areas within the meteoroids vanish and thus the density increases hardening them.

(4) Mechanically weak meteoroids like "dust balls" disintegrate or are taken away from their meteor orbit.

A few unique meteor showers exist that do not agree with the general meteor shower's correlation. The meteoroid material of these meteor showers' may be unique and its origin or evolution may be different from that of ordinary meteor showers.

Five fast meteor showers showed higher luminous altitudes during the maximum solar activity period, but no such correlation exists for the Perseids. This result agrees with previous radio and photographic observation results. It is concluded that the air density is likely to be enhanced at the fast meteor luminous altitude layer during the period of maximum solar activity. I expect future research on the Perseids' unique characteristics.

Acknowledgements

This study is based on SonotaCo network data that is supported by software family developer Mr. SonotaCo and many amateur observers' efforts over the years. Dr. Koji Maeda granted worthful suggestions to me. Thank you very much for everyone's support. SonotaCo network observer Mr. Hideaki Muroishi, who was also a staff of "Mantenboshi" Yanagida village star observation museum, died in September 2022. I am very saddened by his death and pray that he may rest in peace.

References

Babadzhanov P. B. (2002). "Fragmentation and densities of meteoroids". *Astronomy and Astrophysics*, **384**, 317–321.

Batubara M., Yamamoto M. Y., Madkour W., and Manik T. (2018). "Long-Term Distribution of Meteors in a Solar Cycle Period Observed by VHF Meteor Radars at Near-Equatorial Latitudes". *Journal of Geophysical Research (Space Physics)*, **123:12**, 10,403–10,415.

Buček M., Porubčan V., and Zigo P. (2012). "Solar activity and Perseid meteor heights". *Contributions of the Astronomical Observatory Skalnate Pleso*, **42:1**, 22–32.

Campbell M. D., Brown P. G., Leblanc A. G., Hawkes R. L., Jones J., Worden S. P., and Correll R. R. (2000). "Image-intensified video results from the 1998 Leonid shower: I. Atmospheric trajectories and physical structure". *Meteoritics & Planetary Science*, **35:6**, 1259–1267.

Campbell-Brown M. D. (2019). "Solar cycle variation in radar meteor rates". *Monthly Notices of the Royal Astronomical Society*, **485:3**, 4446–4453.

Ceplecha Z. and Revelle D. O. (2005). "Fragmentation model of meteoroid motion, mass loss, and radiation in the atmosphere". *Meteoritics & Planetary Science*, **40:1**, 35–54.

Clemesha B. and Batista P. (2006). "The quantification of long-term atmospheric change via meteor ablation height measurements". *Journal of Atmospheric and Solar-Terrestrial Physics*, **68:17**, 1934–1939.

Cook A. F. (1970). "Discrete Levels of Beginning Height of Meteors in Streams". *SAO Special Report*, **324**.

Drummond J. D. (1981). "A test of comet and meteor shower associations". *Icarus*, **45:3**, 545–553.

Fujiwara Y., Ueda M., Shiba Y., Sugimoto M., Kinoshita M., Shimoda C., and Nakamura T. (1998). "Meteor luminosity at 160 km altitude from TV observations for bright Leonid meteors". *Geophysical Research Letters*, **25:3**, 285–288.

Japan Meteorological Agency (2022). `https://www.jma.go.jp/jma/indexe.html` .

Jenniskens P., Jopek T. J., Janches D., Hajduková M., Kokhirova G. I., and Rudawska R. (2020). "On removing showers from the IAU Working List of Meteor Showers". *Planetary and Space Science*, **182**, 104821.

Jopek T. J. and Jenniskens P. M. (2011). "The Working Group on Meteor Showers Nomenclature: A History, Current Status and a Call for Contributions". In Cooke W. J., Moser D. E., Hardin B. F., and Janches D., editors, *Meteoroids: The Smallest Solar System Bodies*. pages 7–13. NASA/CP-2011-216469.

Jopek T. J. and Kaňuchová Z. (2014). "Current status of the IAU MDC Meteor Showers Database". In Jopek T. J., Rietmeijer F. J. M., Watanabe J., and Williams I. P., editors, *Meteoroids 2013*. pages 353–364.

Jopek T. J. and Kaňuchová Z. (2017). "IAU Meteor Data Center-the shower database: A status report". *Planetary and Space Science*, **143**, 3–6.

Koten P., Spurný P., BorovičKa J., Evans S., Elliott A., Betlem H., Štork R., and Jobse K. (2006). "The beginning heights and light curves of high-altitude meteors". *Meteoritics & Planetary Science*, **41:9**, 1305–1320.

Lee W., Lee C., Kim J.-H., Kam H., and Kim Y. H. (2022). "A Modeling Analysis of the Apparent Linear Relation Between Mesospheric Temperatures and Meteor Height Distributions Measured by a Meteor Radar". *Journal of Geophysical Research (Space Physics)*, **127:1**, e29812.

Li G., Ning B., Wan W., Reid I. M., Hu L., Yue X., Younger J. P., and Dolman B. K. (2014). "Observational evidence of high-altitude meteor trail from radar interferometer". *Geophysical Research Letters*, **41:19**, 6583–6589.

Liu L., Liu H., Chen Y., Le H., Sun Y.-Y., Ning B., Hu L., and Wan W. (2017). "Variations of the meteor echo heights at Beijing and Mohe, China". *Journal of Geophysical Research (Space Physics)*, **122:1**, 1117–1127.

Molau S. and Sonotaco (2008). "On the average altitude of (video) meteors". *WGN, Journal of the International Meteor Organization*, **36:6**, 124–130.

NAOJ Mitaka (2022). "Solar science observatory". `https://solarwww.mtk.nao.ac.jp/jp/activity/activity_backnumber.html` .

Neslusan L., Porubcan V., Svoren J., and Jakubik M. (2020). "On the new design of the IAU MDC portal". *WGN, Journal of the International Meteor Organization*, **48:6**, 168–169.

Porubcan V., Bucek M., Cevolani G., and Zigo P. (2012). "Variation of Meteor Heights and Solar-Cycle Activity". *Publ. Astron. Soc. Japan*, **64**, 86.

Premkumar B., Reddy K. C., and Yellaiah G. (2018). "Variation of the meteor count rate and echo height during solar cycle 23 and 24". *IAU Symposium*, **340**, 73–74.

Roggemans P. (2017). "Variation in heights of CAMS meteor trajectories". *eMeteorNews*, **2:3**, 80–86.

Sarma T. and Jones J. (1985). "Double-station observations of 454 TV meteors. I - Trajectories". *Bulletin of the Astronomical Institutes of Czechoslovakia*, **36**, 9–24.

Sekiguchi T. (2022). "Halley-type & long-period meteor shower characteristics". `http://sonotaco.jp/forum/viewtopic.php?t=5264` . (in Japanese).

SonotaCo (2009). "A meteor shower catalog based on video observations in 2007-2008". *WGN, Journal of the International Meteor Organization*, **37:2**, 55–62.

Spurný P., Betlem H., van't Leven J., and Jenniskens P. (2000). "Atmospheric behavior and extreme beginning heights of the 13 brightest photographic Leonids from the ground-based expedition to China". *Meteoritics & Planetary Science*, **35:2**, 243–249.

Spurný P., Shrbený L., Borovička J., Koten P., Vojáček V., and Štork R. (2014). "Bright Perseid fireball with exceptional beginning height of 170 km observed by different techniques". *Astronomy & Astrophysics*, **563**, A64.

Ueda M. (2015). "2014 Geminids the relation of magnitude and height".

Vinković D. (2007). "Thermalization of sputtered particles as the source of diffuse radiation from high altitude meteors". *Advances in Space Research*, **39:4**, 574–582.

Ward B. (2016). "Melting meteors". `http://sonotaco.jp/forum/viewtopic.php?t=3630` .

Handling Editors: Javor Kac and Tracie Heywood

Appendix

All meteor showers data in this study are shown in Table A.1.

Table A.1 – Halley-type and long-period meteor showers in this study. All orbital elements and coordinates are given for J2000.

No.	Meteor Shower Name	Code	Activity	S. Lon [°]	S.Lon Beg [°]	S.Lon End [°]	RA [°]	DE [°]	dRA [°]	dDE [°]	Vg [km/s]	dVg [km/s]	a [au]	q [au]	e	P [yr]	Peri [°]	Node [°]	Incl [°]	N	H1 [km]	H2 [km]	Ev [°]	mag	RDI	Av_Dd	Av_UT [hr]
6	April Lyrids	LYR	annual	32.18	29	35	272.2	33.4	0.78	−0.21	46.8	0.17	25.1	0.921	0.963	125.4	214.0	32.2	79.7	601	106.4	86.5	59.0	−1.9	1.84	0.025	16.44
7	Perseids	PER	annual	138.06	119	152	45.5	57.5	1.45	0.21	59.1	0.04	19.3	0.949	0.951	85.1	150.6	138.1	112.9	8862	109.9	92.0	42.6	−2.0	2.67	0.043	16.17
8	Orionids	ORI	annual	210.17	198	226	97.0	15.7	0.80	0.03	66.3	−0.06	12.1	0.572	0.953	41.9	82.7	30.2	164.0	3909	112.8	95.3	52.1	−1.8	2.41	0.056	17.15
13	Leonids	LEO	annual	236.57	217	259	154.6	21.4	0.64	−0.40	70.5	0.03	9.57	0.983	0.897	29.6	173.5	236.6	162.4	1507	115.8	96.7	47.3	−2.2	2.73	0.054	18.22
15	Ursids	URS	annual	269.74	266	272	217.4	75.7	1.62	−0.33	33.4	−0.12	5.22	0.937	0.820	11.9	206.5	269.7	53.2	281	102.4	87.0	32.9	−0.8	1.89	0.021	15.39
16	sigma Hydrids	HYD	annual	256.71	237	280	125.8	2.3	0.85	−0.27	59.1	−0.04	24.9	0.258	0.990	124.2	119.0	76.7	129.2	1898	108.6	88.8	46.1	−1.5	2.15	0.064	17.27
19	Dec. Monocerotids	MON	annual	258.99	247	269	101.0	8.1	0.67	−0.13	41.4	−0.18	11.6	0.189	0.984	39.7	129.1	79.0	35.3	606	103.1	85.8	49.1	−1.5	2.28	0.054	16.00
20	Comae Berenicids	COM	annual	273.15	248	324	165.8	28.4	0.87	−0.43	63.5	0.00	19.7	0.558	0.972	87.3	263.1	273.2	135.1	1259	111.4	94.3	57.0	−1.8	2.37	0.077	17.42
22	Leonis Minorids	LMI	annual	209.98	204	216	160.9	36.6	1.10	−0.33	61.6	−0.05	23.3	0.623	0.973	112.6	104.0	210.0	124.8	162	114.2	97.5	36.3	−1.8	1.52	0.034	18.83
23	epsilon Geminids	EGE	annual	207.05	196	218	102.9	27.7	0.83	−0.14	69.4	−0.03	25.2	0.784	0.969	126.5	235.1	207.1	171.0	136	113.4	94.5	52.2	−2.1	3.67	0.070	16.93
27	kappa Serpentids	KSE	annual	24.57	21	27	247.0	18.2	0.74	−0.14	46.4	−0.10	25.5	0.534	0.979	129.1	266.8	24.6	74.4	21	105.5	86.6	54.6	−1.6	2.67	0.043	15.91
31	eta Aquariids	ETA	annual	46.55	38	63	338.5	−0.6	0.68	0.34	65.9	0.04	14.8	0.588	0.960	56.9	98.4	46.5	163.6	1519	112.1	99.0	22.0	−1.4	1.81	0.046	18.21
40	zeta Cygnids	ZCY	annual	23.98	3	45	306.3	42.3	0.94	0.21	43.0	0.00	6.12	0.893	0.854	15.1	140.4	24.0	73.4	145	102.1	90.0	38.7	−0.4	7.83	0.093	17.16
81	Sep. Lyncids	SLY	annual	169.05	164	175	111.4	55.7	1.69	0.01	59.4	−0.13	24.4	0.754	0.969	120.2	119.4	169.1	115.1	48	109.3	95.9	32.4	−1.5	2.93	0.039	17.08
89	Jan. pi Virginids	PVI	annual	290.20	285	296	177.3	11.0	1.02	−0.31	66.3	0.01	41.1	0.493	0.988	263.4	270.2	290.2	159.7	18	109.3	95.7	43.5	−0.9	3.18	0.048	16.90
101	pi Hydrids	PIH	annual	315.91	303	328	211.2	−23.5	0.98	−0.38	70.6	−0.01	18.0	0.922	0.949	76.1	29.4	135.9	161.9	72	112.7	97.4	26.8	−1.6	4.52	0.059	18.93
145	eta Lyrids	ELY	annual	49.33	46	54	290.8	43.5	0.33	0.14	44.2	−0.02	24.2	1.000	0.959	118.8	190.8	49.3	74.7	100	104.7	86.6	54.2	−1.4	3.03	0.036	15.95
175	Jul. Pegasids	JPE	annual	114.40	104	128	352.7	12.6	0.84	0.30	64.0	−0.06	18.4	0.562	0.969	78.6	264.8	114.4	148.8	113	110.5	91.7	49.8	−2.0	2.47	0.061	16.48
183	Piscis Austrinids	PAU	annual	134.77	129	140	352.6	−20.9	0.88	0.32	44.3	−0.03	5.64	0.129	0.977	13.4	140.1	314.8	56.7	33	96.2	86.6	29.8	−0.7	2.15	0.057	16.72
184	Jul. gamma Draconids	GDR	annual	125.17	123	127	280.6	50.7	−0.19	−0.04	27.7	−0.15	32.4	0.977	0.970	184.8	202.6	125.2	40.6	47	98.4	80.5	58.4	−1.2	1.50	0.016	15.27
187	psi Cassiopeiids	PCA	annual	115.87	108	122	356.2	71.1	1.57	0.28	44.6	0.18	14.3	0.976	0.932	53.9	156.8	115.9	76.5	15	101.9	86.7	42.1	−1.7	4.16	0.046	14.67
190	beta Perseids	BPE	annual	129.67	117	143	54.1	48.0	1.42	0.17	60.9	0.03	14.4	0.726	0.950	54.7	114.7	129.7	124.7	83	108.0	93.2	40.0	−1.4	6.65	0.082	17.20
191	eta Eridanids	ERI	annual	138.57	114	158	45.2	−10.8	0.90	0.39	64.8	0.04	18.5	0.954	0.948	79.5	27.9	318.6	134.0	351	110.9	97.8	28.9	−1.6	4.37	0.076	17.80
206	Aurigids	AUR	annual	154.87	135	171	87.1	38.8	1.13	0.12	65.6	0.02	24.2	0.665	0.972	118.8	107.9	154.9	148.4	107	110.6	94.7	35.6	−1.7	2.56	0.071	17.49
208	Sep. epsilon Perseids	SPE	annual	170.36	163	198	51.7	39.5	1.19	0.05	64.6	0.03	20.7	0.714	0.965	94.0	245.9	170.4	140.4	299	112.4	92.7	58.6	−2.4	2.57	0.053	16.65
246	alpha Monocerotids	AMO	annual	240.93	237	247	118.5	0.7	0.98	−0.15	62.1	0.02	19.6	0.472	0.976	87.0	93.3	60.9	134.0	40	105.5	85.8	43.4	−2.0	1.18	0.031	16.88
250	Nov. Orionids	NOO	annual	248.69	232	267	91.8	15.2	0.75	−0.05	42.7	−0.15	21.2	0.124	0.994	97.6	139.2	68.7	24.1	480	102.0	85.2	51.7	−1.0	3.00	0.096	15.91
252	alpha Lyncids	ALY	Could not confirm its existence.																								
281	Oct. Camelopardalids	OCT	Too few meteor numbers to statistics.																								
319	Jan. Leonids	JLE	annual	282.24	281	284	147.8	23.7	0.69	−0.16	52.7	−0.12	7.41	0.051	0.993	20.2	334.6	282.2	106.8	14	97.6	84.9	48.6	−0.8	1.77	0.044	16.25
320	omega Serpentids	OSE	Could not confirm its existence.																								
331	alpha Hydrids	AHY	annual	282.17	273	294	126.0	−8.1	0.67	−0.16	43.8	−0.08	9.06	0.288	0.968	27.3	116.0	102.2	59.3	191	104.0	89.3	36.4	−0.7	3.14	0.056	16.22
333	Oct. Ursae Majorids	OCU	annual	202.61	201.1	204.6	145.6	64.1	1.14	−0.94	55.8	0.28	22.8	0.979	0.957	108.9	164.5	202.6	101.1	70	112.9	96.2	32.5	−1.8	2.43	0.025	16.54
335	Dec. chi Virginids	XVI	annual	261.32	248	275	190.3	−9.9	0.68	−0.36	68.5	0.07	30.8	0.622	0.980	171.1	284.9	81.3	169.6	129	113.2	98.8	30.9	−1.4	2.81	0.071	19.43
336	Dec. kappa Draconids	DKD	annual	251.92	247	258	185.9	70.4	0.72	−0.46	43.8	0.06	11.0	0.925	0.916	36.4	209.3	251.9	73.1	171	106.1	91.4	35.9	−1.3	3.32	0.033	16.24
337	nu Eridanids	NUE	annual	171.66	160	187	71.0	2.3	0.78	0.35	66.5	0.06	12.5	0.891	0.929	44.4	40.0	351.7	144.8	139	111.7	96.3	40.4	−1.6	5.79	0.076	17.53
339	psi Ursae Majorids	PSU	annual	253.53	241	270	169.8	42.7	0.91	−0.64	61.9	0.15	16.8	0.919	0.945	68.9	210.4	253.5	118.9	84	111.6	95.4	49.6	−1.4	1.68	0.051	17.67
340	theta Pyxidids	TPY	annual	249.51	247	252	138.6	−25.7	1.31	−0.13	60.0	0.23	18.1	0.956	0.947	77.0	20.2	69.5	112.3	49	112.8	99.4	25.3	−1.2	1.72	0.031	18.53
362	Jun. mu Cassiopeiids	JMC	annual	74.13	71	75	9.9	55.5	1.19	0.72	42.7	−0.29	8.14	0.646	0.921	23.2	104.0	74.1	69.7	15	101.7	88.0	34.9	−0.8	4.13	0.052	17.19
372	phi Piscids	PPS	annual	111.47	76	138	24.5	27.9	0.79	0.42	66.8	0.00	10.0	0.909	0.909	31.4	142.7	111.5	149.8	358	110.6	96.3	37.0	−1.6	8.03	0.086	16.80
394	alpha Canis Majorids	ACA	annual	239.50	230	250	95.6	−19.9	0.67	0.15	44.4	−0.01	9.63	0.585	0.939	29.9	80.9	59.5	71.1	52	103.8	90.8	29.1	−0.7	4.57	0.063	17.53
410	delta Piscids	DPI	annual	93.52	90	97	12.5	5.4	0.93	0.19	69.6	−0.13	16.1	0.919	0.943	64.9	144.0	93.5	179.9	9	110.9	99.0	24.0	−0.7	3.44	0.050	17.16
411	c Andromedids	CAN	annual	107.18	93	118	29.5	47.3	1.20	0.35	57.4	−0.01	11.5	0.691	0.940	38.9	109.8	107.2	113.0	106	106.9	90.6	38.7	−1.0	3.36	0.059	16.94
424	Sep.-Oct. Lyncids	SOL	annual	179.59	170	190	107.9	49.8	1.44	−0.11	64.5	−0.03	19.3	0.906	0.953	84.8	143.3	179.6	131.4	36	110.3	94.5	37.4	−1.7	2.88	0.051	16.98
425	psi Aurigids	PSA	annual	199.42	186	213	119.1	42.8	1.28	−0.29	67.2	0.04	9.90	0.991	0.900	31.1	171.0	199.4	142.2	28	110.7	94.5	47.9	−1.5	2.91	0.054	17.69
427	Feb. eta Draconids	FED	annual	314.55	314	315.5	240.3	62.1	−0.73	−0.36	34.8	0.36	15.9	0.971	0.939	63.1	193.9	314.5	54.7	9	104.4	89.3	49.4	−1.4	1.87	0.032	18.65
428	Dec. sigma Virginids	DSV	annual	271.14	245	299	208.1	4.5	0.82	−0.21	66.5	0.01	22.7	0.617	0.973	107.9	104.1	271.1	149.4	309	111.5	95.5	36.3	−1.5	3.98	0.100	19.45
429	alpha Coronae Borealids	ACB	annual	308.87	307	312	232.5	26.8	1.55	−0.65	58.3	0.06	39.9	0.982	0.975	252.3	175.4	308.9	106.0	16	112.3	94.8	46.9	−1.7	2.30	0.026	18.41
431	Jun. iota Pegasids	JIP	annual	93.73	93.4	95.1	331.5	29.2	1.02	0.03	59.1	0.33	180	0.903	0.995	2408	219.1	93.7	112.7	13	112.2	89.4	48.6	−2.7	0.78	0.020	15.39
432	nu Bootids	NBO	Could not confirm its existence.																								
439	alpha Sextantids	ASX	annual	227.39	200	250	146.3	−3.9	0.77	−0.21	68.9	0.06	29.9	0.876	0.971	163.3	320.7	47.4	150.8	158	113.0	95.4	34.6	−1.6	5.90	0.117	18.69
440	Nov. Leonis Minorids	NLM	Could not confirm its existence.																								
444	zeta Cassiopeiids	ZCS	annual	114.29	106	119	9.1	51.1	1.71	0.30	57.5	0.08	23.5	0.992	0.958	113.8	162.3	114.3	108.1	133	109.1	92.6	46.7	−1.5	2.89	0.037	15.89
445	kappa Ursae Majorids	KUM	annual	225.12	221	235	146.9	44.9	1.25	−0.25	65.1	−0.04	20.1	0.987	0.951	89.9	186.9	225.1	129.4	116	114.9	97.3	45.1	−2.3	1.56	0.041	17.48
450	April epsilon Delphinids	AED	annual	20.08	14	30	307.8	11.5	0.93	0.35	61.0	−0.06	23.0	0.723	0.969	110.2	115.8	20.1	122.5	43	110.7	94.0	29.1	−1.9	2.38	0.039	17.96
458	Jun. epsilon Cygnids	JEC	annual	82.51	81.8	83.5	315.1	33.6	1.98	0.29	53.3	0.42	104	0.922	0.991	1067	215.4	82.5	95.9	13	108.7	92.7	53.0	−1.7	1.14	0.017	15.35
465	August xi Cassiopeiids	AXC	annual	134.03	131	137	4.0	49.3	0.86	0.36	56.0	0.05	13.9	0.927	0.933	51.7	214.5	134.0	105.0	29	108.7	92.1	54.5	−1.9	2.65	0.042	15.23
480	tau Cancrids	TCA	annual	211.48	196	223	141.5	30.0	0.97	0.03	67.7	−0.01	6.22	0.861	0.862	15.5	135.6	211.5	153.8	128	112.0	96.0	42.2	−1.4	5.77	0.084	18.17
488	Nov. sigma Ursae Majorids	NSU	annual	242.41	239.6	245.1	149.6	59.2	1.10	−0.28	55.0	−0.07	23.6	0.816	0.965	114.5	229.7	242.4	99.3	30	109.2	93.2	38.4	−1.3	1.82	0.024	15.60
493	Dec. epsilon Craterids	DEC	annual	279.20	260	315	186.4	−17.0	0.82	−0.32	70.6	0.02	17.4	0.968	0.944	72.6	349.0	99.2	157.1	205	112.5	97.4	30.4	−1.5	5.81	0.124	19.03
494	Dec. Lyncids	DEL	annual	245.53	231	260	125.8	51.3	0.92	−0.15	54.5	−0.13	21.4	0.462	0.978	98.7	274.4	245.5	100.7	58	106.3	88.5	55.1	−1.4	4.73	0.084	16.40
497	Dec. alpha Bootids	DAB	annual	263.49	261.7	267	212.5	22.2	0.94	−0.31	59.3	0.05	22.4	0.680	0.970	105.7	111.8	263.5	113.0	34	110.2	91.8	35.4	−1.7	1.66	0.032	19.23

Table A.1 – Halley-type and long-period meteor showers in this study. All orbital elements and coordinates are given for J2000 – continued from previous page.

No.	Meteor Shower Name	Code	Activity	S. Lon	S.Lon Beg	S.Lon End	RA	DE	dRA	dDE	Vg	dVg	a	q	e	P	Peri	Node	Incl	N	H1	H2	Ev	mag	RDI	Av_Dd	Av_UT
				[°]	[°]	[°]	[°]	[°]	[°]	[°]	[km/s]	[km/s]	[au]	[au]		[yr]	[°]	[°]	[°]		[km]	[km]	[°]					[hr]
498	Dec. mu Hydrids	DMH	annual	271.78	261	288	159.0	−26.0	0.98	−0.22	63.6	0.09	16.1	0.929	0.942	64.5	27.5	91.8	124.2	117	112.0	98.1	24.0	−1.5	4.12	0.068	18.58
502	Dec. rho Virginids	DRV	annual	256.66	246	269	188.4	12.5	0.91	−0.15	68.6	−0.04	20.2	0.798	0.960	90.8	127.8	256.7	152.4	85	112.1	96.3	41.3	−1.8	3.28	0.062	19.05
510	Jun. rho Cygnids	JRC	annual	84.94	83.4	85.3	321.4	44.3	0.70	0.36	50.1	−0.03	18.1	1.006	0.944	76.7	191.2	84.9	88.9	17	106.0	89.7	48.7	−1.5	2.47	0.024	14.94
512	rho Puppids	RPU	annual	228.02	219	237	127.1	−25.5	1.19	−0.18	58.0	0.09	11.2	0.987	0.912	37.7	0.9	48.0	107.4	61	110.7	97.0	23.6	−1.2	4.62	0.054	18.34
514	omega Capricornids	OMC	annual	55.20	46	63	304.3	−32.7	1.12	0.30	65.2	−0.02	39.9	0.565	0.986	251.6	83.6	235.2	152.4	32	110.7	99.4	18.1	−0.7	2.63	0.049	17.94
517	Apr. lambda Ophiuchids	ALO	annual	15.45	12	21	244.6	1.1	1.00	−0.08	56.4	0.03	48.7	0.295	0.994	340.3	294.6	15.4	111.7	33	107.0	86.7	45.7	−1.7	1.95	0.047	16.98
520	May beta Capricornids	MBC	annual	55.32	49	62	302.5	−15.5	0.76	0.09	66.7	0.01	25.2	0.586	0.977	126.2	261.4	55.3	170.6	17	109.8	97.4	28.6	−1.6	1.93	0.043	17.15
523	Aug. gamma Cepheids	AGC	annual	155.30	149	161	356.1	76.8	1.13	0.38	44.0	0.14	11.7	1.005	0.914	39.9	187.6	155.3	75.2	47	104.0	88.7	45.1	−1.3	3.31	0.035	15.18
524	lambda Ursae Majorids	LUM	annual	215.45	212.4	218.3	158.7	49.2	0.93	−0.41	60.7	0.06	26.1	0.918	0.965	133.6	147.8	215.4	115.2	30	111.2	94.4	39.8	−1.7	2.06	0.031	18.32
529	eta Hydrids	EHY	annual	260.42	245	276	135.8	1.4	0.84	−0.21	62.7	−0.03	24.4	0.377	0.985	120.5	104.2	80.4	142.8	227	110.1	92.5	45.8	−1.4	2.58	0.072	17.50
530	eta Corvids	ECV	annual	299.28	280	319	189.2	−17.4	0.84	−0.11	68.2	−0.02	6.13	0.818	0.867	15.2	50.0	119.3	157.0	156	111.9	98.7	30.4	−1.3	5.72	0.097	18.32
531	gamma Aquilids	GAQ	annual	48.66	40	58	304.9	14.4	0.97	0.24	62.8	−0.03	27.5	0.985	0.964	144.5	197.7	48.7	123.7	40	111.3	93.6	46.6	−2.0	3.91	0.044	17.24
533	Jul. xi Arietids	JXA	annual	114.37	94	130	36.7	9.3	0.73	0.23	69.0	0.04	18.6	0.866	0.953	80.4	314.8	294.4	171.3	70	112.0	97.9	27.9	−1.6	4.10	0.082	17.43
545	xi Cassiopeiids	XCA	annual	155.86	154	159	9.5	50.6	1.19	0.31	52.7	0.32	31.2	0.728	0.977	174.3	244.2	155.9	95.5	12	106.1	88.6	63.3	−1.4	2.39	0.033	15.85
546	43 Cassiopeiids	FTC	annual	144.13	140	148	28.2	68.5	1.74	0.44	52.2	0.07	15.1	1.007	0.933	58.4	173.7	144.1	93.8	41	106.0	90.1	44.7	−1.3	4.89	0.046	15.32
549	49 Andromedids	FAN	annual	115.51	103	123	24.9	46.8	1.13	0.25	59.9	0.05	8.89	0.891	0.900	26.5	137.9	115.5	119.1	63	109.1	94.9	40.6	−1.4	4.07	0.057	16.25
557	64 Draconids	SFD	annual	217.69	208	227	300.8	65.5	−0.17	−0.15	26.2	−0.15	19.9	0.975	0.951	88.7	195.2	217.7	38.1	58	98.4	82.1	43.3	−1.1	5.11	0.040	12.83
558	27 Monocerotids	TSM	annual	223.14	213	235	119.7	−6.7	0.91	−0.07	65.0	0.06	9.75	0.925	0.905	30.4	30.6	43.1	133.1	47	113.1	98.6	37.9	−1.4	3.17	0.057	18.06
563	Dec. omega Ursae Majorids	DOU	annual	271.91	262	283	162.7	42.2	1.30	−0.29	56.7	0.00	24.8	0.543	0.978	123.4	264.7	271.9	106.5	85	108.9	90.1	56.8	−1.7	3.24	0.057	16.98
566	5-Comae Berenicids	BCF	annual	274.84	270	279	178.2	20.7	1.08	−0.40	67.4	0.10	11.1	0.818	0.926	36.9	229.4	274.8	146.2	20	109.6	93.6	48.2	−1.3	2.58	0.037	17.49
569	omicron Hydrids	OHY	annual	306.46	293	316	174.6	−32.9	0.81	−0.36	59.3	−0.06	10.0	0.683	0.931	31.4	68.7	126.5	115.0	97	109.0	97.0	18.5	−0.5	3.22	0.059	18.03
570	Feb. beta Herculids	FBH	annual	311.32	301	318	246.5	23.9	0.93	−0.06	55.7	−0.12	15.9	0.897	0.943	63.2	144.6	311.3	100.7	35	108.6	93.7	39.3	−1.2	3.18	0.051	18.67
571	26 Bootids	TSB	annual	343.76	331	357	214.3	26.2	0.55	−0.34	47.5	−0.10	26.1	0.495	0.981	133.1	270.7	343.8	76.2	63	104.0	84.7	59.4	−1.6	5.34	0.090	17.01
580	chi Andromedids	CHA	annual	154.95	152	160	27.3	45.7	1.36	0.41	59.9	0.15	15.5	0.781	0.950	60.9	237.6	154.9	119.0	29	108.3	91.6	60.9	−1.6	4.42	0.052	16.27
581	90 Herculids	NHE	annual	34.95	31	41	261.9	37.6	0.58	−0.07	40.5	0.02	21.5	0.883	0.959	99.5	221.3	35.0	65.1	33	103.9	89.0	59.2	−1.0	2.81	0.034	15.76
582	Jan. beta Craterids	JBC	annual	294.95	280	308	175.1	−27.9	0.96	−0.30	63.8	0.04	10.2	0.811	0.920	32.6	50.6	115.0	129.0	48	112.0	100.3	22.2	−0.9	2.79	0.061	18.37
593	28 Lyncids	TOL	annual	227.86	216	239	123.1	39.2	1.28	−0.30	65.9	0.03	60.6	0.694	0.989	471.2	246.5	227.9	142.5	34	111.8	89.8	57.3	−2.1	2.47	0.052	17.07
602	kappa Craterids	KCR	annual	289.88	282	301	171.3	−14.9	0.85	−0.32	66.3	0.04	16.1	0.665	0.959	64.8	70.2	109.9	145.7	41	111.1	93.7	34.0	−1.6	1.89	0.049	18.04
618	12 Hydrids	THD	annual	241.09	236	250	123.6	−9.4	0.92	−0.10	62.5	0.06	33.5	0.725	0.978	193.7	62.4	61.1	124.8	25	109.5	92.9	35.9	−1.3	2.54	0.041	17.74
648	22 Aquilids	TAL	annual	24.32	20	29	283.6	4.3	1.02	0.24	65.3	−0.04	18.9	0.957	0.949	82.3	204.8	24.3	133.2	16	111.1	96.0	34.6	−1.7	2.66	0.045	17.02
665	May upsilon Cygnids	MUC	annual	56.12	47	63	317.2	28.7	0.91	0.38	57.1	−0.11	10.5	1.000	0.905	34.1	168.3	56.1	107.8	18	107.7	93.6	44.8	−1.4	3.19	0.044	16.65
694	omicron Geminids	OMG	annual	166.17	152	178	118.3	37.9	1.10	−0.21	59.0	0.06	8.90	0.315	0.965	26.6	66.4	166.2	132.3	44	107.0	94.0	29.8	−0.7	3.58	0.076	18.29
707	beta Pixidids	BPX	annual	283.63	279	289	129.7	−35.6	0.68	−0.33	43.5	0.00	7.89	0.744	0.906	22.1	60.8	103.6	70.9	20	101.9	91.6	15.8	−0.5	3.54	0.042	16.47
715	alpha Camelopardalids	ACL	annual	185.20	175	191	75.5	66.3	1.85	0.08	56.3	0.12	12.2	0.942	0.923	42.4	208.7	185.2	104.6	23	108.5	92.9	47.2	−1.8	2.43	0.047	16.20
720	Nov. gamma Bootids	NGB	annual	244.99	241	247	214.0	39.8	−0.13	−0.34	48.7	0.31	18.2	0.779	0.957	78.0	124.7	245.0	82.4	8	107.7	93.3	33.9	−1.9	2.48	0.033	19.76
722	15 Leonids	FLE	annual	252.81	236	265	147.0	30.1	1.00	−0.38	66.0	0.06	35.1	0.612	0.983	208.2	256.4	252.8	146.9	54	110.6	92.2	61.9	−1.7	2.48	0.058	17.30
727	iota Serpentids	ISR	annual	275.77	269	284	230.8	21.4	0.89	−0.37	54.4	0.04	30.0	0.642	0.979	164.5	107.3	275.8	97.3	24	107.7	91.6	39.2	−2.0	4.30	0.056	19.96
751	kappa Cepheids	KCE	annual	172.88	168	179	11.7	86.1	—	—	43.8	−0.08	21.2	1.004	0.953	97.4	183.3	172.9	73.9	22	104.8	89.8	39.1	−1.5	2.96	0.036	15.51
814	Jan. Canum Venaticids	CVD	annual	303.12	299	308	184.5	40.6	0.93	−0.37	49.0	−0.03	20.7	0.524	0.975	93.9	267.0	303.1	81.3	24	106.0	86.0	65.1	−1.6	2.39	0.047	17.60
818	Oct. Aurigids	OAG	annual	204.73	199	208	68.2	35.6	1.25	0.22	57.4	0.16	−169	0.170	1.001		311.3	204.7	129.3	14	109.2	89.4	58.8	−2.0	1.69	0.076	15.39
827	nu Pegasids	NPE	annual	25.71	10	39	326.7	1.7	0.82	0.27	61.5	0.04	128	0.354	0.997	1446	72.6	25.7	142.9	31	110.9	96.2	20.5	−1.4	1.96	0.066	18.55
838	Oct. delta Sextantids	ODS	annual	211.61	209	214	160.3	−3.4	0.60	−0.26	59.5	−0.03	96.8	0.177	0.998	952.5	229.7	31.6	141.0	7	109.7	87.7	25.9	−1.7	1.36	0.036	19.62
854	psi Cygnids	PCY	annual	48.68	39	61	297.2	52.4	0.20	0.16	40.2	−0.03	17.1	1.005	0.941	70.9	173.5	48.7	66.8	37	104.3	87.9	45.4	−1.1	3.53	0.060	15.38
860	psi Andromedids	PAN	annual	72.11	71.7	72.7	355.5	46.7	0.89	0.55	50.4	−0.83	21.4	0.711	0.967	98.8	113.0	72.1	89.5	18	107.1	93.4	32.9	−1.2	0.97	0.025	16.51
862	16 Scorpiids	SSR	annual	5.35	355	15	245.9	−9.1	0.96	−0.12	64.1	−0.03	15.3	0.449	0.971	60.0	276.8	5.3	151.0	24	109.6	93.9	38.1	−1.3	2.89	0.056	17.78
877	omega Hydrids	OHD	annual	214.29	201	226	148.8	4.6	0.83	−0.29	66.7	0.05	17.2	0.550	0.968	71.2	275.3	34.3	163.9	29	112.3	96.0	33.7	−1.4	2.66	0.069	19.01
884	Nov. beta Pyxidids	NBP	annual	245.31	239	248	132.0	−35.2	0.53	−0.07	52.7	0.10	7.07	0.975	0.862	18.8	12.1	65.3	94.5	16	110.1	96.5	18.2	−1.3	3.55	0.055	18.90
889	Y Ophiuchids	YOP	annual	318.03	307	327	268.9	−7.0	1.02	0.16	58.2	−0.09	27.6	0.229	0.992	145.0	57.1	318.0	126.6	22	109.8	92.1	22.2	−1.7	4.26	0.081	19.86
893	eta Ophiuchids	EOP	annual	1.22	346	16	263.2	−16.3	0.81	−0.02	70.9	−0.04	27.6	0.946	0.966	145.3	205.4	1.2	168.1	46	113.7	99.7	27.9	−1.8	3.55	0.078	18.21
894	June mu-Draconids	JMD	annual	96.34	90	101	252.4	54.8	−0.24	0.25	23.8	−0.10	16.9	1.008	0.941	69.7	190.7	96.3	34.3	6	98.8	80.3	62.1	−2.7	2.86	0.021	14.46
900	beta Bootids	BBO	annual	285.03	278	290	223.9	42.2	0.68	−0.22	50.1	0.00	8.74	0.978	0.888	25.8	171.2	285.0	87.5	17	108.1	94.2	39.0	−0.7	2.13	0.039	18.18
1103	Jan. 15 Bootids	FBI	Too sparse to meteor shower members decide.																								
1119	Dec. lambda Velids	LAV	annual	257.86	252	263	135.3	−37.2	0.75	−0.35	52.4	−0.05	11.7	0.947	0.919	40.2	22.9	77.9	92.5	28	108.8	96.3	15.8	−1.1	4.71	0.041	18.44
1133	32 Cassiopeiids	TCS	annual	105.58	104.7	106.9	14.6	67.4	0.61	0.28	45.7	0.11	10.3	0.863	0.917	33.3	133.2	105.6	78.8	5	95.1	86.2	37.7	−0.5	2.24	0.024	15.45
1137	Aug. mu Perseids	AMP	Too sparse to meteor shower members decide.																								

The International Meteor Organization

www.imo.net

Follow us on Facebook InternationalMeteorOrganization

Follow us on Twitter @IMOMeteors

Council

President: Cis Verbeeck,
Bogaertsheide 5, 2560 Kessel, Belgium.
e-mail: cis.verbeeck@gmail.com

Vice-President: Juraj Tóth,
Fac. Math., Phys. & Inf., Comenius Univ.,
Mlynska dolina, 84248 Bratislava, Slovakia.
e-mail: toth@fmph.uniba.sk

Secretary-General: Robert Lunsford,
14884 Quail Valley Way, El Cajon,
CA 92021-2227, USA. tel. +1 619 755 7791
e-mail: lunro.imo.usa@cox.net

Treasurer: Marc Gyssens, Heerbaan 74,
B-2530 Boechout, Belgium.
e-mail: marc.gyssens@uhasselt.be
BIC: GEBABEBB
IBAN: BE30 0014 7327 5911
Bank transfer costs are always at your expense.

Other Council members:
Karl Antier, 16, rue de la République,
F-04100 Manosque, France.
e-mail: karl.antier@gmx.fr
Javor Kac (see details under WGN)
Detlef Koschny, Zeestraat 46,
NL-2211 XH Noordwijkerhout, Netherlands.
e-mail: detlef.koschny@tum.de
Sirko Molau, Abenstalstraße 13b, D-84072
Seysdorf, Germany. e-mail: sirko@molau.de
Francisco Ocaña Gonzalez, C/ Arquitectura, 7.
28005 Madrid, Spain.
e-mail: francisco.ocana.gonzalez@gmail.com
Vincent Perlerin, 16, rue Georges Bernanos,
51100 Reims, France.
e-mail: vperlerin@gmail.com
Jürgen Rendtel, Eschenweg 16, D-14476
Marquardt, Germany. e-mail: jrendtel@aip.de

Commission Directors

Visual Commission: Jürgen Rendtel
Generic e-mail address: visual@imo.net
Electronic visual report form:
http://www.imo.net/visual/report/electronic
Video Commission: Sirko Molau (video@imo.net)
Photographic Commission: Bill Ward
(bill_meteor@yahoo.com)
Generic e-mail address: photo@imo.net
Radio Commission: Chris Steyaert
(radio@imo.net)
Fireball Commission: Robert Lunsford
Online fireball reports:
http://fireballs.imo.net

Webmaster

Karl Antier, e-mail: webmaster@imo.net

WGN

Editor-in-chief: Javor Kac
Na Ajdov hrib 24, SI-2310 Slovenska Bistrica,
Slovenia. e-mail: wgn@imo.net;
include METEOR in the e-mail subject line

Editorial board: Ž. Andreić, D.J. Asher,
F. Bettonvil, M. Gyssens, C. Hergenrother,
T. Heywood, J. Rendtel, C. Verbeeck,
S. de Vet, D. Vida.

IMO Sales

Available from the Treasurer or the Electronic Shop on the IMO Website	€	$
IMO membership, including subscription to WGN Vol. 51 (2023)		
Surface mail	26	30
Air Mail (outside Europe only)	49	56
Electronic subscription only	21	24
Proceedings of the International Meteor Conference on paper		
1990, 1991, 1995, 1996, 1999, 2000, 2002, 2003, per year	9	12
2007, 2010, 2011, per year	15	20
2012, 2013, 2015, 2017 per year	25	32
Proceedings of the Meteor Orbit Determination Workshop 2006	15	20
Radio Meteor School Proceedings 2005	15	20
Handbook for Meteor Observers	23	29
Meteor Shower Workbook	12	16
Electronic media		
Meteor Beliefs Project ZIP archive	6	8

Bright fireball and aurora from Iceland

Very bright fireball appeared on 2023 September 12 at $22^{\rm h}35^{\rm m}$ UT that left a persistent train shown in the image below. These images were taken from Arctic Henge, Raufarhöfn, Iceland using Nikon D810a with Sigma 8-mm at $f/3.5$ and 2-second exposures at ISO 3200. Image creadit: Sævar Helgi Bragason.